

## CHAPTER 1

### INTRODUCTION

#### **1.0 Overview**

This chapter provides an introduction to the PhD thesis. It starts with the background of the work followed by problem statement. The motivation part highlights the need for this research. The objectives are defined to mark the goals of this thesis to fulfil the problem statement requirements. In the end, complete thesis outline is given to highlight main parts of this thesis work.

#### **1.1 Background**

There are numerous applications of gas sensors varying from households to business industry. Gas sensors are widely used to sense leakage in the delivery systems in houses and factories. On the other hand, they are used to sense corrosive gases in the pipelines in the oil and gas industry. There are many incidents in the history in which numbers of people were affected by the gas leakage. If the gas leakage is left unattended it is a big threat to human safety and can cause economic and financial loss. Gas leakage has lead to many unpleasant incidents ranging from supply shutdowns to the extreme case of human casualties. Sewer explosion in April 1992, in Mexico killed 215 and injured 1500 people. The cause of accident was gas pipeline leakage, leading to an explosion. Another natural gas pipeline exploded in New Mexico in August 2000; number of casualties was 12 and damage to three vehicles [1].

Initially, the need of gas sensor arises in the coal mines to detect the low oxygen level. Later on, there was a problem to detect the lowest explosion limit in the oil tankers. This forced human mind to think about the device which can solve these

problems. The work started in early 19<sup>th</sup> century and the England's Humphry Davey succeeded in making such a device. This leads to the advent of modern day gas sensors. Eventually, numbers of types of gas sensors with different useful specifications were developed. The competition started and companies tried to come up with highly efficient gas sensors. The criteria to evaluate the gas sensor efficiency is based on its number of parameters e.g. sensitivity, selectivity, reproducibility, stability, responsivity, and reversibility. The technology has emerged into the new era of gas sensors with the development of solid state gas sensors in 1968. Solid state gas sensors have number of advantages over the other sensors at that time. These sensors provide high sensitivity, reproducibility, responsivity, and were considered modern gas sensors of the time. Later on, different types of solid state gas sensors have been developed according to the specific requirements of different applications. The sensors which were considered very latest and modern few decades ago are not enough to meet the requirements of the current highly demanding applications. Although, solid state gas sensors are still in use but, today's application requirements need something which is one step ahead. The technology is changing very quickly especially, in the last two decades after the invention of the nanomaterials. Researchers are trying to take good advantage of these nanomaterials to scale down and to improve the efficiency of the devices. The nanomaterials, especially carbon nanotubes have number of useful properties which make them the heart of numerous applications. To make use of its field emission property, carbon nanotubes are also used in gas sensing technology. The details are provided in chapter 2.

The electric field breakdown property of the gas is known since 19<sup>th</sup> century. It is the natural property of every gas to become conducting or partially conducting when field becomes very high between the two boundaries. Lightning in the clouds and between cloud and the ground is a very common example of the electric field breakdown in the air. In a broad range it can be considered that the gas breakdown mechanism between two electrodes at some applied field is similar to the lightning process. The only difference is that lightning is in the long range separation between the two mediums e.g. meters or kilometres range without any externally applied potential. However, in the case of manmade device, there are two metallic electrodes and the very high potential is applied across them to give electric field breakdown of

the gas. But if technical details are considered, there is quite different phenomenon taking place in the manmade device. The details of the phenomenon are described in chapter 2.

The conventional type of gas breakdown devices suffer from the very high applied voltage e.g. in the kilovolt range and the huge size of the device. This keeps them away to use as the gas detecting devices in smart applications. In 1998, the introduction of the nanometaterials on the electrode was the real breakthrough in this field [2-3]. With the presence of nanomaterials on the electrode, the electric field breakdown was observed at a very low voltage. The size of the device was also reduced as it operates at low voltages. In 2001, carbon nanotubes were used first time as nanomaterials on the electrode and the device was used to detect several gases efficiently [4]. In 2003, the same device with carbon nanotubes on the electrode was developed with some different features and was named *miniaturized ionization gas sensor* [5]. After 2003, the race has started and up till now, several types of miniaturized ionization gas sensors have been developed. Later on, it is mostly called *ionization gas sensor*. Also in this thesis, the name used for this type of gas sensor is ionization gas sensor.

## **1.2 Problem Statement**

Since, ionization gas sensors are recently developed and research is still in progress, this provides a room to explore it in various aspects. These gas sensors work by fingerprinting the ionization characteristics of distinct gases. So far, most of the work is being done on the fabrication and characterization of these sensors. There are several parameters that can be optimized to improve the efficiency of ionization gas sensors. Some processes like, ionization which plays a key role in gas breakdown need to be examined in detail. The structure optimization of carbon nanotubes which is important in field enhancement needs to be examined in detail. The breakdown occurs very quickly, in few microseconds or earlier in some cases, so it is very difficult to examine the details experimentally due to equipment limitation. On the other hand, the optimization of the carbon nanotube structure requires very controlled fabrication environment and it is not possible to change the structure during

experiment. Every time new fabrication needs to be done to examine the new structure. To solve these problems, modelling and simulation of the ionization gas sensor is required. But unfortunately, there is no literature available so far on the comprehensive modelling of the ionization gas sensor. Also, the field emission model of carbon nanotubes for the application of ionization gas sensor does not exist. These problems provide the platform to this PhD thesis.

The motivation behind the development of field emission model of CNTs is to improve the efficiency of ionization gas sensor. It is believed that using proper models for the device useful information can be extracted which is often very difficult to obtain from experimental characterization.

### **1.3 Objectives**

The objectives of this work are as follows:

- To develop a field emission model of carbon nanotubes to study the gas detection mechanism in carbon nanotube based ionization gas sensor.
- To run simulations to test the functionality of the new model and to extract useful results.
- To validate the new model, so that it can be used to optimize the carbon nanotube based ionization gas sensor.

### **1.4 Scope of Study**

This research is based on a multidimensional project which requires a comprehensive knowledge of gas sensors especially, ionization gas sensors (from working mechanism to efficiency evaluation criteria), chemistry of the gases, physics of the plasma, nanomaterials and their properties (especially, carbon nanotubes and their field emission property), plasma simulation techniques and their mathematical modelling, and computer programming. It was a tedious task to deal with all these fields simultaneously. Hence, defining the scope of this research was itself a challenge.

The scope of this PhD thesis can be divided into following categories:

- (i) **Benchmarking:** The benchmarking part is to run the baseline simulations to understand the existing plasma simulation tool and to explore the contribution of important plasma parameters in the breakdown phenomenon. The results were compared with the published experimental and simulated data to validate the simulations.
- (ii) **Development of a new model:** In this part of the thesis, the emphasis was on the development of field emission model of carbon nanotubes. The model contains the effects of CNT density and aspect ratio parameters on the field emission behaviour. The new model was successfully embedded in the standard PIC-MCC codes.
- (iii) **Validation of a new model:** Number of simulation setups was run to test the functionality of the new model. The validation of the model was done by calculating the field enhancement factor  $\beta$  and comparing the value with the  $\beta$  of the well established published model.
- (iv) **Optimization of ionization gas sensor:** The useful results were obtained from the simulations carried out with the help of enhanced PIC-MCC codes. These results pave the way to optimize the ionization gas sensor.

## 1.5 Thesis Outline

In this section, brief outline of the following chapters is provided.

Chapter 2 contains the literature review which was done in the beginning of this project. The literature review was done to narrow down the problem statement, define the objectives, and to propose the methodology of this thesis. The literature review is divided into three major parts. The first part is the overview of some widely used gas sensors, the second part is on field emission property of carbon nanotubes, and third part is on the plasma simulation techniques. The remarks at the end of each section are provided to conclude the discussion of the respective section.

In chapter 3, the details of the methodology adopted for this thesis are provided. The overview of the working mechanism of particle simulation technique i.e. PIC-

MCC is given followed by the benchmarking phase. The criteria for developing the new model are discussed. The flow diagrams of the standard and new modules are given to provide adequate understanding of the working of the new model. The simulation parameters are also provided with every simulation setup.

Chapter 4 consists of results and discussion part of the thesis. The chapter starts with the results of benchmarking phase and their comparison with the published data. The results from the simulations to test the new model are validated and discussed. The findings are highlighted and the controlled parameters to optimize the ionization gas sensor are provided.

Chapter 5 contains the conclusion, recommended future work, and the contributions based on this thesis work.

## CHAPTER 2

### LITERATURE REVIEW

#### **2.0 Overview**

In this chapter the detailed literature review is given. The literature review is divided into three major parts. In first part, emphasis is given on different types of gas sensors, the sensing techniques and the performance parameters. In second part, the field emission property of the carbon nanotubes is discussed. Finally, third part provides literature on the plasma simulation techniques.

#### **2.1 Gas Sensors**

##### **2.1.1 Solid-State Gas Sensors**

Solid-state gas sensors are the outcome of the research work done on the p-n junction. It was discovered that the p-n junction was very sensitive to the environmental background gases. Initially, the sensitivity of the p-n junction to the environment is considered a setback of the device. Later on, the attempts were made to use this property of the p-n junction to sense the gas. Until 1968, the catalytic combustion sensor was the only type of the gas sensor available. The solid-state gas sensor shown in Fig. 2.1 provides several advantages over the catalytic combustion gas sensor including small size, high sensitivity at low concentrations, and low cost which made it very popular in a short time.



Fig. 2.1 Solid-state gas sensor [6]

The working principle of the catalytic combustion gas sensor is such that it burns the gas being detected and the sensor material is consumed every time. Eventually, the sensor burns out and needs replacement. However, in solid-state sensor the gas is absorbed on the sensor surface and detected by the change in the resistance of the sensor material. When the gas disappears, the sensor returns to its original condition. Hence, sensor material is not consumed in gas detection providing high reproducibility and long sensor life. There are different types of solid-state gas sensors and each type has different level of performance and quality. Depending on the characteristics, solid-state gas sensors can be used in a number of applications [7-12]. The widely used types of solid-state gas sensors are discussed below.

#### *2.1.1.1 Metal Oxide Semiconductor Gas Sensor*

The metal oxide gas sensors are composed of heated membranes that are fitted with gas sensitive semiconductor materials. The device cross section of the SOI based micro-heater arrays is shown in Fig. 2.2.

The heated membranes are used to raise the temperature typically around 400°C to 500°C and work as a thermal actuator. This high working temperature is one of the drawbacks of this type of sensors. When the temperature is raised at the surface of the

heated membrane, a chemical reaction takes place and the gas is absorbed by the semiconductor material. The initiation of the chemical reactions at the chemically sensitive material layer is responsible for the change in the conductivity of the material. The change in conductivity is measured and generates electrical output signals via the interfacing circuitry to detect the gas. The popular sensing materials are  $\text{SnO}_2$ ,  $\text{TiO}_2$ , and  $\text{WO}_3$  [13-15]. These materials are semiconductors with wide-band-gap. They respond to changes in their gaseous environment via reversible conductivity changes [11, 15-17].

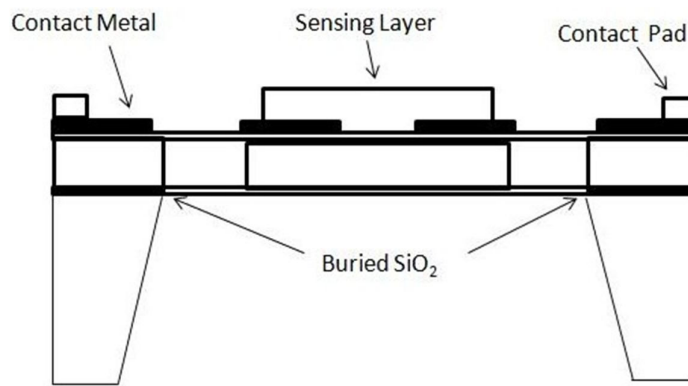


Fig. 2.2 Device cross-section of the SOI-based micro-heater arrays [6]

Most of the metal oxide semiconductor gas sensors are big in size as they are fabricated using bulk ceramic substrates [13-14]. Due to their bulky nature, ceramic heater substrates consume heating powers on the order of 0.5-1 Watt per sensor element for achieving the required operating temperatures of few hundred degrees centigrade. This large power consumption is a severe drawback of semiconductor gas sensor especially when utilized in a bus-connected sensor networks.

### 2.1.1.2 Field-Effect Gas Sensors

The field-effect gas sensors are first introduced by Lundstrom et. al. in 1975 [18-20]. The number of field-effect devices such as schottky diodes, capacitors and transistors can be used as a gas sensor. These devices are shown in Fig. 2.3.

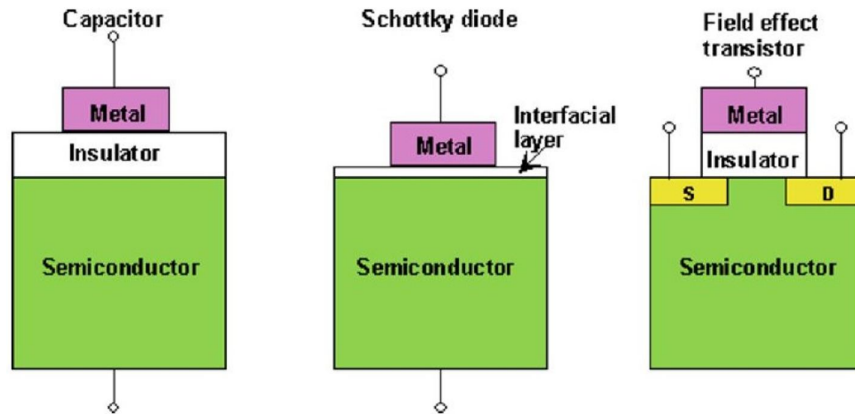


Fig. 2.3 Schematic diagram of FET device [6]

The schottky diode and transistor works at DC gate voltage but the drawback of the capacitor is the AC operation. Both schottky diode and transistors operate in the constant current mode. In these devices, the gas species react with the sensing layer and give corresponding change in the field effect. This field effect change leads to the change in the output signal and hence, the gas is detected. In the case of schottky diode, if the gate contact has large resistivity, it will lead to more prominent resistivity change instead of field effect when reacting with the gas species [21]. The capacitor which operates on the AC voltage gives response to the gas species with a change in the field effect only. The AC operation put limits on the conductivity of the gate metal and the insulating properties of the insulator on the top of the semiconductor.

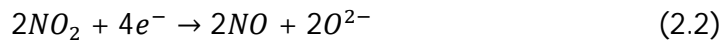
These devices usually operate at room temperature and initially used for hydrogen detection. Later on it is shown that a wide variety of hydrocarbon gases can be detected with the help of SiC devices. These devices need high operating temperature

around 400°C to 600°C [22-24]. This is a great drawback of these devices as the Si-MOS capacitors rapidly lose their efficiency and electronic performance is reduced at temperatures near 200°C. This disadvantage has limited the use of Si-MOS sensors in gas sensing applications.

### 2.1.1.3 Electrochemical Gas Sensor

The hazardous gases which cause pollution include CO, NO<sub>x</sub> (NO and NO<sub>2</sub>) and hydrocarbons (HCs). Usually, these gases are detected by electrochemical process. Many electrochemical gas sensors are developed based on solid electrolytes. Among them, the Ytria-Stabilized Zirconia (YSZ)-based gas sensor seems to be the most reliable and realistic for the application. The YSZ-based oxygen (air/fuel) sensor is in use on commercial grounds for more than 30 years. The current research is being done on the efforts to combine the YSZ with oxide-based sensing electrode (SE). Most of the research done on the solid-state electrochemical gas sensors so far is focused on the monitoring of combustion exhausts. The YSZ-based gas sensor operates in several modes. The overview of each mode is provided below.

Mixed-potential-type sensors based on YSZ works in tubular or in planar configuration with an oxide-SE. The sensor operation is based on the mixed potential that appears on the sensing electrode when anodic reactions rate becomes equal to the cathodic reactions. When in the combustion process the NO<sub>2</sub> exists with O<sub>2</sub>, the anodic reaction of O<sub>2</sub> and the cathodic reaction of NO<sub>2</sub> occur simultaneously at the SE-YSZ interface [25]. These anodic and cathodic reactions are given in Eq. 2.1 and Eq. 2.2 respectively.



In mixed-potential-type sensor the SE-YSZ interface is considered to be responsible for the mixed potential [26]. The selection of sensing electrode material and interfacing with YSZ is important in improving the efficiency of mixed-potential-type sensor. It is found that Nickel-Oxide (NiO) is the most promising sensing electrode

material which detects the  $\text{NO}_x$  upto  $850^\circ\text{C}$  [27-28]. Similarly, for the detection of hydrocarbons e.g propene ( $\text{C}_3\text{H}_6$ ) and methane ( $\text{CH}_4$ ),  $\text{In}_2\text{O}_3$  could be the best sensing electrode material. The sensor that uses  $\text{In}_2\text{O}_3$  as sensing electrode can selectively detect  $\text{C}_3\text{H}_6$  in very low concentration range of 10-200ppb at relatively low temperature of  $450^\circ\text{C}$ .

With advancements in the nanotechnology, the nanostructured NiO-based materials are also used as sensing electrode in the YSZ- based sensors. The nanostructured sensing electrode allows miniaturized sensor size, low power consumption along with improved sensitivity and faster response time. The sensing electrodes with gold (Au) nanoparticles of various thicknesses also give highly selective response to  $\text{NO}_2$  [29]. The nanostructured materials have remarkable chemical and electrochemical properties which provide a promising way to accomplish the desirable gas sensing characteristics.

Impedancemetric sensor detects the change in the complex-impedance of the device attached with the specific oxide-sensing electrode and transmits it as a sensing signal. It is a new type of sensor different from the conventional mixed-potential-type and amperometric sensor. It is used to detect  $\text{NO}_x$  [30-31], water vapour [32], and different combustible hydrocarbons [33]. The equivalent circuit of the impedancemetric YSZ-based sensor attached with oxide sensing electrode is shown in Fig. 2.4. In this equivalent circuit  $R_b$  is the bulk resistance of the YSZ,  $R_o$  and  $C_o$  are the resistance and capacitance of the oxide sensing electrode respectively. The resistance and capacitance due to the electrochemical reaction occurring at the interface between YSZ and oxide sensing electrode is represented by  $R_e$  and  $C_e$  respectively.

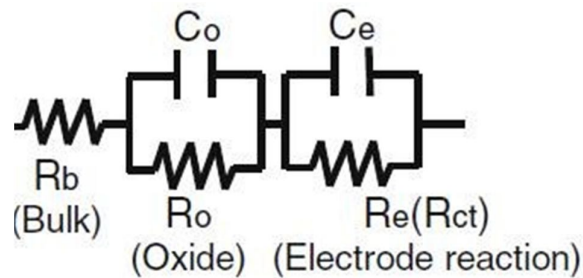


Fig. 2.4 The equivalent circuit for the YSZ-based sensor using oxide sensing electrode

An important feature of impedancemetric sensor is that they detect water vapour [30-31], and combustible hydrogen-containing gases [33]. The sensor operates at 900°C with  $\text{In}_2\text{O}_3$  as sensing electrode. These sensors are highly sensitive even with low concentrations of the gas and suited for the gas detection from combustion exhausts. Another highly sensitive impedancemetric YSZ-based sensor with ZnO as sensing electrode is reported by N. Miura et. al. [34]. The sensor is highly selective for the  $\text{C}_3\text{H}_6$  detection at very low concentration of 0.05 to 0.8 ppm.

These three types of electrochemical gas sensors described above have number of advantages and disadvantages depending on the operating temperatures and environmental conditions. These sensors have special features such as high temperature operation, excellent sensing performances and good chemical and mechanical stability. However, the main drawbacks for most of the solid-state electrochemical sensors are (i) a unique selectivity to the desirable gas in a multi-component gas systems and (ii) the long-term stability of the sensor in the harsh surrounding atmosphere.

#### *2.1.1.4 Optical Gas Sensors*

Another type of gas sensors is the optical gas sensors which use spectroscopy as the gas sensing technique [35-40]. They are used in wide application areas such as toxic gas alert, industrial and combustion processes control, environmental pollution monitoring, and human breath analysis for medical diagnosis. With advancements in the laser sources and optical components, some other methods were also established for optical gas sensing. Among these methods; ellipsometry and surface plasmon resonance (SPR) are very popular.

Spectroscopy is the widely used optical gas sensing technique [35, 37-40]. The basic principle behind the spectroscopic optical gas sensing is to monitor the optical absorption, emission, or scattering of the gas species at the particular optical wavelengths. The target gas species can be identified with the help of the wavelength distribution. The information about the target gas is provided by the intensity of the absorption, emission, or scattering phenomenon. The reliability of the spectroscopic

method is depends on the significant absorption or emission of optical radiation in a suitable wavelength band [6].

Many more spectroscopic gas detection schemes have been employed which are multipass absorption spectroscopy (MPAS), cavity-enhanced spectroscopy (CES), cavity ringdown spectroscopy (CRS), tunable diode laser absorption spectroscopy (TDLAS), tunable infrared laser differential absorption spectroscopy (TILDAS), photoacoustic spectroscopy (PAS). These optical spectroscopic gas detection schemes are developed to fulfil the challenging requirements for state-of-the-art gas sensors, including high gas sensitivity, high gas selectivity, real time and continuous measurements, field suitability, multicomponent compatibility, automatic or user friendly operation [6].

Ellipsometry is another optical gas sensing technique which is based on reflection mechanism and is used since many years [41]. The ellipsometric gas sensor working principle is based on monitoring the changes of the polarization state. The schematic illustration of ellipsometric-based sensing is shown in Fig. 2.5. As shown in Fig. 2.5, in ellipsometric gas sensor the sensing layer is a thin film over the substrate. This sensing layer is usually porous silicon due to its quite low detection limit threshold which is about 10 ppm in the case of acetone vapours [42]. The sensing layer is exposed to the target gas and the beam of light is incident on the thin film sample with an arbitrary angle  $\theta_i$  at the boundary of the medium. The part of the light will be reflected at  $\theta_r$  and the other part is transmitted through the sample at  $\theta_t$  angle. The reflected light intensity and the transmitted light intensity ratios over the total light intensity incident on the sample are measured. From these ratios the change in the polarization state are monitored and the ellipsometric parameters  $\Psi$  and  $\Delta$  for a thin film sample exposed are measured.

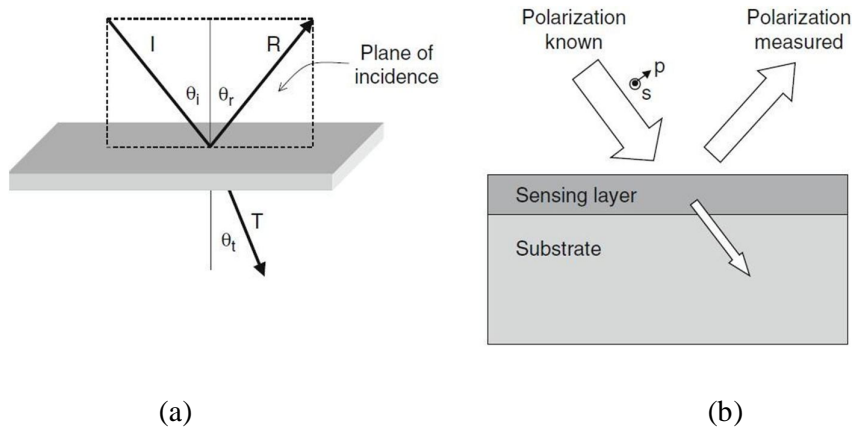


Fig. 2.5 (a) Schematic illustration of incident, refracted and reflected beams (b) Schematic illustration of ellipsometry-based sensing [6]

The advantages of ellipsometry are fast response time, high selectivity and sensitivity. To increase the efficiency of ellipsometry gas sensing method, several modifications have been adopted. The deposition of copper on the porous silicon sensing layer increase the sensitivity of the sensor to low concentrations of alcoholic gases such as methanol, ethanol, and 2-propanol [43]. The high sensitivity can also achieved by optimizing the porous silicon layer in terms of thickness and porosity [44].

Surface plasmons are the surface electromagnetic waves that propagate parallel along the metal-dielectric interface. Surface Plasmon Resonance (SPR) is a physical process that can take place when plane polarized light hits a metal film under total internal reflection conditions. SPR technique is a well standing technique for optical gas-sensing applications [45-49]. There are several configurations of SPR devices like, prism-coupled total reflection systems, grating coupled systems, and optical waveguide systems. The schematic illustration of SPR system employed for gas detection is shown in Fig. 2.6.

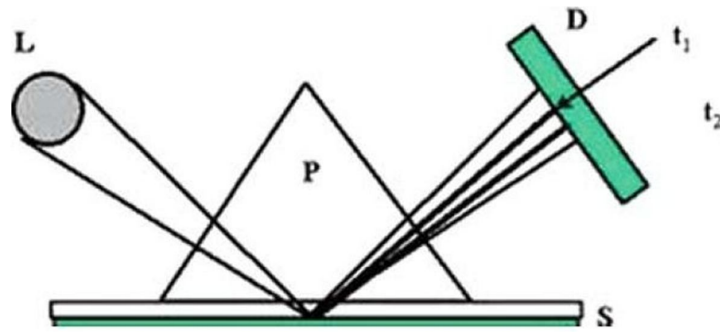


Fig. 2.6 Schematic illustration of surface plasmon resonance sensor [6]

The working principle of the SPR device depends on the light impinging at the interface between a metal and a dielectric material that can give rise to a resonant interaction between the waves and the mobile electrons at the surface of the metals. The metal film is evaporated onto the base of the glass prism. The incoming light from a light source is totally reflected at some critical angle. An evanescent wave penetrates through the metal film. The penetration is extended by a quarter of a wavelength beyond the reflecting surface. As a result, a decrease in the reflected light is observed. When the momentum of the surface plasmon becomes equal to the momentum of the incoming light, a resonance occurs. The SPR angles depend on the properties of the metal film. In order to improve the efficiency of the SPR, the thickness of the metal film must be optimized. The sensitivity of the SPR sensors can be improved by embedding gold nanoclusters in a dielectric film [50].

The main advantages of optical gas sensing over other techniques are high degree of gas specificity, non-contact or remote measurements, and potential of absolute measurements, intrinsically safe systems even in hazardous and explosive environments. On the other hand, they have disadvantages of high cost and low level of field robustness.

### 2.1.1.5 Surface Acoustic Wave (SAW) Gas Sensor

The term *acoustic* is usually used to cover the frequencies which are well above the audible range. Acoustic waves cover the frequency range from  $10^{-2}$  Hz to  $10^{12}$  Hz. The working of acoustic wave devices is based on the high-frequency mechanical vibrations. The acoustic waves which are confined to the surface of the piezoelectric material are known as surface acoustic waves. Piezoelectric-based SAW devices were first developed by White and Voltmer [51] in 1965. The most basic form of SAW device is shown in Fig. 2.7. The device consists of piezoelectric substrate, on top of which two metallic interdigital transducers (IDTs) are patterned to form a delay line structure. The gas-sensing layer is usually deposited between the two IDT ports. The delay path between the transmission and reception of the surface wave is determined by the separation between the IDT ports. The IDT geometry is used to determine the acoustic wavelength of the structure. Usually, equal finger width and spacing is used for IDT geometry for sensing applications.

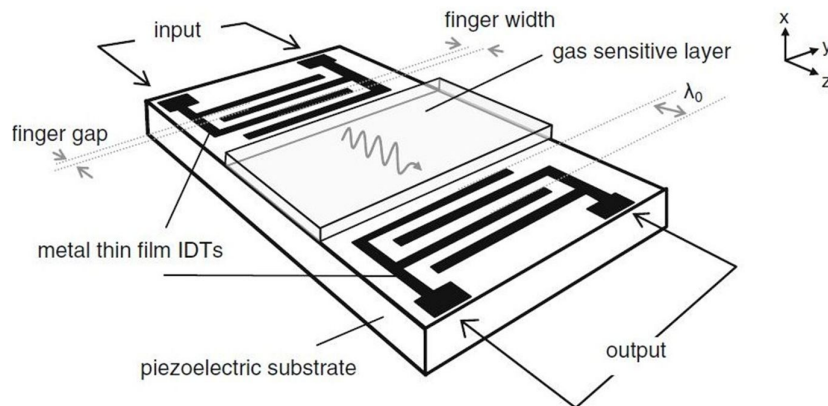


Fig. 2.7 (a) 2-port delay line SAW device with gas sensitive layer [6]

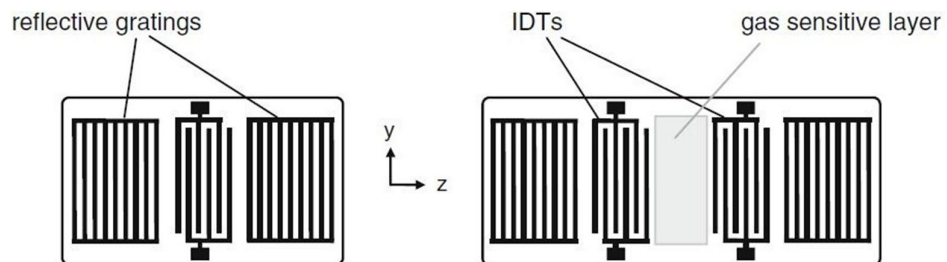


Fig. 2.7 (b) Top view of 1-port and 2-port SAW resonator [6]

The SAW devices operate by applying alternating voltage to the input IDT. The electrodes become positively or negatively charged and the electric field is created between them. The field distribution produces surface acoustic waves by inducing the strain in the piezoelectric substrate. The acoustic waves travel along the surface to the output IDT, where acoustic wave energy is converted into an electrical signal [52].

#### 2.1.1.5.1 Conventional SAW Gas Sensors

The conventional SAW gas sensor shown in Fig. 2.7 is the most commonly used SAW gas sensor. In this type of SAW gas sensor the sensitive layer is directly deposited over substrate between the IDT ports. The gas is detected by the change in the propagating acoustic mode's phase velocity. This change in the acoustic mode's phase velocity is related to the change in the resonant frequency. The device response can be obtained by several attenuation and phase measurement techniques [53-55]. The measured quantities are then correlated with the gas concentration.

#### 2.1.1.5.2 Multi-Layered SAW Gas Sensors

Multi-layered SAW gas sensors contain the thin-film layer which is deposited between the SAW substrate and the gas sensitive layer as shown in Fig. 2.8. These sensors are mostly used for liquid-phase-sensing applications. It is reported that these sensors have been used for the detection of hydrogen [56-60], nitrogen dioxide [61-63], and ethanol vapour [64].

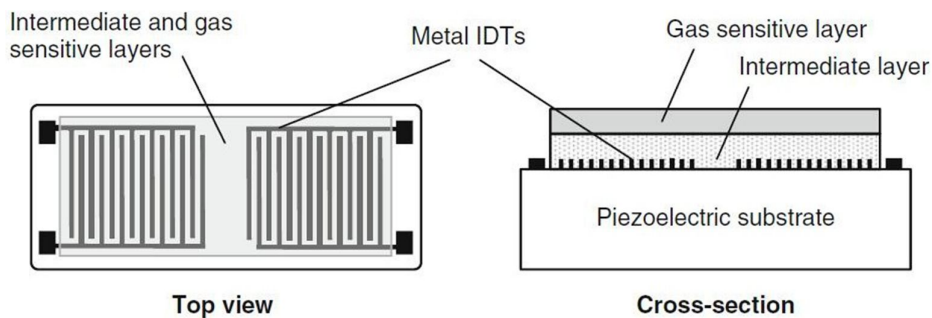


Fig. 2.8 Layout of multilayered two-port delay line SAW device [6]

Multi-layered SAW sensors have several advantages over the conventional SAW devices like, increased electromechanical coupling coefficient, increased sensitivity,

ability to generate several modes of propagation, improved temperature compensation, isolation of the substrate from the gas-sensing environment, and the generation of acoustic waves on a non-piezoelectric substrate as well [65].

Overall, SAW devices are well established in the electronics industry since last 30 years [66]. They have high sensitivity in the range of parts-per-million (ppm) and parts-per-billion (ppb) concentrations. Recent research on SAW devices includes the investigation on the sensing properties with different combinations of materials [67]. The modelling of the device is very important to analyze and investigate issues related to the performance. The advances in SAW sensor modelling have greatly facilitated the design and analysis of high performance multi-layered structures [68-70]. A significant advantage of SAW-based sensor is their rigid planar structure. They have small dimensions and can easily be integrated in sensor arrays. These devices can easily be interfaced with external circuitry for direct frequency output signal monitoring. On the other hand, it is very difficult to satisfy all the requirements with one sensor design. Therefore, the selection of structural parameters and materials result in design tradeoffs between device sensitivity, stability, selectivity, and operating temperature.

#### *2.1.1.6 Cantilever-Based Gas Sensor*

In 1968, Wilfinger et al. [71] detected adsorption by measurement of bending or change in resonance frequency in large silicon cantilever structures of dimension 50mm x 30mm x 8mm. After that many researchers start working on the microcantilevers. Heng [72] fabricated gold microcantilevers which are capacitively coupled to microstrip lines. They are used for the mechanical trimming of high-frequency oscillator circuits. Peterson [73] constructed silicon based cantilever-type micro-mechanical membrane switches. Kolesar [74] suggested electronic detectors for nerve agents. These electronic detectors can be fabricated with the help of cantilever structures. The breakthrough for microcantilever came and the micro-fabricated cantilevers become available commercially with the advent of atomic force microscopy (AFM) in 1986 [75].

The microcantilever surfaces are fabricated such as to detect the adsorption of molecules. The upper surface of the microcantilever is coated with a thin layer showing affinity to the molecules in the environment to be detected. This layer is called the functionalized surface of the microcantilever as shown in Fig. 2.9. The lower surface is coated with a passivation layer being inert to the molecules to be detected. Usually, microcantilever sensor has two modes of operation namely, (i) static mode and (ii) dynamic mode. In static mode, the gas molecules adsorb on the functionalized surface and form a layer. The microcantilever gradually bends with the weight of the molecules. The surface stress changes in the cantilever help to detect the molecules. In dynamic mode of operation, the mass change on the microcantilever surface is determined. The microcantilever oscillating frequency is tracked during mass adsorption and desorption. As the mass is added on the cantilever's surface, the frequency will shift to a lower value and the microcantilever will act as a microbalance.

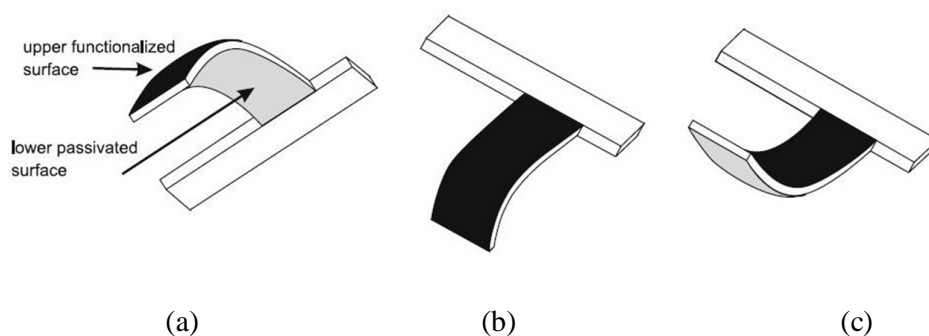


Fig. 2.9 Schematic drawing of microcantilever (a) lower surface passivated and upper surface functionalized (b) downward bending (c) upward bending [6]

Recent research on microcantilever gas sensors covers several theoretical, simulations and fabrication aspects. Hu et al. [76] reported the bulk adsorption of hydrogen on palladium using differential stress formation on a bimaterial cantilever. Baselt et al. [77] describe the design of a micro-electromechanical (MEMS) hydrogen sensor consisting of an array of 10 micromachined cantilever beams. The sensor was highly sensitive so that it can easily detect concentrations of 0.4% hydrogen. Fabre et al. [78] present a hydrogen sensor based on Pd-coated microcantilevers. They found

that the influences of the microcantilever shape and surface roughness play an important role. The investigation of hydrogen storage capacity of carbon nanotubes (CNTs) was reported by Ono et al. [79]. Zhou et al. [80] detected 10 ppm concentration of Freon, and Adam et al. [81] detected 50 ppb of mercury using piezoelectric microcantilevers. HCN was detected down to concentration of 150 ppm using embedded piezoresistive microcantilever sensors by Porter et al. [82].

Beside gas sensing, the microcantilever sensors can also be used to detect chemical vapour [83], explosives, and gas pressure and flow sensing [84-88].

### **2.1.2 Ionization Gas Sensor**

Ionization gas sensors are based on electrical conductivity of the gases in a high electric field region. These gas sensors are used in high precision gas analyzers such as chromatograph and mass spectrograph to sense the concentration and type of gases. However, the traditional ionization gas sensors have number of limitations, e.g. high working voltage, high vacuum environment, and their huge and bulky architecture. The first miniaturized MEMS based ionization gas sensor was reported in 1998 by two different groups, Dai et al. [2], and Ghodsian et al. [3]. In MEMS based ionization gas sensor of Dai et al., the operating voltage was reduced from thousands of volts to few hundred volts. Ghodsian et al. reported a successful detection of 14ppm  $\text{CH}_3\text{COOH}$  at an operating voltage of 5V.

CNT based ionization gas sensor, another optimized form, was developed by Y. Zhang et al. [4] in 2001. They reported the successful detection of several gases at lower operating voltages. In 2003, Modi et al. [5] developed the second CNT based ionization gas sensor with some different features from the previous one. After that, CNT-based ionization gas sensors have drawn much attention and research is underway on different aspects of these sensors [89-92]. Now, researchers working in gas sensing field are in a row to fabricate optimized ionization gas sensors. Apart from CNT, people have started embedding different nanomaterials like, gold nanowires (AuNWs) [93-95], zinc oxide (ZnO) nanowires [96], and silver nanowires (AgNWs) [97] in ionization gas sensors.

In the later sections, the basic principle and working of ionization gas sensor is described in detail.

### 2.1.2.1 Working Principle of Ionization Gas Sensor

Ionization gas sensors detect gas by using the electrical breakdown property of the gas. The simplified schematic diagram of the ionization gas sensor is shown in Fig. 2.10. It consists of two parallel metal electrodes separated by some distance called gap spacing. Nanomaterials are fabricated on one of the electrodes to enhance the electric field at lower voltages. When voltage is applied between the electrodes, electric field becomes non-uniform and high electric field region is created near the sharp tips of the nanomaterials. This high electric field region helps to ionize the gas molecules and to emit the secondary electrons from the electrode. Ultimately, the gas becomes conducting and the electric field breakdown occurs between the electrodes. The threshold field which is required to achieve the electrical breakdown is different for every gas. This unique property of a gas is used to detect the gas in an ionization gas sensor.

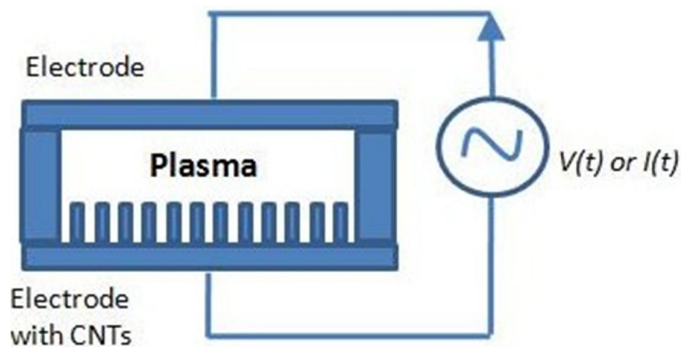


Fig. 2.10 Simplified schematic diagram of CNT based ionization gas sensor

### 2.1.2.2 Gas Breakdown Mechanism

The gas breakdown phenomenon is under investigation since more than one century. Very wide range of literature is available on different types of gas breakdowns in different gases by number of researchers in the world [98-110]. The literature available before the existence of nanomaterials is on the gas breakdowns between bare parallel and cylindrical electrodes. However, in ionization gas sensor nanomaterials are used on the electrode to lower the breakdown voltage. First, the concept of electrical breakdown in gas is provided and then, the role of nanomaterials in the gas breakdown mechanism is discussed.

In general, the electrical breakdown of gas is a process of transformation of non-conducting gas into a conductor which generates different kind of plasmas in the presence of sufficiently strong field. The gas and the electrode are two major components involved in the breakdown mechanism. Hence, the electrical breakdown depends on the number of parameters related to the gas and the electrodes. Among these parameters, gas pressure and electrode spacing plays an important role. The breakdown criteria can be of different type depending on the gas pressure according to Osmokrovic [109]. When the gas pressure is very low (high vacuum) and gap spacing is also very small, the breakdown is initiated, developed, and self-sustained by the processes taking place due to the electrodes. Gas plays no prominent role in the breakdown. At slightly high pressure and gap spacing, the breakdown is initiated by the gas processes but developed and self-sustained by the electrodes. At more high pressure and gap spacing values, the breakdown is initiated and developed by the gas processes but self-sustained by the processes due to electrodes, which is called *Townsend mechanism of breakdown* [99]. At very high gas pressure and large gap spacing between the electrodes, breakdown is initiated, developed, and self-sustained by the gas itself. This condition is called *Streamer's formation or Meek breakdown condition* [111]. It is not possible to define the boundaries between these types of breakdowns in certain pressure ranges. In some cases, the breakdown occurs due to one of these mechanisms only but in certain cases the breakdown occurs due to the combination of these mechanisms [109].

In miniaturized ionization gas sensors, the gas pressure can vary from few Torr to few atmospheres but the gap spacing between the electrodes is very low specifically, in micrometer range due to small size of the device. Hence, the breakdowns mostly observed in the ionization gas sensor are based on Townsend breakdown mechanism.

#### 2.1.2.2.1 Townsend Mechanism of Gas Breakdown

When potential is applied between the electrodes and electric field is created, electrons gain energy from the electric field and distribute this energy for all other processes. The applied electric field is uniform and is determined by Eq. (2.3)

$$E = \frac{V}{d} \quad (2.3)$$

where 'V' is the voltage applied and 'd' is gap spacing between the electrodes. When the electrons collide with gas atoms ionization process is indicated depending on the electron energy and the gas pressure. The gas pressure is directly proportional to the collision probability. The electrons created as a result of ionization are called primary electrons. The primary electrons provide very low initial current  $i_0$ . These electrons attract towards the anode and collide with other gas atoms and ionize them. As a result, an electron avalanche is generated. This avalanche started with a small number of *seed* electrons. Sometimes, it can even be triggered with a single electron. The avalanche evolves in time and in space because multiplication of electrons proceeds along with their drift from the cathode to anode. The simplified process is shown in Fig. 2.11.

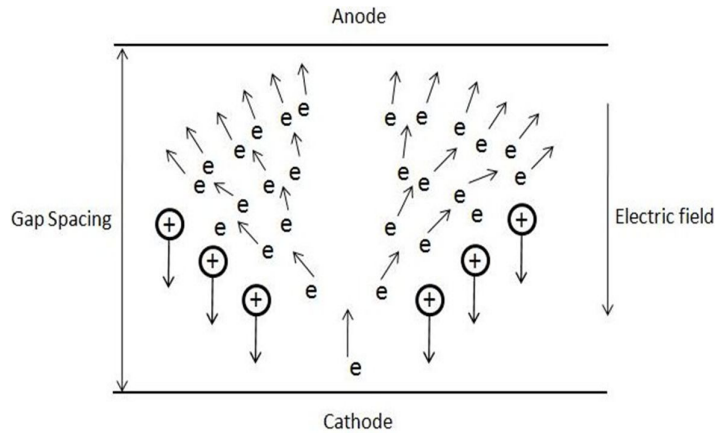


Fig. 2.11 Townsend breakdown gap

The number of ionization collisions in an avalanche can be described by the *Townsend's ionization coefficient*  $\alpha$ .  $\alpha$  is defined as the number of ionization events performed by an electron per centimetre (cm) along the field. The Townsend ionization coefficient is related to the ionization rate coefficient as in Eq. (2.4),

$$v_i = \alpha v_d \quad (2.4)$$

where  $v_i$  is the ionization frequency with respect to one electron and  $v_d$  is the electron drift velocity. The complete description of the ionization rate is provided by the frequency  $v_i$ , especially in the fast-oscillating fields. However, dc measurements give  $\alpha$ .

Along with electrons, ions are also created as a result of ionization process. According to Townsend's ionization coefficient, each primary electron generated near the cathode and moving towards the anode produces  $e^{\alpha d} - 1$  ions in the gap spacing between the electrodes. The ions created are positively charged and attracts towards the cathode. All of these ions created by that one electron hit the cathode and as a result each of these ions produces  $\gamma$  electrons from the cathode.  $\gamma$  is another Townsend coefficient called *secondary electron emission coefficient*.  $\gamma$  is defined as the description of the probability of the secondary electron emission on the cathode by an ion impact. So, total number of secondary electrons coming out of the cathode due

to  $e^{\alpha d} - 1$  ions is  $\gamma[e^{\alpha d} - 1]$ . These secondary electrons have to travel all the way from cathode to anode. Thus, these electrons produce more ionization than an electron born halfway.

Hence, the overall process can be best thought of as the multiplication of avalanches. Now, at this stage it is easy to define an avalanche. One avalanche can be considered as the process from the moment an individual electron leaves the cathode until the moment when all  $e^{\alpha d}$  electrons (which are its descendents) reach the anode. From this definition we can make a clear picture of electron multiplication. The breakdown started with few electrons or with a single electron in one cycle, then in the second cycle they multiplied to make e.g.  $x$  avalanches and in the third cycle there are  $x^2$  avalanches and so on. With this secondary electron emission, the steady discharge current formula derived by Townsend in 1902, also known as *Townsend formula* is given by Eq. 2.5.

$$i = \frac{i_0 e^{\alpha d}}{1 - \gamma[e^{\alpha d} - 1]} \quad (2.5)$$

The current in the gap spacing is non-self-sustained if the denominator in Eq. (2.5) is positive. As soon as, the electric field and the Townsend ionization coefficient  $\alpha$  become sufficiently large, the denominator in Eq. (2.5) goes to zero. At this point, a transition from non-self-sustained current to self-sustained current takes place which is the onset of breakdown. Thus, the breakdown condition in the gap is given by Eq. (2.6).

$$\gamma[e^{\alpha d} - 1] = 1 \quad (2.6)$$

This mechanism of ignition of a self-sustained current in a gap controlled by secondary electron emission from the cathode is called *Townsend breakdown mechanism*.

### 2.1.2.2.2 Paschen's Law and Minimum Breakdown Conditions

Paschen's Law developed by Friedrich Paschen in 1889 [98] states that the breakdown voltage of a gas between two bare parallel electrodes is a function of a product of gas pressure and the gap spacing. Paschen's Law is given by Eq. (2.7).

$$V_b = f(p \cdot d) \quad (2.7)$$

Later on, in 1910, Townsend suggested empirical formula to calculate the ionization coefficient  $\alpha$ , given by Eq. (2.8).

$$\alpha = A \cdot p \cdot e^{-\frac{Bp}{E}} \quad (2.8)$$

In Eq. (2.8),  $p$  is pressure of the gas,  $E$  is the electric field, and  $A$  and  $B$  are constants. The Eq. (2.8) is combined with Townsend's breakdown condition, given by Eq. (2.6), to derive the relations of breakdown voltage and electric field given by Eq. (2.9).

$$V_b = \frac{B(p \cdot d)}{C + \ln(p \cdot d)}, \quad \frac{E}{p} = \frac{B}{C + \ln(p \cdot d)} \quad (2.9)$$

In Eq. (2.9),  $B$  is the same constant as in Eq. (2.8), but  $A$  is replaced by  $C$ . Where  $C$  is given by Eq. (2.10).

$$C = \ln A - \ln \ln \left( 1 + \frac{1}{\gamma} \right) \quad (2.10)$$

The values of constants  $A$ ,  $B$ , and  $C$  can be found in [112]. Here, the influence of secondary electron emission is double logarithmic and is very weak. From Eq. (2.9), the dependence of breakdown voltage on the product  $p \cdot d$  can be clearly described which is the statement of Paschen's Law. Eq. (2.9) can also be used to calculate the minimum breakdown voltage of the discharge gap. The minimum breakdown voltage can be given by Eq. (2.11).

$$V_{b_{min.}} = \frac{e \cdot B}{A} \ln \left( 1 + \frac{1}{\gamma} \right) \quad (2.11)$$

For minimum breakdown voltage, the electric field is given by Eq. (2.12)

$$\left(\frac{E}{p}\right)_{V_{b_{min.}}} = B \quad (2.12)$$

and the value of  $(p \cdot d)$  is given by Eq. (2.13)

$$(p \cdot d)_{V_{b_{min.}}} = \frac{e}{A} \ln\left(1 + \frac{1}{\gamma}\right) \quad (2.13)$$

However, the minimum limit of the  $(p \cdot d)$  for which the breakdown can occur in the gas is given by Eq. (2.14)

$$(p \cdot d)_{limit} = \frac{(p \cdot d)_{V_{b_{min.}}}}{e} \quad (2.14)$$

where in Eq. (2.11), (2.13), and (2.14),  $e = 2.72$ , which is the base of natural logarithms. From above equations it is concluded that minimum value of electric field does not depend on the secondary electron emission and thus on cathode material in contrast to the minimum breakdown voltage.

### 2.1.2.3 Role of Nanomaterials in Gas Breakdown

Nanomaterials, e.g. CNTs on one of the electrodes in ionization gas sensor have remarkable effect on the gas breakdown mechanism. The CNTs have long thin structure with high aspect ratio and sharp pointed tips as shown in Fig. 2.12. The electric field becomes non-uniform due to the presence of CNTs. The region near the tips of the CNTs is at high electric field gradient than anywhere else between the electrodes. The gas atoms in this high electric field region experience large force of attraction towards the tips. As the field becomes sharply non-uniform by increasing the voltage, the electron is separated from the atom leaving the atom to be positively ionized. This phenomenon is similar to the *corona discharge*, in which one electrode has plane shape but the other one has sharp pointed tip. The corona discharge arises when the field become strongly non-uniform and the characteristic size of the pointed electrode is much smaller than the gap spacing between the electrodes. This happens because the minimum energy required to produce one electron-ion pair (minimum

price of ionization) is achieved at much lower voltage compared to the parallel plate electrodes without CNTs. The reason is establishment of high non-uniform electric field due to the presence of nanomaterials.

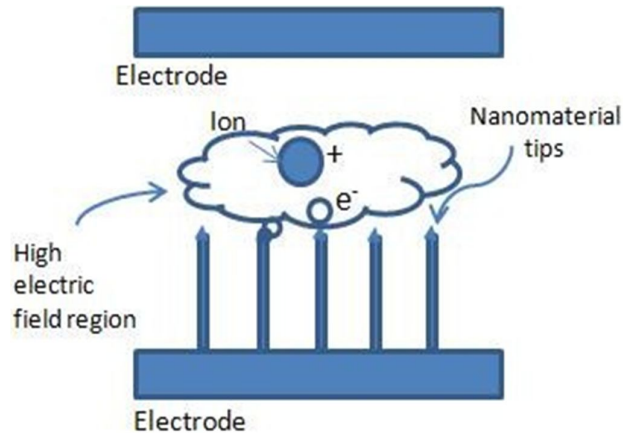


Fig. 2.12 High electric field region near sharp tips of CNTs help gas atoms to ionize

On the other hand nanomaterials, especially CNTs have very good field emission property. They are capable to produce very high currents, and hence contribute to the secondary electron emission, at very low applied fields. The detailed overview of the field emission property of the CNTs is provided in the section 2.2.

Hence, the role of CNTs in the gas breakdown mechanism in ionization gas sensor is very important. They contribute to both, local effects (ionization and the processes produced by the gas) and non-local effects (secondary electron emission and the processes in which electrode is involved).

Now, to conclude talk on the gas sensors, I would like to say that a very brief overview of few types of gas sensors is provided in section 2.1. Still, there is lot of literature available which is left unattended due to the limited scope of this research project.

Everything in this world has its advantages and disadvantages and same is the case with gas sensors. Different type of solid state gas sensors discussed above have a big advantage that the material of the gas sensor is not consumed in gas detection like in catalytic combustion sensor. Some gas sensors like, optical, and cantilever based sensors have high sensitivity. Electrochemical gas sensors have high temperature operation, good stability but have problem of selectivity of a gas when used in mixture of gases. Field effect gas sensors detect hydrogen at room temperature but needs high temperature around 400°C to 600°C for the detection of other hydrocarbons which affects their performance. Most of the other solid state gas sensors commercially available have the disadvantage of high temperature operation and high power consumption. Some gas sensors have conductivity-based detection mechanism in which the gas is absorbed on the sensing layer. This absorption process needs some time, although few seconds, but still the detection mechanism is delayed. So, the sensors have response time issues. During gas detection they detect the change in the conductivity of the sensing layer. Sometimes, when used in a mixture of gases, alarm rings at the wrong gas. Hence, selectivity of the gas is another issue. After gas detection, the gas needs to de-absorb from the sensing layer. It also requires some time (few seconds) and after the gas is completely de-absorbed the sensor is again available for another operation. So, again the response time problem. After several operations, some types of sensing layers do not respond to the gas as they responded first or second time so, reproducibility problems arise. But these disadvantages don't mean that these gas sensors are not in use anymore. In some applications response time is not an issue but high sensitivity is required and in some applications sensitivity is the secondary priority but high stability is required. So, depending on the particular application requirements, most of the sensors are still in use and commercially available.

Solid state gas sensors are quite old and detailed research on every aspect including the design and modelling part of these sensors is being done in the last few decades. So, now there is less research opportunities in these sensors compared to the newly developed gas sensors like, miniaturized ionization gas sensors.

The miniaturized ionization gas sensor fabricated in 1998 [2-3] and CNT based ionization gas sensor in 2001 [4], being quite new compared to the other gas sensors. These gas sensors have advantages of room temperature operation, less power consumption, and small size. These sensors are based on the electrical breakdown property of the gas to detect it, for which the threshold is different for every gas; hence high selectivity is achieved in a mixture of gases. As, no adsorption and desorption of the gas is required on the sensor so, fast response time can be achieved. Nanomaterials are used on the electrode to lower down the breakdown voltage; hence these sensors are highly sensitive at lower voltages.

As, these gas sensors are being developed recently and research is relatively new mostly conducted in the last one decade, this leaves number of areas under investigation or still unexplored. These areas include the optimization of electrode structure, fabrication aspects of nanomaterials, ionization processes, gas breakdown mechanism, and most importantly the modelling of ionization gas sensors. Almost all the work reported so far on the ionization gas sensors is based on the design, fabrication, and characterization of the device [3-5, 89-91, 93-96]. Negligible attention has been paid towards the modelling and simulation part of the ionization gas sensor. Only one paper which is reported in the end of year 2009, after we started this project in 2008, has basic overview on the modelling of silver nanowire based ionization gas sensor [97]. Still, no work has been found in literature on the modelling of CNT based ionization gas sensor, which is a main focus of this research thesis.

## **2.2 Field Emission from Carbon Nanotubes (CNTs)**

In general, field emission is the extraction of electrons from a solid by tunnelling through the surface potential barrier in the presence of applied field. The details can be found in the literature [113-116].

CNTs were first discovered by Iijima in 1991 [117]. Beside its number of useful properties, CNTs are proven to be excellent electron field emitters. Their potential as electron field emitters were first reported in 1995 [118-120]. But, CNT has gained much attention as field emitters in 1998 when Q. H. Wang and co-workers [121]

reported the world's first CNT based field emission flat panel display. The same year, Y. Saito and co-workers [122] reported CNT based lighting element. These works provide a new direction to the researchers and scientists interested in the properties of CNTs and working on applications of electron field emission. A very wide range of literature is available on the field emission property of different types of CNTs. Many studies used different techniques to optimize CNT fabrication to enhance the field emission. Typically, the field emission is measured in terms of turn-on field and threshold field. Turn-on field is the amount of field required to extract a current density of  $10 \mu\text{A}/\text{cm}^2$  and threshold field is the field at which current density of  $10 \text{mA}/\text{cm}^2$  is achieved. Normally, electron emission is observed with CNTs at fields below  $1 \text{V}/\mu\text{m}$ . According to Bonard et al. [123] the turn-on field is usually below  $5 \text{V}/\mu\text{m}$  and threshold field is around  $7 \text{V}/\mu\text{m}$ . CNT films are capable to emit current densities up to few  $\text{A}/\text{cm}^2$  at field below  $10 \text{V}/\mu\text{m}$ . In another report, Boanrd and co-workers [124] reported that CNTs have excellent field emission with operating voltages far lower than diamond. In some other studies, the turn-on field as low as  $0.75 \text{V}/\mu\text{m}$  and threshold field  $1.6 \text{V}/\mu\text{m}$  is achieved [125]. The difference in the field emission behaviour of CNTs mainly depends on the electrostatic screening effects. These electrostatic screening effects are produced depending on various factors e.g. fabrication process, structure of CNT, density of CNT on the substrate, aspect ratio of CNT etc. Among these, the effects of some parameters on the electrostatic screening are described below.

### **2.2.1 Effect of Electrostatic Screening on the CNT Field Emission**

The electrostatic screening effects are defined as the effects due to very close presence of the neighbouring CNT which screens the applied electric field and decreases the effective field amplification. These effects arise when the intertube spacing is very small or negligible as compared to the height of the CNT. In this case, the actual number of emitting sites (CNTs which are contributing to the field emission) becomes low. All the CNTs do not contribute to the field emission due to the CNT tips very close to each other. According to Manohara et al. [126] the electrostatic screening effect can also be produced due to height difference of the

densely packed CNTs. During fabrication, it is very difficult to control the same height of the CNTs. Some CNTs have longer heights than others. The CNTs with shorter height do not contribute to the field emission to an extent the longer CNTs. The CNTs with much shorter heights do not emit as much as due to the lack of field penetration. Hence, the overall field emission is decreased. There are several factors which can produce electrostatic screening effects and reduces the field emission. Among these factors, some of them are given below.

#### *2.2.1.1 Effect of CNT Fabrication Methods on Field Emission*

In literature, CNTs fabricated with different methods are used to test the field emission behaviour. It is difficult to compare all of them because the methods used for synthesis, purification, and deposition, are varied. If these parameters are same then the experimental setup e.g. gap spacing between the electrodes can be different. The first method used for the production of CNTs is the *arc discharge* method. This method can be used to produce both multiwall nanotubes (MWNTs) [117, 127] and singlewall nanotubes (SWNTs) [128-129]. Bonard et al. [130] prepared MWNTs by arc discharge method and tested their field emission behaviour. They provide very good field emission giving turn-on field  $2.6 \text{ V}/\mu\text{m}$  and threshold field  $4.6 \text{ V}/\mu\text{m}$ . Similarly, the turn-on fields of  $1.1 \text{ V}/\mu\text{m}$  and threshold field of  $2.2 \text{ V}/\mu\text{m}$  is observed for the sample of MWNTs fabricated with arc discharge method [131]. The nanotubes fabricated with *chemical vapour deposition* (CVD) method are also used by many groups to test the field emission property. The MWNTs of Xu and Brandes [132] fabricated by CVD method showed turn-on field of  $4.8 \text{ V}/\mu\text{m}$ , and threshold field of  $6.5 \text{ V}/\mu\text{m}$ . The MWNTs of Rao et al. [125] fabricated with CVD method showed lower turn-on and threshold fields which are  $0.75 \text{ V}/\mu\text{m}$  and  $1.6 \text{ V}/\mu\text{m}$  respectively. This difference in field emission behaviour of nanotubes fabricated with same method is due to the influence of other factors which are different in both cases. But, very high electron field emission is reported for CNTs fabricated by both arc discharge and CVD method. In one of the recent reports by Srivastava et al. [133], CNTs were prepared with microwave plasma enhanced CVD process and the turn-on and threshold fields of as low as  $1 \text{ V}/\mu\text{m}$  and  $2.1 \text{ V}/\mu\text{m}$  is observed. Silan et al. [134]

reported in 2009 that they have introduced a novel geometry of CNTs capable of achieving high current densities. They have fabricated a patterned vertically aligned CNT bundles with an open centre capable of achieving current densities up to  $60 \text{ mA/cm}^2$  at DC field of less than  $8 \text{ V}/\mu\text{m}$ . The same year Seung et al. [135] fabricated organic binder-free CNTs by filtration-transfer technique to improve the field emission. They reported the turn-on and threshold fields of  $0.77 \text{ V}/\mu\text{m}$  and  $1.88 \text{ V}/\mu\text{m}$  respectively, which is an excellent field emission.

#### *2.2.1.2 Effect of CNT Structure on Field Emission*

CNTs can be fabricated with different structures e.g. SWNTs, MWNTs, open tips, closed tips, vertically aligned, etc. The properties of these structures are somehow different from each other. Some properties vary to a large extent and some have slight effects. Field emission is also influenced by the structure of the nanotube. P.J. de Pablo and co-workers [131] studied the behaviour of different structures of CNTs on electron field emission. Keeping all other parameters same, they reported the turn-on field and threshold field of  $2.6 \text{ V}/\mu\text{m}$  and  $4.6 \text{ V}/\mu\text{m}$  respectively, for the MWNTs and  $2.8 \text{ V}/\mu\text{m}$  and  $5.2 \text{ V}/\mu\text{m}$  respectively, for the SWNTs. They also tested the MWNTs with open tips, for which the fields are  $4.5 \text{ V}/\mu\text{m}$  and  $30 \text{ V}/\mu\text{m}$  and graphitic fibres, for which the fields are  $5.6 \text{ V}/\mu\text{m}$  and  $14 \text{ V}/\mu\text{m}$ . A very high threshold field is observed in the case of MWNTs with open tips. Bonard et al. also compared the field emission of two different structures of nanotubes i.e. SWNTs [124] and MWNTs [130]. For SWNTs the turn-on field is in the range of  $1.5\text{-}4.5 \text{ V}/\mu\text{m}$  and threshold field range is  $3.9\text{-}7.8 \text{ V}/\mu\text{m}$ . By taking average emission from 12 nanotubes the turn-on and threshold fields become  $2.8 \text{ V}/\mu\text{m}$  and  $5.2 \text{ V}/\mu\text{m}$ . These are compared with MWNTs field emission, in another paper by the same group [130]. The fields are  $2.6 \text{ V}/\mu\text{m}$  and  $4.6 \text{ V}/\mu\text{m}$ , which are slightly lower than SWNTs.

This comparison shows that different structures have slight effects on the field emission behaviour of CNTs. In almost all the cases, high emission currents are obtained at low voltages except in the case of MWNTs with open tips for which the threshold field is  $30 \text{ V}/\mu\text{m}$ .

### *2.2.1.3 Effect of CNT Density and Aspect Ratio on Field Emission*

The density of CNTs is an important factor which affects number of CNT properties. The field emission behaviour is also influenced by the density of CNTs. In most of the literature, the density of the CNT is divided in three main categories i.e. high density, moderate density, and low density. There is no specific number to define these three categories, but it depends on area of the substrate, aspect ratio (height/diameter), and distance between two CNTs which is called intertube spacing.

Bonard et al. [136] tested the field emission dependence on the density of the CNTs. They have used three samples with low density, medium density and high density MWNTs grown by CVD process. All other parameters were kept same in the three samples except density of the CNTs. They reported the turn-on and threshold voltages of 9.8 V/ $\mu\text{m}$  and 14.4 V/ $\mu\text{m}$  in the case of low density CNTs. The high density CNTs showed better results with turn-on voltage of 3.6 V/ $\mu\text{m}$  and threshold voltage of 5.3 V/ $\mu\text{m}$ . But the best field emission was observed in the case of moderate density CNTs which is with 2.2 V/ $\mu\text{m}$  and 3.3 V/ $\mu\text{m}$  turn-on and threshold voltages respectively. The reason for high turn-on and threshold voltages (low emission) in the case of low density CNTs is the less number of CNTs on the electrode. Due to low density, the CNTs are very far apart from each other and the intertube spacing is very large. For the high density CNTs, better field emission is observed because of large number of CNTs on the electrode. But, in high density case the field emission is not as good as in the case of moderate density CNTs. The reason is very dense CNTs on the electrode. The moderate density CNTs has best emission with low turn-on and threshold fields. The reason is that the number of CNTs on the electrode is neither very small (so that the actual number of emitting sites become low) nor very large (so that electrostatic screening effect occurs). In the moderate density CNTs, the intertube spacing should be large enough to keep the tips of the CNTs away from each other. When CNTs are far apart, screening doesn't occur and the field amplification takes place. But, the intertube distance should not be very large so that the number of CNTs become very less and emission becomes low. Although, very large intertube spacing reduces the electrostatic screening effect completely but, in this case the actual

emitting sites are also less. Hence, intertube spacing should be a compromise between the two extremes so that best results can be obtained.

Uptill now, the range of CNT density is described in a very crude form i.e. high, moderate, and low. No numerical number is given in these ranges. After discussing the factors which affects the CNT density range, it is now easy to give idea about the actual number of CNTs on the electrode. By this time the reader can easily understand why these numbers are increasing and decreasing. The typical CNT density on the electrode is  $10^8$ - $10^9$  / $\text{cm}^2$ , which is considered as highly dense. In a report by Teo et al. [137] the number given for highly dense CNTs is  $10^9$  / $\text{cm}^2$  out of which  $10^4$  / $\text{cm}^2$  CNTs were actually contributing to the field emission. In another report by Bonard et al. [130], they also reported CNT density on the electrode is  $10^9$  / $\text{cm}^2$ , which is considered as highly dense. Due to this high density, the actual number of emitting sites reduces to  $10^4$  / $\text{cm}^2$  at the turn-on field which increases to  $10^6$  / $\text{cm}^2$  at the threshold field. In some other reports as well [120, 138-139], the emitting sites reduces to  $10^3$ -  $10^4$  / $\text{cm}^2$  at the turn-on field, if the actual CNT density on the electrode is  $10^8$ - $10^9$  / $\text{cm}^2$ . By these numerical numbers from the literature, it is observed that if the CNT density is very high then the actual emitting sites are reduced by a factor of around  $10^5$  / $\text{cm}^2$ . Now, to give some idea about the number of CNTs in the low density range, we recall the above discussion. We have already discussed above from [136] that the turn-on and threshold fields are very high (9.8 and 14.4 V/ $\mu\text{m}$ ) in the case of low density CNTs and comparatively low (3.6 and 5.3 V/ $\mu\text{m}$ ) in the case of high density CNTs. That means the total number of CNTs in the low density range is very much less compared to the actual emitting sites in the case of high density CNTs. So, we can say that if the density of CNTs is below  $10^3$  / $\text{cm}^2$ , it can be considered as low density of CNTs on the electrode. Hence, the range for moderate density of CNTs is below  $10^8$  / $\text{cm}^2$  and above  $10^3$  / $\text{cm}^2$ .

It is already discussed that array of CNTs can be capable of delivering current up to few A/ $\text{cm}^2$ . But, in the literature several reports can be found in which the individual CNT current is reported. The individual MWNT can deliver  $\sim 50$  pA-1 nA in the turn-on region and  $\sim 10$  nA-0.2  $\mu\text{A}$  in the threshold region [130]. In another

report by Manohara et al. [126], it is mentioned that an individual CNT can produce up to 30 nA of current.

In literature, many groups reported the improvement in emission property of CNTs by reducing electrostatic screening effect. As clear from the above discussion that electrostatic screening effects are reduced by optimizing the intertube spacing and controlling the height and diameter of the CNTs. Many groups have reported the theoretical [140-141], simulated [142] and experimental [143-145] data on the reduction of electrostatic screening effects. Nilsson et al. [140] in 2000, reported based on the theoretical work that the optimum field emission performance could be achieved when the intertube spacing is equal to two times height of the CNT. Many researchers in the field cited this work and it was remain true until few years. This work was in variance with the experimental studies performed in 2002 [143] and 2004 [144] in which it is reported that the maximum field emission occurs when the intertube spacing is equal to height of the CNT. But Nilsson's work is in accordance with the Teo et al. [137] work which also showed experimentally in 2002, that the intertube spacing should be twice the height of the CNT for best emission. In 2007, Smith et al. theoretically predicts that the residual screening of the order of 11% remains in the array if the intertube spacing is equal to two times height of the CNT. According to them, the electrostatic screening effect is reduced to minimum when the intertube spacing is equal to five times height of the CNT. These predictions were based on the two dimensional model. In 2009, the same group reported based on the three dimensional model that to reduce the electrostatic screening effects and best field emission, intertube spacing of three times height of the CNT is required. The latest report on the reduction of electrostatic screening (according to our knowledge) is by Jia Yun et al. [145] in which the diameter, height, sharpness, and the intertube spacing is controlled during fabrication. They proved experimentally that the field emission performance is optimized when the intertube spacing to tube height ratio is equal to 1 (intertube spacing is equal to height of the CNT). Their results are in line with other experimental results reported by Suh et al. [143-144] but different from the theoretical predictions made by Nilsson [140] and Smith [141-142].

We can summarize the above discussion with few words that the fabrication process, structure, and density and aspect ratio affects the field emission property of CNTs. With proper fabrication processes and controlling the structure and density of CNTs better field emission can be obtained. But, controlling these parameters is a difficult task. During fabrication, it is not possible to control all these parameters simultaneously and to change these parameters during experiments. In this research project we are trying to provide a solution to this problem by modelling the field emission property of CNTs.

Although, number of research papers are available in this field but in most of the papers results are different from others. As, only 20 years of research is available on CNTs from which most of the research is in the past 10 years so there are still lot of research opportunities available. Numbers of parameters are still unexplored and people are trying to get the best results. But overall, we can conclude that field emission is excellent from almost all types of CNTs.

### **2.2.2 Field Enhancement due to Nanomaterials**

As already discussed, high electric field region is created near the sharp tips of the carbon nanotubes. In this high electric field region, the gas atoms are ionized more easily than anywhere else between the electrodes. If carbon nanotubes are not present, a very high voltage (thousands of volts) is required to maintain this high electric field region between the electrodes. Without carbon nanotubes, the field is uniform between the parallel plate electrodes and is equal to the applied field, given by Eq. (2.3). But with the help of carbon nanotubes increase in the field is observed at a very low applied voltage. This increase in the field at a very low voltage is called field enhancement. The quantity used to measure this field enhancement is called the field enhancement factor ( $\beta$ ). The field enhancement factor can be defined as the ratio of the effective electric field to the applied field, given by Eq. (2.15).

$$\beta = \frac{E_{eff}}{E_{app}} \quad (2.15)$$

In Eq. (2.15), the effective field is the enhanced field achieved at the tips of the nanomaterials and the applied field is due to the external applied voltage. The effective field which is achieved near the tips of the nanomaterials is multiplied several times with respect to the applied field. This multiplication factor can be measured with the help of  $\beta$ .

Beside other factors, the effective field is also influenced by the electrostatic screening effects. The electrostatic screening effects reduce the effective field achieved at the nanomaterials tips. One of the reasons for the production of electrostatic screening effects is the high density of the nanotubes. If the density of the nanotubes is moderate or low, there is a sufficient intertube spacing and the electrostatic screening effects are reduced. Besides intertube spacing, the height of the nanotubes also affects the electrostatic screening. There should be a compromise between the height of the nanotube and the intertube spacing to reduce the electrostatic effects to a greater extent. To summarize the discussion it can be concluded that the height of the nanotube is related to the intertube spacing, the intertube spacing is related to the electrostatic screening, and electrostatic screening reduces the field enhancement at the nanomaterials tip. Hence, the height of the nanotube affects the field enhancement factor  $\beta$ .

On the other hand, the field enhancement is also affected by the tip diameter. The field enhancement can be increased if the nanotubes have sharp pointed tips. However, the large tip diameter reduces the effective field which eventually reduces the field enhancement factor. Hence, the two parameters i.e. height and the tip diameter, which defines the geometry of the nanotubes has great influence on the field enhancement factor.

Several models have been developed to describe  $\beta$  based on the geometry of the nanomaterial. A well established and widely used formula to describe  $\beta$  was developed by Forbes et al. [146] in 2003 and was named *hemisphere on post model*. The model gives an estimate of  $\beta$  based on the geometry of the nanotube. This model is used for the closed-end nanotube for which the free end of the nanotube is a solid hemisphere that sits on a cylinder which might be singly or multiply walled. The

cylinder in turn sits perpendicularly on a flat plate. The equation based on this model to estimate  $\beta$  is given by Eq. (2.16).

$$\beta = 1.2 \left( 2.15 + \frac{h}{r} \right)^{0.9} \quad (2.16)$$

where,  $h$  is the height and  $r$  is the radius of the nanotube. The Eq. (2.16) will be used in chapter 5 to calculate  $\beta$ . The calculated value of  $\beta$  will be compared with the  $\beta$  obtained from the simulations using our field emission model of carbon nanotubes. The simulated value of  $\beta$  obtained from our model will also be compared with the published values of  $\beta$  obtained from the existing ionization gas sensors. This comparison will provide the practicality of our model and the authenticity of the results obtained from the simulations.

### 2.3 Modelling and Simulation

Modelling is the process of producing a model. The model can be defined in various ways depending on different conditions. In engineering, model can be defined as the simplified representation of a system at some particular point in time or space intended to promote understanding of the real system. The purpose of the model is to easily analyze changes in the real system. For this reason, the model should always be a simpler form of the real system. But beside simplicity, model should be a close representation of a real system and includes most of its salient features. In short, a good model should be developed keeping in mind both the accuracy and simplicity. With engineering view point, the models are usually developed mathematically with the help of some software tool and can be one of the types or combination of the following types.

- Deterministic model, in which the input and output variables are fixed values.
- Stochastic model, in which atleast one of the input or output variables are probabilistic.
- Static model, in which the time is not taken into account.
- Dynamic model, time-varying interactions are taken into account.

The simulation is the manipulation of a model in such a way that it operates in time or space to compress it and to perceive the interactions that would not otherwise be apparent because of their separation in time and space. In simple words, the simulation is the operation of a model to extract information on the behaviour of real system under different conditions over long periods of real time. Simulation is usually referred to the computerized form of the model which is run to study the implications of the defined interactions. When one develops a model and run the simulations based on that model, the output of the model appears. The model can be revised based on that output. This iteration continues until the adequate level of understanding is developed.

### **2.3.1 Advantages and Disadvantages**

The modelling and simulation has number of advantages:

- i. The main advantage of modelling and simulation is the user can get practical feedback while designing the real world system. This allows the user to optimize the design to improve the efficiency of the system.
- ii. Another big advantage is the cost effectiveness. During design phase the effects of specific design decisions are investigated rather than the construction phase and overall cost of building the system diminishes significantly. Simulations take the building/rebuilding phase out of the loop by using the model already created. Most of the time, the simulation testing is cheaper and faster than performing the multiple tests of the design each time.
- iii. One more advantage of the modelling and simulation is the level of detail that can be achieved from simulation. Simulations can provide results which itself or the details of which cannot be experimentally measureable due to equipment limitation. Sometimes while taking the results experimentally, number of events happen very quickly and it is not possible to catch each one of them e.g., a breakdown process in ionization gas sensor. In this case, simulations can be set to run for as many time steps as desired and the useful information can be extracted.

Beside its number of advantages, the modelling and simulation have their disadvantages as well.

- i. The main disadvantage is the simulation errors. The authenticity of the results depends on the credibility of the model. As discussed above, the model should be simple and real. To overcome this issue some important steps can be taken. The first step to ensure the model provides correct results is to run a base line simulation to prove that it works. Secondly, the model to be accepted in the general community, some experimental results should be simulated. If the two data sets are comparable then any further simulations done on the same model will have some credibility. The emphasis is given on these points in this project.
- ii. Another disadvantage of the simulation is the fact that it is simulation. Many people do not consider the project until they hear, feel, and see the real system. The reason is the difficulty level to imagine virtual environment. Sometimes, it is not as easy to imagine behaviour of the system as it is in the real world. The virtual world is difficult to get use to, especially for the first time.
- iii. One more disadvantage of the simulation is the computation time. Some simulators require computationally intensive processing. As a consequence the results of the simulation need large time to compute. An event that may occur instantaneously in the real world may actually take hours to mimic in a simulated environment. The delays may be due to an exceedingly large number of entities being simulated or due to the complex interactions that occur between the entities within the system being simulated. Consequently, these simulators are restricted by limited hardware platforms which cannot meet the computational demands of the simulator. One of the ways to resolve this issue is to introduce simplifying assumptions or heuristics into the simulator engine. While this technique can dramatically reduce the simulation time, it may also give its users a false sense of security regarding the accuracy of the simulation results. However, this problem can be of less concern if more powerful platforms and improved simulation techniques are used.

To conclude this talk on advantages and disadvantages of modelling and simulation we can say that the only restrictions in the simulations are the imagination, programming skills, and the CPU. If these issues are resolved then the sky isn't even the limit.

### 2.3.2 Plasma Simulation Techniques

Particle modelling started with pioneering work in the late 1950s and early 1960s [147-150]. This work has shown that by using appropriate methods relatively small systems of a few thousand particles can indeed simulate accurately the collective behaviour of real plasmas. Since then, the development of new algorithms and the availability of more powerful computers have allowed particle simulation to progress from simple electrostatic problems to more complex and realistic situations.

Computer simulations of plasmas comprises of two general areas based on kinetic and fluid descriptions as shown in Fig. 2.13. The *fluid* simulation proceeds by solving numerically the magnetohydrodynamic (MHD) equations of plasma assuming approximate transport coefficients. On the other hand, *kinetic* simulation considers more detailed models of the plasma involving particle interactions through the electromagnetic field. This is achieved either by solving numerically the plasma kinetic equations e.g. Vlasov or Fokker Planck equations or by *particle* simulation, which simply computes the motion of a collection of charged particles, interacting with each other and with externally applied fields. Vlasov called his particles *clouds*. Vlasov equation is a particle simulation technique using integration of the collisionless kinetic equation which treats phase space as a continuum (which is an approximation). This approach does avoid statistical errors present in particle simulation, and has been used successfully. Vlasov simulation has not so far proven to be as adaptable as particle simulation.

Both *fluid* and *particle* simulation are well developed disciplines, which have become an integral part of plasma physics. The comprehensive overview of fluid, particle, and hybrid simulation techniques are given below to better understand the capabilities and limitations in these techniques. Beside limitations in these modelling

techniques, an intelligent selection of the plasma model can lead to better agreement between experimental and simulated environments.

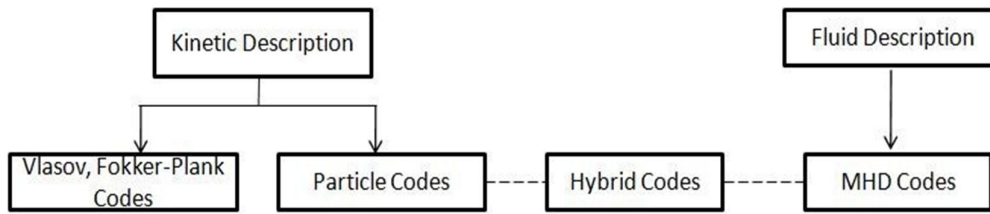


Fig. 2.13 Classifications of computer simulation models of plasmas

### 2.3.2.1 Fluid Models

The early work on fluid models have started in late 80s and early 90s [151-154]. This work have zero-dimensional (dealing with uniform quantities) or one-dimensional simulations of capacitively coupled discharges [155]. At that time the computer resources were limited and the basic emphasis was on the work to validate and improve the modelling techniques by studying fundamentals of plasma physics. The fluid models describe the plasma based on the density, mean velocity and mean energy of the constituent species. These models treat all the species as fluids so they are not very accurate in describing the particle kinetics. The major assumption made in these models is that the velocity distribution is based on the local value of the electric field. This makes them very less useful while dealing with the non-local effects of the particle kinetics. These models are more suitable where the non-local effects are less important especially at high pressure discharges. At high pressure discharges the non-local effect are of less concern due to the frequent collisions between the particles.

As these models are not involved in the detailed particle kinetics so the computation time is very less. The two-dimensional and three-dimensional models can be run in reasonably short time. Moreover, large number of species can be modelled using fluid technique which allows the simulation of complex chemistries.

### 2.3.2.2 Particle-In-Cell Monte-Carlo Collision (PIC-MCC) Models

The PIC-MCC technique is originally developed by the Plasma Theory and Simulation Group (PTSG) of University of California Berkeley [156-157]. The group is working under the leadership of Prof. C. K. Birdsall since five decades. In this period they have developed number of plasma simulation codes. Initially, the simple and straight codes for the plasma simulation were developed. With the passage of time and with the availability of modern sophisticated computers, the simple work has transformed into the more complex codes.

The PIC-MCC is a numerical simulation technique which caters the motion of charged particles and the collisions between charged and neutral particles along with the boundary effects. The charged particles are moving due to the forces produced by collisions and the applied field. The physics behind this model consists of two parts. In first part, the field produced by the particles is considered. The second part consists of the motion produced by the forces (or fields). The fields are calculated from Maxwell's equations by knowing the positions and velocities of all the particles. The forces on the particles are found using the electric and magnetic fields in the Newton-Lorentz equation of motion. For field calculation, the input sources to the Maxwell's equation are the current and charge densities. The current and charge densities are calculated with respect to the initial position and velocity of the particles and the fields are calculated for the same position and velocities. Then, particles are forced to move small distances and current and charge densities, and fields are recalculated at the new positions and velocities of the particles. This procedure repeats for as many time steps as desired.

In particle simulations, all the species are treated as particles and hence, more detailed description of particle kinetics is provided. In PIC simulations, reduced number of computer particles (also called super particles) are simulated which represent large number of real particles [157-159]. Usually, hundreds of thousands of computer particles are simulated and each particle represents hundreds of thousands of real particles. So, total number of simulated particles is up to thousands or millions. The position, velocity, current, charge, force, and fields are calculated for all the particles simultaneously in each time step. The time step is of the order of picosecond

or femtosecond. Hence, the computation complexity is a major concern in these simulations. The computation time is proportional to the number of super particles. The large number of simulated particles also limits the number of species that can be modelled. With the availability of high speed computers, the computationally efficient techniques and bounded models to embed statistical processes and particle collision (MCC module) were also developed in mid-1990s [160-161]. Regardless of any effort to cope up with the computation time, still PIC-MCC models require very large computation time. On the other hand, as they capture more details of particle kinetics so, provide more accurate results than the fluid simulations.

In PIC-MCC statistical processes are modelled in more detail as compared to fluid simulations. The fundamental equations are solved with very few approximations so, kinetics of the simulated species can be accurately modelled including both local and non-local effects. PIC-MCC simulations were performed on parallel and cylindrical electrodes and provided important understanding of non-local effects in capacitively coupled discharges [156, 162-163]. Therefore, these simulations are well suited for low pressure discharges where non-local effects are very important.

#### 2.3.2.2.1 Integration of Equation of Motion

The two first order differential equations for the particle motion are given by Eq. (2.17) and Eq. (2.18).

$$m \frac{dv}{dt} = F \quad (2.17)$$

$$\frac{dx}{dt} = v \quad (2.18)$$

where  $F$  is the force on the particle and has two parts i.e. electric and magnetic. The force  $F$  is given by Eq. (2.19).

$$F = qE + q(v \times B) \quad (2.19)$$

These equations are integrated separately for each particle. For example, if we have 100,000 particles and the simulation is to be run for 10,000 time steps, the equation of motion must be integrated  $10^9$  times. The equations are integrated using a commonly used integration method called leap-frog method. The sketch of the leap-frog method is shown in Fig. 2.14.

In leap-frog method, the Eq. (2.17) and Eq. (2.18) are replaced by the finite difference equations given by Eq. 2.20 and Eq. 2.21.

$$m \frac{v_{new} - v_{old}}{\Delta t} = F_{old} \quad (2.20)$$

$$\frac{x_{new} - x_{old}}{\Delta t} = v_{new} \quad (2.21)$$

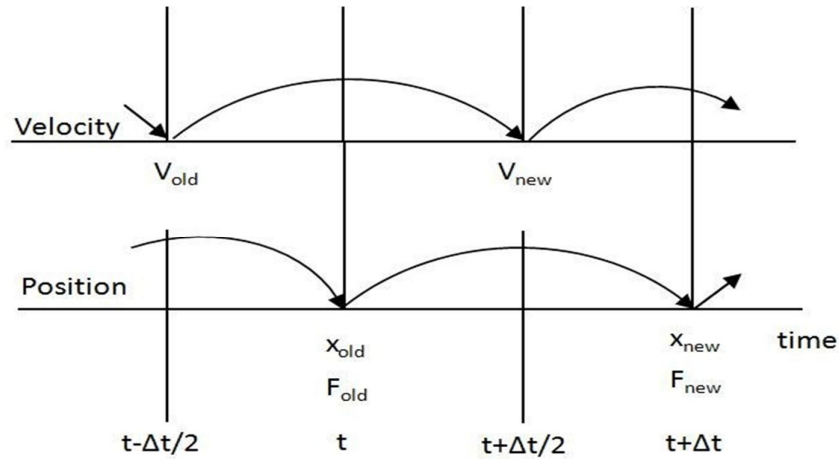


Fig. 2.14 Sketch of leap-frog integration method showing time-centering of force  $F$  while advancing  $v$ , and of  $v$  while advancing  $x$  [157]

The minimum information required for the integration is the particle position and velocity. These two parameters for every particle i.e.  $x_i$  and  $v_i$  are required for several previous time steps, where  $x$  is the position,  $v$  is the velocity, and  $i$  denotes the number of the particle. The computer will advance  $v_t$  and  $x_t$  to  $v_{t+\Delta t}$  and  $x_{t+\Delta t}$ , even though  $v$  and  $x$  are not known at the same time.

### 2.3.2.2.2 Integration of Field Equations

The electric and magnetic fields are calculated from the current and charge densities which are calculated at the grid points. The Maxwell equations, using  $\rho$  and  $J$  as sources, for 1-dimensional codes are given. The differential equations to be solved are

$$E = -\nabla\phi \quad \text{or} \quad E_x = -\frac{\partial\phi}{\partial x} \quad (2.22)$$

$$\nabla \cdot E = \frac{\rho}{\epsilon_0} \quad \text{or} \quad \frac{\partial E_x}{\partial x} = \frac{\rho}{\epsilon_0} \quad (2.23)$$

These differential equations are combined to obtain the Poisson's equation

$$\nabla^2\phi = -\frac{\rho}{\epsilon_0} \quad \text{or} \quad \frac{\partial^2\phi}{\partial x^2} = -\frac{\rho}{\epsilon_0} \quad (2.24)$$

A possible sequence for solving the Poisson's equation using the fast Fourier transform (FFT) and its inverse (IFFT) is summarized in Eq. 2.22.

$$\rho(x) \xrightarrow{\text{FFT}} \rho(k) \xrightarrow{k^2} \phi(k) \xrightarrow{\text{IFFT}} \phi(x) \xrightarrow{\nabla\phi} E(x) \quad (2.22)$$

This is a very powerful approach to solve the field quantities at the grid points for periodic systems. To keep things simple a detailed discussion on the solution of Poisson's equation is not provided. However, the details of this method along with several other solutions can be found in [157].

### 2.3.2.3 Hybrid Models

The hybrid models combine both fluid and PIC-MCC techniques. The idea was to use the fast speed of fluid models along with the accurate particle kinetics of PIC-MCC. The end result is that hybrid models are an intermediate form of these two models. They are faster than the PIC, but slower than the fluid models. As far as particle kinetics is concerned so, hybrid models are more accurate than fluid, but less accurate than the PIC models [155].

In literature, various forms of hybrid models are available. In some cases, ions (which are heavy) are considered as fluid and electrons as particles [164]. In other cases, only high energy electrons are treated under PIC scheme, while ions and low energy electrons are considered as fluids [165-166]. Hybrid models have their own issues e.g. the communication between the fluid and particle parts of the model. The major problem arises in defining the time step requirements which are quite different in both the models. However, by considering some educated predictions, these issues can be resolved to some extent.

At this stage a brief overview of these plasma simulation techniques is enough to select the appropriate technique for our work. It is already mentioned in the concluding remarks of section 2.1, that local and non-local effects both are important to support gas breakdown in ionization gas sensor. Hence, our selection of the simulation technique is straight forward i.e. PIC-MCC. The complete process flow and working of the PIC-MCC model is provided in detail in chapter 4. Although, we can select the hybrid models as well but, accuracy of the particle kinetics is preferred over the expensive computation in this project. To cope with the large computation times, a high performance workstation is dedicated to do simulation work.

To end up the modelling and simulation section it is important to mention here that, within all three branches of plasma study i.e. experimental, theory, and computation, a great deal of care is required. The care should be enough to obtain the essence of the problem, but not so much as to inhibit achieving any result [157].

## **2.4 Summary**

In this chapter an effort is made to provide comprehensive literature review on the main fields of this project i.e. gas sensors, CNT and its field emission property, and plasma simulation. Different types of latest gas sensors are discussed and details of ionization gas sensor are provided. The breakdown criterion is discussed in the light of Townsend mechanism and Paschen's law. Useful data on field emission property of CNT is provided and its role in ionization gas sensor is discussed. Some equations which govern the field enhancement of nanomaterials and breakdown conditions in

ionization gas sensor are also provided. Last part of this chapter is devoted to the modelling and simulation studies. The plasma simulation techniques, which are in use, are discussed and PIC-MCC is selected as the simulation technique based on the requirements of this project. The few basic equations of PIC-MCC codes are discussed. Although, there are number of complex equations and their solver modules running behind the PIC-MCC codes but, few equations in a simple form are presented.

## CHAPTER 3

### METHODOLOGY

#### **3.0 Overview**

The chapter starts with detail description of the PIC-MCC simulation technique. This is followed by benchmarking of codes using planar and cylindrical electrodes and explanation of simulation parameters. The enhancement of standard PIC-MCC codes and the detail description of the new model is provided. The process flow of the three new modules is discussed in detail. Furthermore, the criterion of carbon nanotube density calculation on the electrode is also provided. The simulation conditions and parameters to test the model are given along with every section to provide the insight of the overall simulation procedure.

#### **3.1 PIC-MCC Codes**

One of the pillars of this research is the simulation tool. PIC-MCC is selected as the simulation technique for this research based on the literature survey described in chapter 2. The PIC-MCC technique consists of two modules, i.e. Particle-in-Cell (PIC) along with Monte Carlo Collision (MCC) module. In a broad sense, PIC can be defined as a numerical method to examine the behavior of charged particles. While, MCC is a numerical method to cater the collisions between charged and the neutral particles. Hence, PIC-MCC is a numerical simulation technique to examine the behavior and to compute different parameters of plasma.

There are number of plasma computation codes available based on PIC-MCC technique [160, 167-168]. These codes are developed by the Plasma Theory and

Simulation Group (PTSG) of University of California Berkeley. Among these codes, the *Plasma Device Planar 1-dimensional with three velocity components* (XPDP1) [160] and *Plasma Device Cylindrical 1-dimensional with three velocity components* (XPDC1) [160] are used in this research project. The XPDP1 and XPDC1 packages contain the input file and the source codes. The input file contains almost hundred parameters related to the device structure and the gas species. Out of these parameters, the user defines certain parameters depending on the requirements of the simulation. The source codes are running at the backend controlling numerous tasks ranging from plasma physics and field calculations to the appearance of the graphs in the output windows. These source codes are written using the computer programming language C with the object oriented approach.

### 3.1.1 PIC-MCC Process Flow

The process flow of the working mechanism of PIC-MCC technique is shown in Fig. 3.1. In this technique, the simulation space is bounded by two electrodes which have planar or cylindrical shape. The simulation space between these electrodes is divided into number of cells creating a grid as shown in Fig. 3.2. The species (charged and neutral particles) to be simulated are defined in the input file. All the initial information about the species e.g. density, pressure, number of particles etc. and about the device structure e.g. area, gap spacing, voltage or current sources, number of cells etc. are also defined in the input file. The particles with these initially defined parameters are loaded into the bounded simulation space. These particles are called *computer particles* or *super particles*. The computer particles are reduced number of real particles. Typically, the number of computer particles is in the range of hundreds of thousands and each computer particle represents almost the same number of real particles. The parameter which specifies the relation between computer particles and real particles is also defined in the input file.

When particles are loaded in the simulation space, every particle is tracked with the Newton Lorentz equations of motion and assigned initial position and velocity. Every particle is assumed to be in the boundary of the cell. According to the position and velocity of the particle, current and charge densities are calculated at the grid

points. This technique is called weighting particles to the grid. A number of weighting techniques can be employed [169-172] e.g. zero-order weighting, first-order weighting, and higher-order weighting. In zero-order weighting, the particles are weighted to the one nearest grid point. The number of particles within the distance of half cell width on both sides of the grid point is counted and that number is assigned to the grid point. According to the number of particles, the current and charge density is calculated at the grid point. The density value increases or decreases depending on the particles coming in or going out in that particular cell range. In first-order weighting, the particles are weighted to the two grid points. This technique requires additional computation in accessing two grid points for each particle. In higher-order weighting, the particles are weighted to the four grid points. This technique is very accurate in terms of computation but requires large time. To compromise between the computer efficiency, physical representation and simulation noise, a zero-order weighting is typically used in PIC simulations.

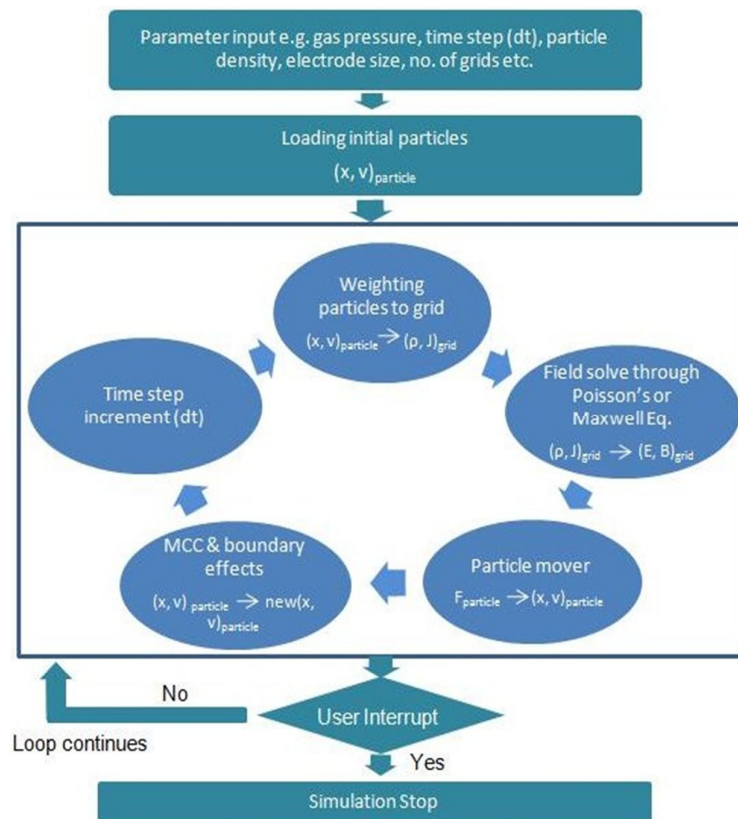


Fig. 3.1 The flow diagram of Standard PIC-MCC Model

The current and charge densities are converted at the grid points to electric and magnetic fields with the help of Maxwell's or Poisson's equations. All these parameters are calculated without making any assumption on the velocity distribution and the kinetics of each species are calculated with very little approximation.

After the calculation of electric and magnetic field at the grid points, force on the individual particle is calculated. This technique is called weighting grid to the particle. Every particle moves with that force with the help of particle mover module. When the particles move, they collide with each other. The MCC module caters collisions between the particles statistically. The interaction of the particles with boundary electrodes is also taken into account by incorporating effects of reflection, absorption, and emission of the particles at boundaries. In MCC module, the particles undergoing collision are randomly selected in each time step. The programming is done in such a way that the particle which collides once is shifted to the end of the array so that it should not be selected twice for the collision. When a collision between two particles takes place its type is determined by the collision cross section which is the most fundamental characteristic of all elementary processes. There are elastic and several inelastic collisions defined in the source codes to take place. Typically, for ion-neutral collisions, scattering, excitation, and ionization, whereas for electron-neutral, scattering and charge exchange is present. After completing the MCC module and boundary effects procedure, the Newton Lorentz equations of motion are applied and the new position and velocity is assigned to the particles. At this stage, one loop is completed and the time step is incremented. The same procedure continues in the next time step. All the parameters mentioned above are calculated for all computer particles simultaneously in each time step. The time step is usually of the order of picoseconds or below making the PIC-MCC simulations computationally very expensive [157].

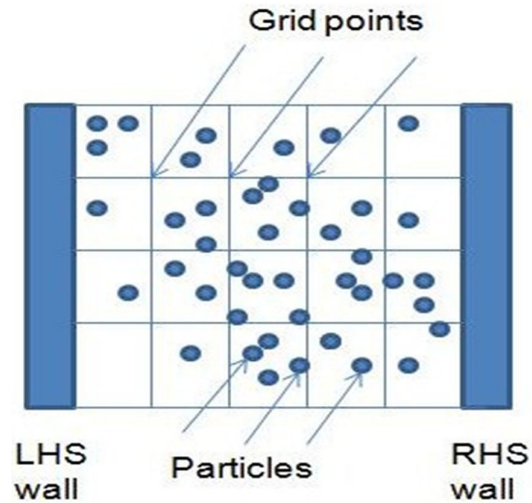


Fig. 3.2 Simplified bounded simulation space with planar electrodes. LHS wall and RHS wall are used to distinguish the two electrodes

### 3.2 Benchmarking

As the codes XPDP1 and XPDC1 are used in this project, the detail knowledge of these source codes and understanding of working mechanism is necessary. In order to gain enough understanding, the work is started with the benchmarking. The goal of benchmarking is to run the base line simulations and to validate results with published data. The benchmarking is divided in two phases. In the first phase, XPDP1 codes are used to simulate electron densities during discharges in argon and in the second phase, XPDC1 codes are used to simulate breakdown voltages of argon.

#### 3.2.1 Simulation of Electron Densities

Electrons are main energy carriers and are responsible for the formation of plasma by the process of ionization. They have a mass few orders of magnitude less than the mass of ions and neutral particles and have high mobility. Due to these properties electrons gain energy from the electric field and distribute this energy for all the processes and mechanisms which take place in the discharge region. The rate of these

processes depends on the number of electrons which have sufficient energy to perform the specific task.

In order to determine role of electron densities in the discharge phenomenon we have used XPDP1 codes to simulate the *capacitively coupled radio frequency (CCRF)* discharge in argon gas. The simulated device structure is shown in Fig. 3.3.

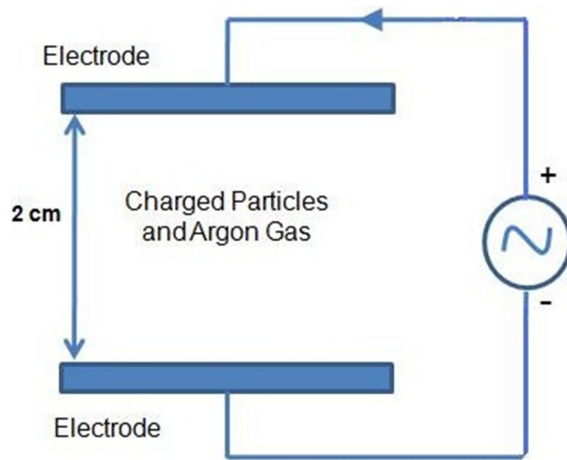


Fig. 3.3 The simulated device structure of XPDP1

There are certain parameters in the input file which need to be assigned proper values to get desired results. The values of some of the important parameters are shown in Table 3.1.

Table 3.1 Parameter values used for the simulation setup of section 3.2.1

Parameter	Assigned values
No. of spatial cells	400
Area	0.142 m <sup>2</sup>
Gap Spacing	0.02 m
Source	AC

Current density	2.65mA/cm <sup>2</sup>
Frequency	13.56 MHz
nc2p	3.266 x 10 <sup>7</sup>
Number of species	2 (Electrons and Argon)
Initial density of each species	1.74810 <sup>15</sup> / m <sup>3</sup>
Gas Pressure	0.1 – 0.5 Torr
Initial gas temperature	0.026 eV (room temp.)
Time step	8 ps
Codes	XPDP1

Using parameters in Table 3.1, the discharge in the device shown in Fig. 3.3 is simulated at various gas pressures ranging from 0.1 Torr to 0.5 Torr. Number of simulation runs were performed by changing the gas pressure every time but the gap spacing between the electrodes is kept constant in all the cases. The number of cells is 400 which are in accordance with the gap spacing of 0.02 m. The width of each cell can be calculated by Eq. (3.1).

$$Cell\ width = \frac{Gap\ Spacing}{No.\ of\ cells} \quad (3.1)$$

Using Eq. 3.1, the width of each cell is determined to be  $5 \times 10^{-5}$  m. If number of cells is very large and the gap spacing is small then, the width of the cell becomes small. The small cell width makes the grid points close to each other and the number of particles in each cell decreases. Although, it gives more accurate results because particles are weighted to the grid and fields are calculated at the grid points. But, the computation time increases. Hence, the number of cells should be large enough to

give correct results in a reasonable time. The number of computer particles is calculated by Eq. (3.2).

$$\text{No. of computer particles} = \frac{\text{Area} \cdot \text{Gap spacing} \cdot \text{initial density}}{nc2p} \quad (3.2)$$

where  $nc2p$  is the parameter in the input file which represents the number of real particles per computer particle. The total number of computer particles calculated by Eq. (3.2) is 152,000. This makes the total real particles to be  $4.96 \times 10^{12}$ . The time step is 8 ps. There are number of factors involved in selecting the time step of the simulation [156, 173]. The time step should be smaller than the maximum collision frequency  $v_{\max}$  of the particles. This prevents the particles from undergoing more than one collision in one time step. If the particle collides more than once in one time step, it is hard for the source codes to identify the type of collision. It may end up with the wrong computation of plasma parameters.

### 3.2.2 Simulation of Breakdown Voltages

Breakdown voltage ( $V_{bd}$ ) is the fundamental parameter to detect gases in ionization gas sensor. The breakdown mechanism has been introduced in chapter 2. As the breakdown voltages are of significant importance throughout this thesis, it is necessary to run some initial simulations of the breakdown behaviour in a gas and to validate the simulation results with published data. The emphasis is on the comparison of acquired results with experimental published data to make a good understanding and to increase the confidence level of the research to proceed further.

In this second phase of benchmarking, the XPDC1 codes are used to examine the breakdown behavior of argon gas. In these simulations the breakdown is examined in two types of fields i.e. combined RF and DC field and in DC field. In XPDC1, there are two cylindrical bounding electrodes located at  $r_1$  and  $r_2$  as shown in Fig. 3.4.

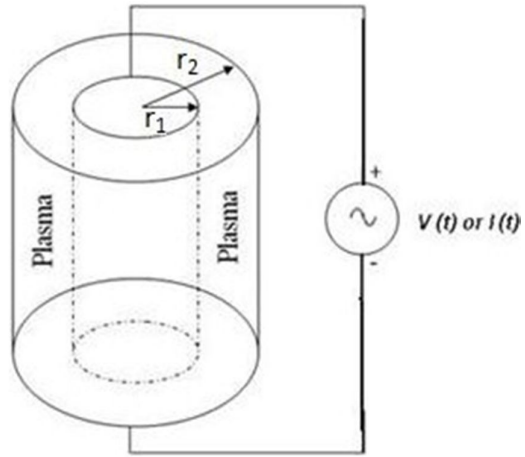


Fig. 3.4 The simulated device structure of XPDC1

The values of some important parameters in this simulation are given in Table 3.2.

Table 3.2 Parameter values used for the simulation setup of section 3.2.2

Parameter	Assigned values
No. of spatial cells	500
$r_1$	0.027 m
$r_2$	0.05 m
Gap Spacing	0.023 m
Height	0.1 m
DC Source	0 – 600V
Combined DC and RF source	0 -300 V AC and 25 V DC
Frequency	13.56MHz

nc2p	1 x 10 <sup>5</sup>
Number of species	2 (Electrons and Argon)
Initial density of each species	10 <sup>14</sup> / m <sup>3</sup>
Gas Pressure	0.1 to 1.3 Torr (DC field) 0.1 to 7.0 Torr (Combined fields)
Initial gas temperature	0.026 eV (room temp.)
Time step	10 - 50 ps
Codes	XPDC1

The gas pressure is varied from 0.1 Torr to 1.3 Torr in the case of DC field and from 0.1 Torr to 7.0 Torr in the case of combined RF and DC fields. In the case of combined fields the frequency is 13.56 MHz and a 25V of DC voltage is applied along with the AC source. The number of cells and the gap spacing is increased to 500 and 0.023 m respectively. The cell width can be calculated by the Eq. (3.3) if the uniform grid spacing is considered in the cylindrical electrodes.

$$Cell\ width = \frac{r_2 - r_1}{No.\ of\ cells} \quad (3.3)$$

The cell width of each cell is 4.6 x 10<sup>-5</sup> m. The initial density is reduced to 1 x 10<sup>14</sup> / m<sup>3</sup>. In XPDC1, new parameter added is the height of the cylinder. The number of computer particles can be calculated by Eq. (3.4).

$$No.\ of\ computer\ particles = \frac{(r_2^2 - r_1^2) \cdot \pi \cdot height \cdot initial\ density}{nc2p} \quad (3.4)$$

Using Eq. (3.4), the number of computer particles is calculated to be 5.56 x 10<sup>5</sup>. Each particle represents 10<sup>5</sup> real particles making total number of real particles to be 5.56 x 10<sup>10</sup>. The time step varies between 10ps to 50ps for different simulation runs to satisfy the time step requirements already mentioned.

After completion of the benchmarking phase, the adequate understanding of the two packages i.e. XPDP1 and XPDC1 was developed. Moreover, the role of electron density and other parameters in the gas breakdown phenomenon is also realized.

### 3.3 Simulation of Gas Breakdown in Different Devices

This simulation setup was run to examine the role of device structure in the gas breakdown. In this setup, the argon gas breakdowns were simulated in two different structures keeping all other parameters same in both the cases. The XPDP1 and XPDC1 packages are used with the same devices as shown in Fig. 3.3 and Fig. 3.4 respectively. The gap spacing is 0.023 m in both the cases and the gas pressure is varied from 0.1 Torr to 4.5 Torr. All the simulations are carried out in the DC field. The values of important parameters are given in Table 3.3.

Table 3.3 Parameter values used for the simulation setup of section 3.3

<b>Parameter</b>	<b>Assigned values</b>
No. of spatial cells	300
Area	0.0242 m <sup>2</sup> (XPDP1)
r <sub>1</sub>	0.027 m (XPDC1)
r <sub>2</sub>	0.05 m (XPDC1)
Gap Spacing	0.023 m
Height	0.1 m (XPDC1)
DC Source	0 – 600V
nc2p	1 x 10 <sup>5</sup>
Number of species	2 (Electrons and Argon)

Initial density of each species	$10^{14} / \text{m}^3$
Gas Pressure	0.1 to 4.5 Torr
Initial gas temperature	0.026 eV (room temp.)
Time step	50 ps
Codes	XPDP1, XPDC1

These parameters are almost the same as were in the previous case. According to the radii and height of the cylinders, the number of computer particles is  $5.56 \times 10^5$  in cylindrical electrodes. To achieve the same number of computer particles in planar electrodes, Eq. (3.2) is used, which gives the area of the planar electrode to be  $0.0242 \text{ m}^2$ . The number of cells is 300 and the time step is 50 ps.

### 3.4 Simulation of Breakdown Behavior in Different Gases

This simulation setup was run to examine the changes in the breakdown behavior of two different gases in the same type of device. In this setup, the planar device (XPDP1) shown in Fig. 3.3 is used with two gases i.e. argon and helium. All the simulations are carried out in the DC field. The values of the important parameters are given in Table 3.4.

Table 3.4 Parameter values used for the simulation setup of section 3.4

<b>Parameter</b>	<b>Assigned values</b>
No. of spatial cells	300
Area	0.0242 m <sup>2</sup>
Gap Spacing	0.023 m
DC Source	0 – 600V
nc2p	1 x 10 <sup>5</sup>
Number of species	2 (electrons and argon, electrons and helium)
Initial density of each species	10 <sup>14</sup> / m <sup>3</sup>
Gas Pressure	0.1 to 4.5 Torr (argon) 0.5 to 8.0 Torr (helium)
Initial gas temperature	0.026 eV (room temp.)
Time step	50 ps
Codes	XPDP1

The same parameters are used as was in the previous simulation setup with XPDP1 package. The helium gas is tested in the device with a pressure ranging from 0.5 Torr to 8.0 Torr. Two separate simulation setups were run for both the gases keeping number of species in each case to be two. Several simulations are run in each case by changing the gas pressure every time in the range given above. The breakdown voltages are calculated and the details of acquired results are discussed in chapter 4.

### 3.5 The Enhancement of Standard PIC-MCC Model

The existing codes, based on PIC-MCC technique, XPDP1 and XPDC1 are used in the previous simulation setups. These codes are used for benchmarking and to investigate the critical issues in the gas breakdown behavior. The devices in these existing codes, shown in Fig. 3.3 and Fig. 3.4, have plane bare electrodes. These packages are for general plasma simulation and do not contain the effects of nanomaterials on the electrode. However, the typical ionization gas sensor has nanomaterials grown on one of the two parallel electrodes. The objective of this thesis is to model the gas detection mechanism in carbon nanotube based ionization gas sensor. Hence to achieve the objective, the existing PIC-MCC package XPDP1 is required to be enhanced with a new model which contains carbon nanotubes on one of the electrodes. As the role of carbon nanotubes in ionization gas sensor is to provide high field emission, the new model should be able to cater for the field emission property along with the factors which affect field emission of the carbon nanotubes.

The enhancement of the existing model with field emission effects of carbon nanotubes was a challenging task. It required complete understanding of various fields e.g. existing source codes of XPDP1 package, field emission property of carbon nanotubes and their dependence on various factors, and computer programming using object oriented C. Moreover, the care should be taken in developing a new model that it should work properly with the existing XPDP1 package without affecting the basic functionality of the standard codes.

After comprehensive understanding of the XPDP1 source codes it was found that the module which contains the particle injection and loss mechanism is the *boundary effects module* working with the *MCC module*. As the field emission is due to the secondary electron emission from the boundary, this boundary effects module in the standard codes become the focal point of the work. The new model of carbon nanotube field emission should be embedded with this module in the standard codes.

Before discussing the new model, it is necessary to take a brief overview of the particle injection and loss in the standard model. The simplified process flow of the standard PIC-MCC model is shown in Fig. 3.5. The *MCC module* and the *boundary*

*effects module* which were shown together in the Fig. 3.1 are now shown separately to highlight the boundary effects module for particle injection and loss. The overview of functionality of this module is provided in the next section.

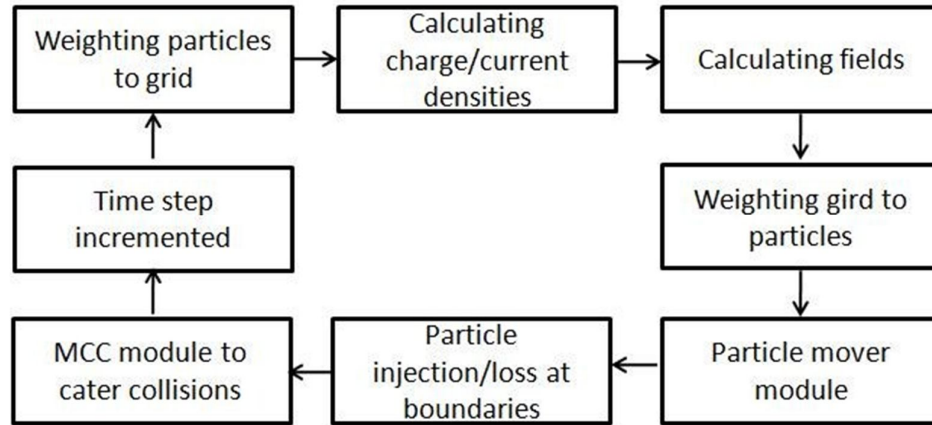


Fig. 3.5 The simplified flow diagram of Standard PIC-MCC Model. The MCC module and the boundary effects module are shown separately

### 3.5.1 Particle Injection and Loss in Standard PIC-MCC Model

This is the module which keeps track of all the particles which are emitted in the simulation space due to field emission or secondary electron emission. Secondly, it also keeps track of the particles which are lost in the electrodes. As we are dealing with the bounded plasma system the absorption and emission of particles from the walls is very important. To cater for absorption and emission there are two main parameters in standard XPDP1 codes i.e., *secondary* and *reflux*. In real systems, when voltage becomes very high (e.g. in kilovolt) the electrons are extracted from the plane metal electrodes due to tunneling process. The *secondary* parameter in simulation keeps track of all the secondary electrons emitted from the boundaries. This secondary emission can be from both the electrodes i.e. anode and cathode. The electrons which are injected in the simulation space are counted and the simulator keeps track of all the particles in each time step. Once, the particles are injected, the task is to assign the position and velocities to the newly injected particles. These velocities can be generated and assigned to the particle when the particle is injected,

or stored in an array before the particle injection and assigned to them as soon as they are injected.

In real systems, most of the particles striking the boundaries are absorbed in the boundaries. The reflux parameter in the simulation is used if the particles are to be bounced back into the simulation space after striking the walls but in real environment this does not happen. The simulator keeps track of the particles which absorb in the walls and delete these particles from the simulation space thus decreasing the total number of particles.

After this increment and decrement in the total number of particles in each time step, the new total number of particles is compared with the maximum number of particles defined by the user. If the total number of particles is more than the maximum number of particles, simulation exits. Otherwise, the time step is incremented and the same procedure repeats in the next cycle. Hence, the simulator is keeping track of the injected and lost particles in each time step simultaneously.

### **3.5.2 Carbon Nanotube Field Emission Model**

Keeping in view all these factors the new model was developed and embedded in the standard PIC-MCC codes i.e. XPDP1. The XPDP1 package containing the new model also works on the same PIC-MCC principle and is named *enhanced PIC-MCC model*. The modified codes for the enhanced PIC-MCC model are given in Appendix-A. The simulation space of the enhanced form of XPDP1 package is shown in Fig. 3.6. It is similar to the device of standard XPDP1 package shown in Fig. 3.2 but, with the effects of carbon nanotube field emission model. The flow diagram of enhanced PIC-MCC model is shown in Fig. 3.7. The new field emission model of the carbon nanotubes is embedded in between the *boundary effects module* and *MCC module* of the standard model. If there is a need to put the effects of the field emission of carbon nanotubes, the control goes to the new model from the *boundary effects module*. After putting the effects of carbon nanotube field emission property the control of the program comes back to the standard PIC-MCC codes at the MCC module. But after the control returns back to the standard model, it takes all the effects of the new model

with it. That means every parameter in the standard model is now calculated by taking the effects of the new model into account.

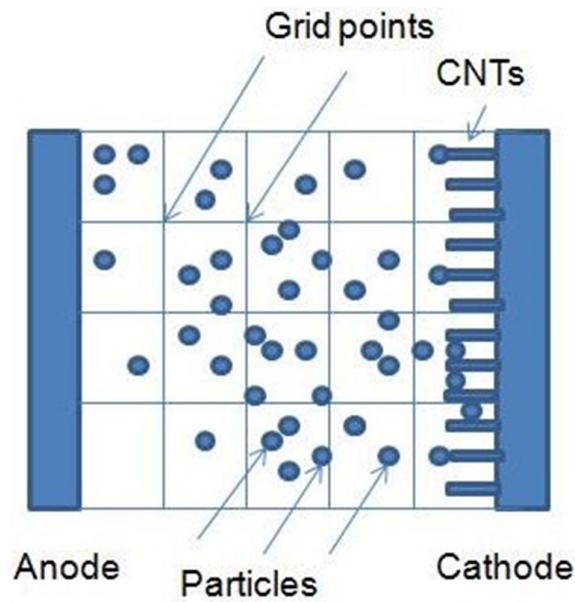


Fig. 3.6 The simplified bounded simulation space with planar electrodes and carbon nanotubes on the cathode

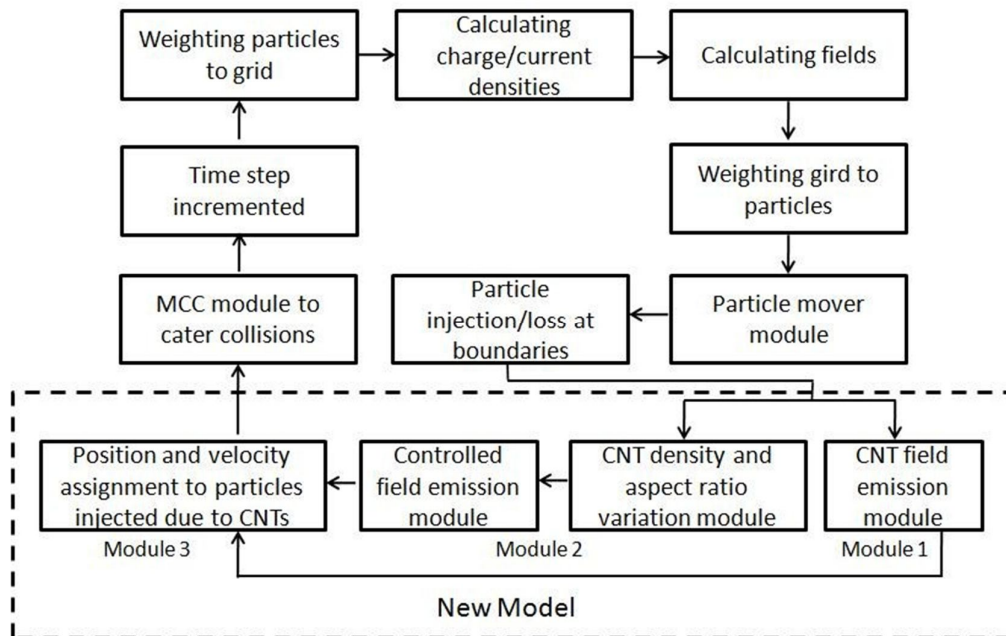


Fig. 3.7 The flow diagram of Enhanced PIC-MCC Model

The flow diagram in Fig. 3.7 shows that the new model is mainly divided into three modules. These modules are *CNT field emission module*, *CNT controlled field emission module with density and aspect ratio variations*, and *position and velocity assignment module*. The programming for all these modules is done using the same computer programming language as used for the standard codes i.e. object oriented C. If the user desires to put the effects of carbon nanotube field emission the control goes to the *CNT field emission module*. After putting the field emission effects, the control is transferred to the *position and velocity assignment module*. The position and velocity is then assigned to the newly injected particles. Then the control is passed back to the standard model. However, if it is desired to control the field emission with respect to the carbon nanotube density and aspect ratio, the control goes to the *CNT density and aspect ratio variation module*. This module after putting the effects of controlled density and aspect ratio of the carbon nanotubes transfers the control to the *controlled field emission module*. This module provides controlled field emission with respect to the density and aspect ratio of the carbon nanotubes and transfers the control to the *position and velocity assignment module*. The *position and velocity assignment module* is designed in such a way that it works with both types of field emissions intelligently. The process flow and functionality of these three modules is discussed in detail.

### 3.5.2.1 CNT Field Emission Module

The objective of this module is to cater for the field emission property of carbon nanotubes. The source codes of this module contain various parameters out of which two parameters are user defined parameters and added in the input file. These two parameters are given below.

*nm* = nanomaterial parameter

*nmeec* = nanomaterial electron emission coefficient

The parameter *nm* can be assigned a value '0' or '1'. If the user wants to put the effects of CNT field emission in the simulations, this parameter is set to '1' and the control goes to the CNT field emission module. Otherwise, if this parameter is '0' the

simulation runs with the standard PIC-MCC model. If control comes to *CNT field emission* module, it provides the enhanced field emission due to presence of carbon nanotubes and transfers the control directly to the *position and velocity assignment* module. This process flow is shown in Fig. 3.7.

The primary role of carbon nanotubes is to enhance the field emission effects due to secondary electron emission. Each electron injected from the cathode produces number of ions and each ion hitting the cathode produces number of electrons. This process creates a positive feedback and leads to the gas breakdown. The electrons injected from the cathode are called the secondary electrons and their number depends on the Townsend's second ionization coefficient  $\gamma$ . Recalling the definition of  $\gamma$  from chapter 2,  $\gamma$  is defined as the description of the probability of the secondary electron emission on the cathode by an ion impact. To cater for  $\gamma$ , the parameter *nmeec* is introduced. The parameter *nmeec* is used to emit the electrons from the carbon nanotube electrode. If the value of this parameter is e.g. 0.5, then on average 5 electrons are injected for every 10 incident particles striking the carbon nanotube electrode.

The process flow of the CNT field emission module is shown in Fig. 3.8. This process flow provides an overview of the logic used in the source codes of CNT field emission module. The source code is divided into a sequence of sections. The codes are initialized to put the effects of carbon nanotube field emission. The scheme for injecting particles is built and the random number is generated. The random number is generated by the random number generator module which is already present in the standard model. The same random number generator module is used to generate the random number for CNT field emission module. The randomly generated number is compared with the *nmeec* to inject the electrons in the simulation space. After this comparison, the carbon nanotube electrode, which is cathode, is selected. The name of this electrode in the source codes is right hand side (RHS) electrode but, using this name doesn't have any technical reason. One important thing to mention here is the selection of cathode as the carbon nanotube electrode instead of anode. The reason is that the positive ionization takes place in the case of all non-attaching gases. These positive ions attract towards the cathode and produce more electrons due to the

presence of carbon nanotubes on the cathode. If carbon nanotubes are on the anode, the positive ions attract towards the cathode and hit the plane electrode in uniform electric field and number of electrons produced will be less in this case.

The field emission of carbon nanotubes is measured in terms of the current density which is different for turn-on field and threshold field. The current density is a physical parameter and it is converted to the computer parameter i.e. number of particles injected per second. The value of turn-on field and threshold field in the codes is set to  $0.75 \text{ V}/\mu\text{m}$  and  $1.6 \text{ V}/\mu\text{m}$  respectively. These values of turn-on field and threshold field are taken from the experimental data of Rao et al. [125]. The reason is that they tested their sample for  $10 \mu\text{m}$  of gap spacing and for ionization gas sensor we are also interested in the gap spacing of micrometer range.

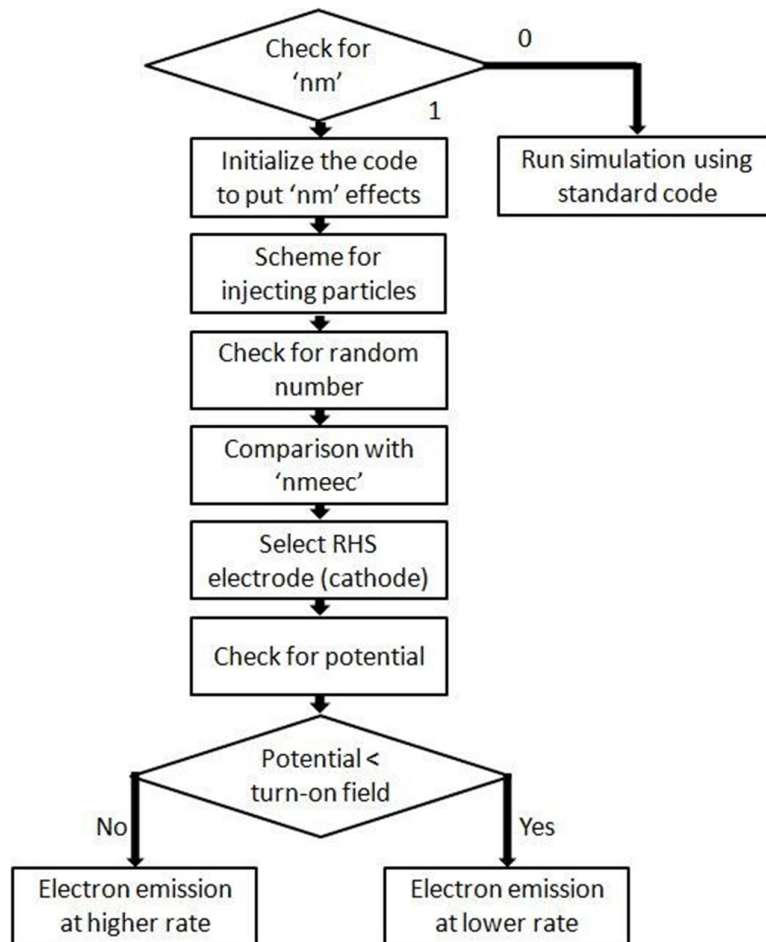


Fig. 3.8 Flow diagram of the source code logic of CNT field emission module

After selecting the cathode, the code checks the applied potential and decides the rate of electron injection. If the potential is less than the turn-on field which is  $0.75 \text{ V}/\mu\text{m}$ , the electron injection is at a lower rate. If the potential is higher than the  $0.75 \text{ V}/\mu\text{m}$ , the electron injection is at a higher rate.

### 3.5.2.2 CNT Density and Aspect Ratio Variation Module

As already described in chapter 2, the field emission property of carbon nanotubes is influenced by various parameters. Among these parameters, the density and aspect ratio of carbon nanotubes are the most important and has large affect on the field emission behavior. In this module, the source codes are written to cater the variations in these parameters and their effects on the carbon nanotubes field emission behavior. These two parameters are also related with each other. The aspect ratio is the ratio of the height to the diameter of the nanotube. The density of the nanotube is the number of nanotubes on the specified area of the electrode. If the density is low, the intertube spacing is large and if the density is high the intertube spacing is small. There is a need of some reference scale for the measurement of intertube spacing. In this work, the height of the nanotube is related to the intertube spacing as a reference scale.

Among various parameters which are declared in the source codes, the four parameters are made flexible to cater the variations in the density and aspect ratio. These parameters are given in the input file to be assigned values by the user and respective changes were made in the source codes. The parameters are given below.

*nm\_den* = nanomaterial density parameter

*nm\_d* = nanomaterial diameter

*nm\_h* = nanomaterial height

*int\_spc* = ratio of intertube spacing to tube height

The *nm\_den* is similar to the *nm* parameter in the *CNT field emission* module. If the user wishes to put the effects of carbon nanotube field emission which are controlled by the density and aspect ratio then this parameter is set to '1'. Otherwise, this

parameter should be '0'. If this parameter is set to '1' the control goes to the *CNT density and aspect ratio variation* module. This module calculates the carbon nanotube parameters based on the values defined by the user and transfers the control to the *controlled field emission* module. The *controlled field emission* module provides field emission based on the parameters calculated by the *CNT density and aspect ratio variation* module and transfers the control to the *position and velocity assignment* module. The details of the process flow are already provided in Fig. 3.7.

The flow diagram of the code logic for the *CNT density and aspect ratio variation* module along with *controlled field emission* is shown in Fig. 3.9. This module is also divided into sequence of sections. When user give values to the input parameters and transfers the control to this module, the codes are initialized to put the effects of carbon nanotube controlled field emission. The density of the carbon nanotubes on the electrode is calculated by using the aspect ratio, intertube spacing to tube height ratio, and the area of the electrode. As already described in chapter 2, the density is divided into three categories i.e. high, moderate, and low. Once the density is calculated by the codes, the next task is to find out the category in which this density value lies. The density is a strong function of intertube spacing which is related to the nanotube height. If the density is low or moderate, almost all the nanotubes contribute to the field emission. However, in the case of high density the actual emitting sites become low due to electrostatic screening effects (already described in chapter 2). If the density calculated by the simulator lies in the high density category, the option is provided in the codes to cater for the electrostatic screening effects and reduces the actual emitting sites. The current density produced by the carbon nanotubes is calculated based on the actual number of emitting sites in case of high density, and the total number of emitting sites in the case of moderate and low density. The current which is a physical quantity is converted to the computer quantity i.e. number of particles injected per second. These number of particles are adjusted according to the time step value of the simulation. The *nmeec* which was defined by the user in the previous module is now calculated based on the particles injected in the simulation space. Once *nmeec* is calculated, the previous module i.e. *CNT field emission module* runs and the same procedure follows to inject the particles in the simulation space.

But, in this case these injected particles are controlled by the density and aspect ratio of the carbon nanotubes.

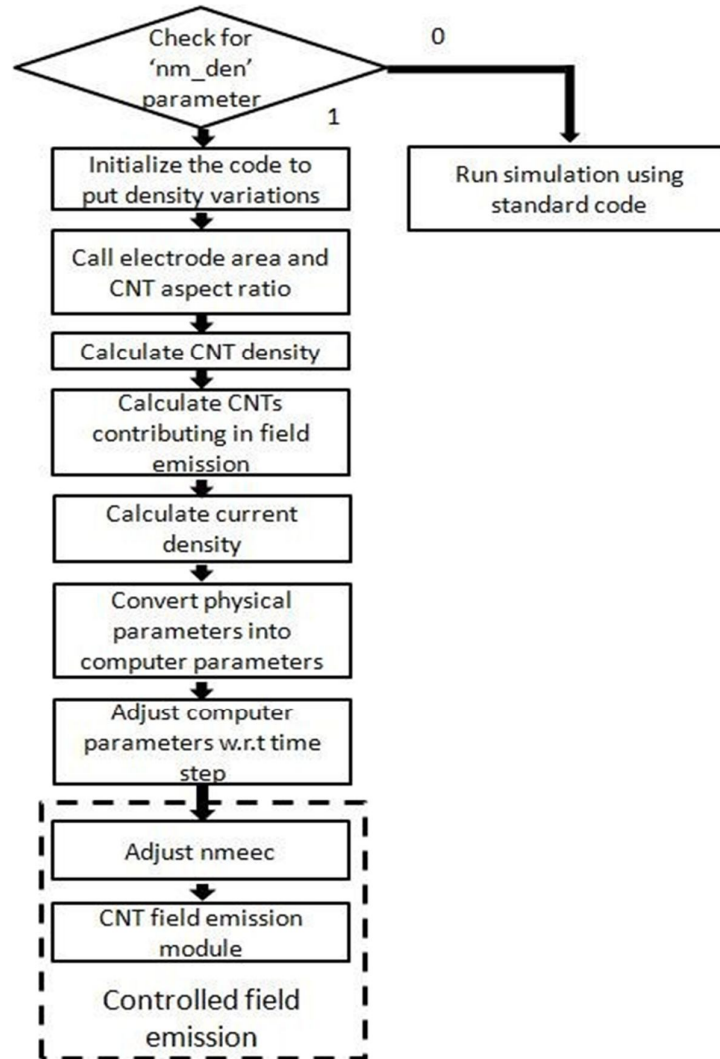


Fig. 3.9 Flow diagram of the source code logic of controlled field emission due to CNT density and aspect ratio variation module

### 3.5.2.2.1 Density Calculation Criteria

Most of the models are based on few assumptions which are taken into account to simplify those things which are very complex in reality. But, these assumptions should be made in such a way that they do not take things very far away from the reality. While developing this module few assumptions were taken keeping in mind the actual functionality of the real device. These assumptions are made in calculating the density of the carbon nanotubes on the electrode and described as follows.

- (i) The carbon nanotubes used in this model are vertically aligned with the same intertube spacing between all of them.
- (ii) The carbon nanotubes are completely round and have same height and diameter.
- (iii) The carbon nanotubes are grown in a square patterned array.

The carbon nanotubes with all these features mentioned in the assumptions are shown in Fig. 3.10. In this figure, the nanotubes top view is shown on an enlarged scale.

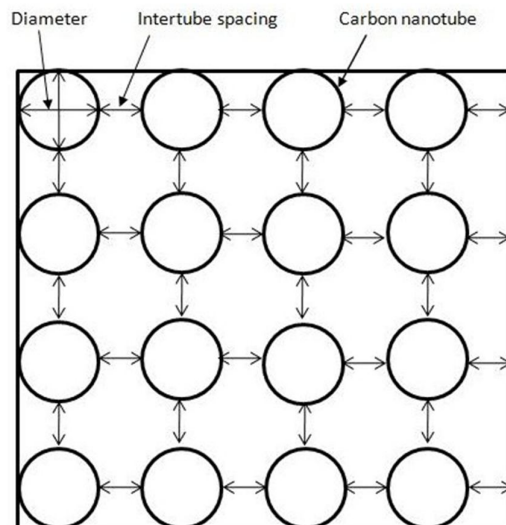


Fig. 3.10 Patterned square array of rounded carbon nanotubes with same diameter and intertube spacing between them

The density calculation in the codes with these assumptions is validated by comparing the density values with published experimental data [137]. In this published work, the carbon nanotubes are fabricated and their aspect ratios and densities are observed in the laboratory using high resolution equipment. As rest of the calculations in this module are dependent on the density parameter, it is very important to calculate the densities with correct procedure. The densities of the carbon nanotubes on the electrode are calculated several times with different aspect ratio and compared with the published data. All other parameters are kept same as in the published work to notice the change in the density parameter only. The details of the results will be provided in chapter 4.

### *3.5.2.3 Position and Velocity Assignment Module*

The simulator keeps track of every single computer particle in the simulation space. One of its task is to assign the position and velocity to the particles which are initially loaded before simulation started or injected during a run in the simulation space. In the new model, the particles injected during the run due to carbon nanotube field emission need to be assigned a proper position and velocity. As the name indicates, the *position and velocity assignment* module assigns position and velocity to these newly injected particles. This module is developed in such a way that it can work with both the previous modules separately. The flow diagram of this module is shown in Fig. 3.11. The *position and velocity assignment* module works as a slave module with its two master field emission modules described previously. This module waits for the signal from any of the two field emission modules. If the user set either of the two field emission modules to '1' in the input file and run the simulation, this *position and velocity assignment* module becomes active automatically.

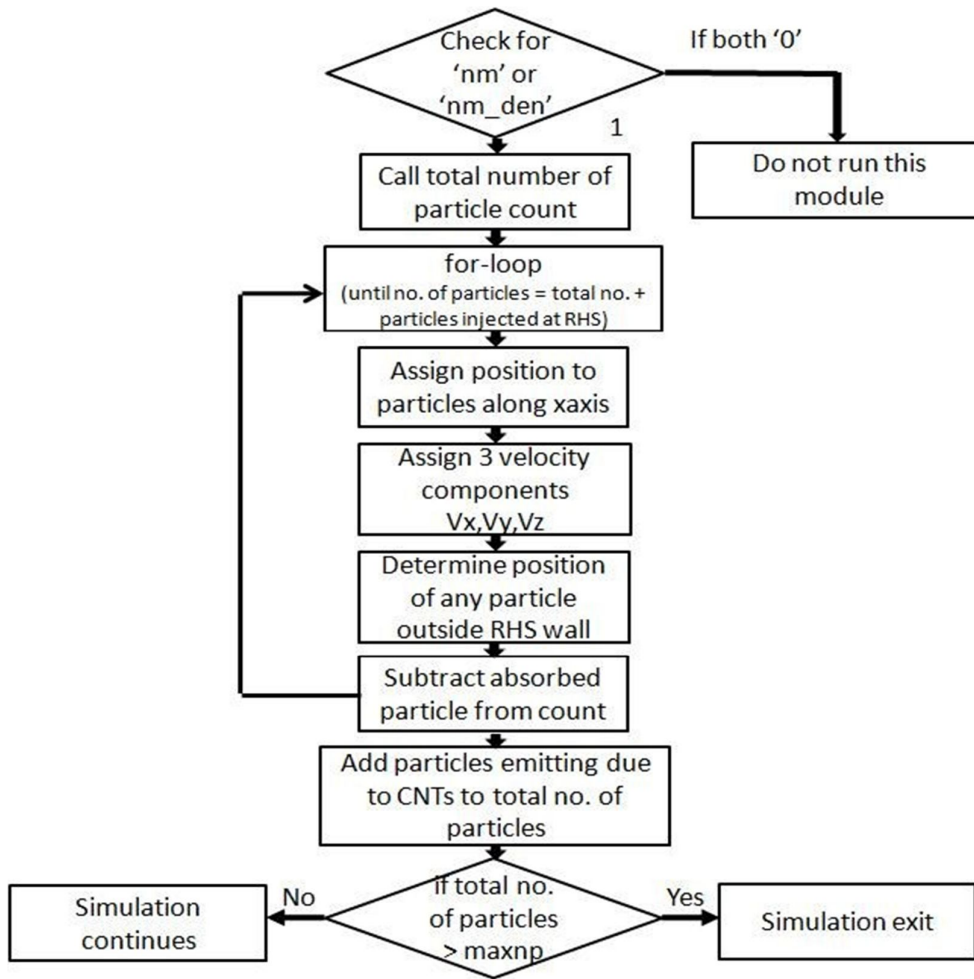


Fig. 3.11 Flow diagram of the source code logic of the position and velocity assignment module

It is important to mention here that this module assigns position and velocity to the particles injecting due to carbon nanotube field emission only. There are some other parameters in the standard codes which are responsible for the particle injection and absorption. These parameters are *secondary* and *reflux* respectively (explained previously). These parameters also affect the particle count. Along with this external injection of the particles, the increase in the number of particles is also due to the ionization within the boundaries. However, great care has been taken that position and velocities are assigned to the newly injected particles only due to carbon nanotubes field emission.

The module starts working by calling the total number of particles which are updated in the memory location in every time step. The *for-loop* is created with a condition that it will keep on executing until the number of particles become equal to the sum of the total number of particles called from the memory and the particles injected from the cathode due to carbon nanotube field emission. There are two advantages of this *for-loop*. Firstly, it separates the particles which are injected due to carbon nanotubes from all other injected particles (if any). Secondly, the condition of the *for-loop* keeps it working until the particles due to carbon nanotube field emission stop injecting from the electrode. This provides a surety that all the particles which are injected due to carbon nanotube field emission have been assigned position and velocity. In practice, the condition for stopping the *for-loop* doesn't meet because the particles keep on injecting from the electrode. The condition which temporarily stops this procedure is the time step. When the time step is incremented, the loop discontinues and the memory is updated with the new total number of particles which is the sum of total number of particles of the previous cycle and the particles injected due to the carbon nanotubes field emission in this cycle. Now, in the start of next cycle the module again calls for the total number of particles from the memory, which is already updated.

Until now, the overall functionality of this module and reasons for creating the *for-loop* are discussed. Now, the sections which are inside the *for-loop* are briefly discussed. Once the loop is created and the injected particles are distinguished, position is assigned to the particles inside the boundary of the cathode. The velocities are also assigned along with three velocity components i.e.  $V_x$ ,  $V_y$ ,  $V_z$ . For the position and velocity assignment, the same subroutines are used which are already present in the standard codes. After assigning the position and velocities, the loop also keeps track of those particles which are absorbed in the boundary just after injection and subtract these particles from the count. These particles are also subtracted from the total number of particles which are updated in the memory location in every cycle.

Another parameter which is already present in the input file in the standard codes is *maxnp* which is the maximum number of computer particles in the simulation space. The user defines this parameter and if the total number of particles in the

simulation exceeds the defined number of maximum particles, the simulation stops. This check is also included at the end of this module because now the particles due to carbon nanotube field emission are also contributing to increase the total number of particles in the simulation space.

The new field emission model of carbon nanotubes for ionization gas sensor has been developed and embedded in the standard PIC-MCC codes successfully. Now, the details of the simulation setups which are run to test the functionality of the new model are provided.

### 3.6 Simulation of Breakdown Voltages in Micrometer Gaps

In previous simulation setups the benchmarking is done for the centimeter range of gap spacing. Those simulation setups were run to keep the simulations simple and to understand the basic functionality of the standard models. But in real ionization gas sensor, the device dimensions are in micrometer range. Before testing the functionality of the new model in micrometer ranges, it would be more appropriate to benchmark the breakdown voltages in micrometer gaps without field emission model. It would provide a platform to compare the results of standard and enhanced models. The important parameters used in this simulation setup are given in Table 3.5.

Table 3.5 Parameter values used for the simulation setup of section 3.6

Parameter	Assigned values
No. of spatial cells	100
Area	$0.2 \times 10^{-6} \text{ m}^2$
Gap Spacing	10 $\mu\text{m}$
DC Source	0 – 100V
nc2p	$4 \times 10^4$

Number of species	2 (Electrons and Argon)
Initial density of each species	$7 \times 10^{21} / \text{m}^3$
Gas Pressure	300 Torr to 3800 Torr
Initial gas temperature	0.026 eV (room temp.)
Time step	0.05 ps
Codes	Enhanced XPDP1
<i>nm</i>	0
<i>nm_den</i>	0

From these parameters using Eq. (3.2), the number of computer particles is found to be  $3.5 \times 10^5$  which represents  $1.4 \times 10^{10}$  real particles. In this simulation setup, the simulated device is scaled down to micrometer range. The area is  $0.2 \times 10^{-6} \text{ m}^2$  and the gap spacing is reduced to  $10 \mu\text{m}$ . According to this small area and gap spacing the number of spatial cells is selected to be 100 and the initial density of the species is increased to the order of  $10^{21} / \text{m}^3$ . As already mentioned, the time step should be smaller than the maximum collision frequency of the particles. If we decrease the size of the device and increase gas pressure, the collision probability of the particles increases. Hence, the time step should be smaller. To cope up with this small scale device and to increase the accuracy of the results, the time step is reduced to 0.05 ps. The small time step took very large time to compute each case. As these simulations are run without the carbon nanotube field emission effects, the parameters *nm* and *nm\_den*, both are set to '0'. When these parameters are set to '0', the field emission effects are neglected and the enhanced codes behave like the standard XPDP1 codes.

This simulation setup is run to test the device for a wide range of gas pressure. The gas pressure range was varied from 300 Torr to 3800 Torr. The high pressure range up to few thousand Torr was selected according to the availability of published

data in this range of gas pressure. However, the low gas pressure range in few hundred Torr is selected keeping in view the functionality of real ionization gas sensor which works usually in the low gas pressure range. The breakdown voltages for various gas pressures were calculated and compared with the published simulated and experimental results. These simulations provide a baseline to test the functionality of the new modules in the micrometer range gap spacing as in real ionization gas sensor.

### 3.7 Simulation Setup based on Module 1

This simulation setup is run to test the functionality of the Module 1 (CNT field emission module) along with Module 3 (position and velocity assignment module). The simulated device is shown in Fig. 3.12.

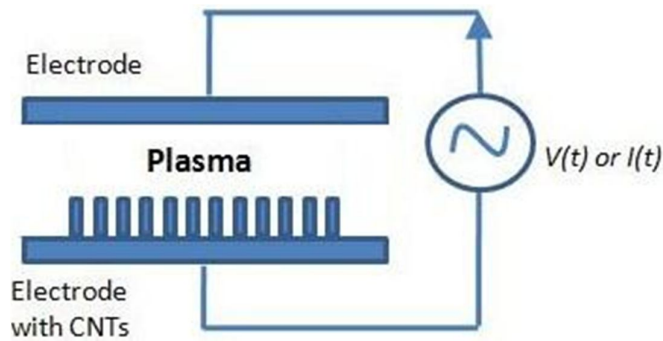


Fig. 3.12 The simulated device structure of Enhanced XPDP1

In these simulations, most of the input parameter values are same as was in the previous case. These parameter values are selected keeping in mind that the behavior of the modelled device should be as close to the real CNT based ionization gas sensor as possible. The values of some important parameters are given in Table 3.6.

Table 3.6 Parameter values used for the simulation setup of section 3.7

<b>Parameter</b>	<b>Assigned values</b>
No. of spatial cells	100
Area	$0.2 \times 10^{-6} \text{ m}^2$
Gap Spacing	6 - 12 $\mu\text{m}$
DC Source	0 – 100V
nc2p	$4 \times 10^4$
Number of species	2 (Electrons and Argon)
Initial density of each species	$7 \times 10^{21} / \text{m}^3$
Gas Pressure	300 Torr to 1400 Torr
Initial gas temperature	0.026 eV (room temp.)
Time step	0.05 ps
Codes	Enhanced XPDP1
nm	1
nm_den	0
nmeec	0.49

In Enhanced XPDP1, two new parameters *nm* and *nmeec* are added for the Module 1. The values for these parameters are given. After assigning the proper values to the parameters, the computer simulations were carried out. The simulations were run with variable gap spacing and argon gas pressure. Several simulations were run for each case to check the reliability and repeatability of the results. The

breakdown voltages were determined and some other parameters e.g. electron density, number of particles contributing in the breakdown phenomenon, and the ionization collisions were also observed.

Furthermore, the field enhancement factor  $\beta$  is calculated to check the integrity of the enhanced XPDP1 codes. The results were also compared and validated by the experimental published data available in the literature. It is also important to mention here that with these enhanced XPDP1 codes the simulation of gas breakdown behavior in CNT based ionization gas sensor become possible for the first time. The details of the results are discussed in chapter 4.

### 3.8 Simulation Setup based on Module 2

This simulation setup is run to test the functionality of Module 2 (CNT density and aspect ratio variation module) along with Module 3 (position and velocity assignment module). The important parameters in this setup are the aspect ratio parameters which are added in the new model. The objective of these simulations is to investigate the effects of density and aspect ratio variations on the field emission behavior of carbon nanotubes. These important parameters along with some other are given in Table 3.7.

Table 3.7 Parameter values for the simulation setup of section 3.8

<b>Parameter</b>	<b>Assigned values</b>
No. of spatial cells	100
Area	$0.2 \times 10^{-6} \text{ m}^2$
Gap Spacing	10 $\mu\text{m}$
DC Source	0 – 100V
nc2p	$4 \times 10^4$

Number of species	2 (Electrons and Argon)
Initial density of each species	$7 \times 10^{21} / \text{m}^3$
Gas Pressure	300 Torr to 1400 Torr
Initial gas temperature	0.026 eV (room temp.)
Time step	0.05 ps
Codes	Enhanced XPDP1
nm	0
nm_den	1
nm_d	$55 \times 10^{-9} \text{ m}$
nm_h	$5 \times 10^{-6} \text{ m}$
int_spc	1 - 5

Most of the parameters in this setup are the same as in the previous simulation setup. The same micrometer scaled device was simulated along with the effects of carbon nanotube field emission. The emphasis in this simulation setup was on the effects of density and aspect ratio parameters on the field emission behavior of carbon nanotubes. To achieve this goal, the parameters were given values accordingly. The parameter *nm\_den* was set to '1' to put the aspect ratio and density variation effects and *nm* was set to '0'. At a time, either of these two parameters can be set to '1' and the other should be '0'. If both of these parameters are set to '1', the option is provided in the new model to check this condition and exit the simulation. The proper message also appears on the screen to identify the problem to the user.

The other parameters e.g. *nm\_d* and *nm\_h*, which represent the diameter and height of the carbon nanotube respectively, are also tested by assigning different

values. Some typical values which are used initially for the benchmarking of the density calculation of carbon nanotubes are given in the list of parameters above. As already mentioned, the intertube spacing is related to the height of the nanotube. The parameter *int\_spc*, which is ratio of intertube spacing to tube height, is also assigned different values in different simulations and varied between 1 – 5.

All the computer simulations were carried out with constant gap spacing of 10  $\mu\text{m}$  and varying the argon gas pressure from 300 Torr to 1400 Torr. The effects of various parameters on the field emission behavior of carbon nanotubes were observed. Moreover, the variations in the breakdown voltage, electron densities, number of electrons etc. are also observed. The results of this section along with discussion on the graphs is provided in chapter 4.

### **3.9 Summary**

In this chapter, the methodology adopted in this work is explained. The project was divided into various sections. The functionality of the standard PIC-MCC model is described with the process flow diagram to provide detail understanding of PIC-MCC simulation technique. The benchmarking and simulation details using the standard PIC-MCC codes (XPDP1 and XPDC1) are provided. The simulation setup to understand the impact of electrode shape on the breakdown voltages is also given. The enhancement of PIC-MCC codes which is the main goal of this research is discussed in detail. The criteria to enhance the PIC-MCC model is given along with the model parameters. The process flow of the new model is described. The flow diagrams for the three new modules are explained to provide understanding of the code logic running behind these modules. The simulation setups and important parameters to test the functionality of the enhanced PIC-MCC model are given.

## CHAPTER 4

### RESULTS AND DISCUSSION

#### 4.0 Overview

This chapter is dedicated to the results and discussion part of the thesis. Results of all simulation setups described in chapter 4 are provided in the form of graphs and tables. The comparison of the results with published experimental and simulated data is given where required. The data analysis is also done which includes the calculation of correlation coefficients and the improvement factors. In the end, suggestions based on the results of the new model are given which provides a platform to improve the performance of ionization gas sensor.

#### 4.1 Electron Densities in Planar Electrodes

In first part of the benchmarking, the simulations were carried out using standard XPDP1 codes to study the CCRF discharges in argon gas. In this setup, number of simulations was run to observe electron densities by varying the gas pressure range. The gap spacing was kept constant, i.e. 2 cm, in all the cases.

The spatial profile of electron density between the two planar electrodes is shown in Fig. 4.1. In this graph, the y-axis shows the electron density and the x-axis shows the gap spacing between the electrodes, i.e. from 0 to 2 cm. It is observed that electron population is highly dense in the center and gradually decreases while moving away from the center of the gap spacing. Closer look at the graph reveals that less number of electrons is observed within the range of 0.4 cm from the two electrodes. As the ionization process depends on the availability of electrons with sufficient amount of energy, the ionization channel is also deep in the center and

shallow at the corners. The electron density is in symmetry from both sides of the device which clearly indicates the same amount of secondary electron emission from both the electrodes. The secondary electron emission is at a very low rate showing the less electron density near the electrodes. In addition, the device used in these simulations (shown in Fig. 3.3) has plane bare electrodes (without CNTs) which create uniform electric field in the space between them. This uniform electric field is responsible for the movement of electrons from cathode to anode at uniform velocities.

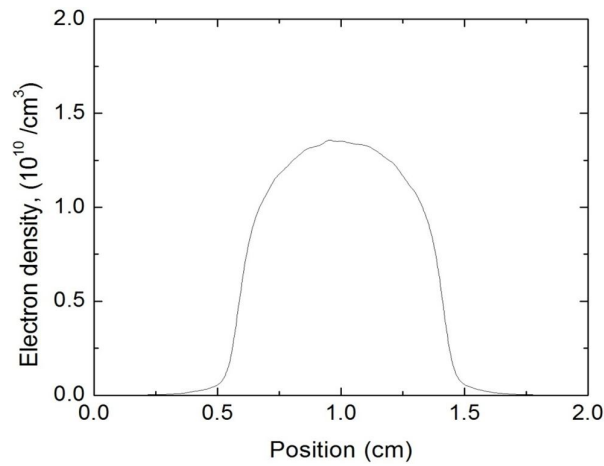


Fig. 4.1 The spatial profile of electron density in planar electrodes

The electron densities as a function of gas pressure are shown in Fig. 4.2.

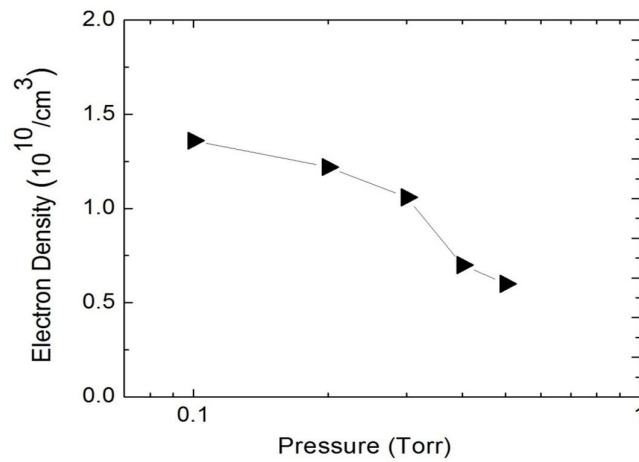


Fig. 4.2 Electron densities as a function of argon gas pressure

These electron densities are calculated when the CCRF discharge occurs in argon gas. The electron densities are on the y-axis and the gas pressure is varied from 0.1 Torr to 0.5 Torr along x-axis on a log scale. The graph clearly shows that the less electron densities are required for a discharge to occur if the gas pressure is increased. The increase in gas pressure increases the collision probability between the gas particles and charged particles. The increased number of collisions is responsible for the increase in ionization process and the increase in the electron heating process. This electron heating process at high gas pressure is called collisional heating process. On the other hand, at low gas pressure, the collision probability decreases which leads to the decrease in rate of ionization. In this case, the electron heating is due to the stochastic heating process. Hence, at low gas pressures, high electron densities are required for the occurrence of the discharge.

According to Godyak et al. [174], the transition from the collisional heating process to stochastic heating process occurs at a gas pressure of around 0.35 Torr. The transition occurs at almost the same gas pressure in the simulations in the graph of Fig. 4.2. Furthermore, the simulation results of Fig. 4.1 and Fig. 4.2 are compared with the published experimental [174] and simulated [175] data. The comparison of the graphs is shown in Fig. 4.3 and Fig. 4.4. The parameters which are available in the published work are kept the same in these simulations to make the simulation setup as close to the published work as possible. Some parameters which are not mentioned in the published work are assigned the appropriate values according to the simulation criteria. It can be concluded from the graphs of Fig. 4.3 and Fig. 4.4 that the same trend is observed in the results of this simulation setup and the results of other published experimental and simulated works.

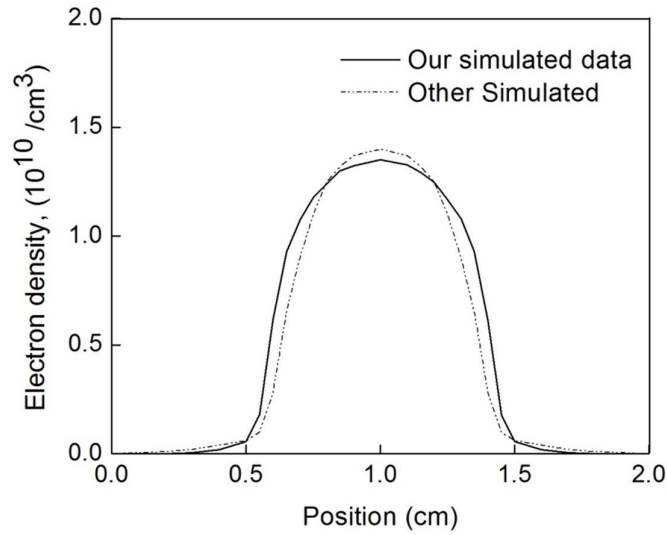


Fig. 4.3 The spatial profile of electron densities in planar electrodes. Comparison of our simulated data with other simulated data [175]

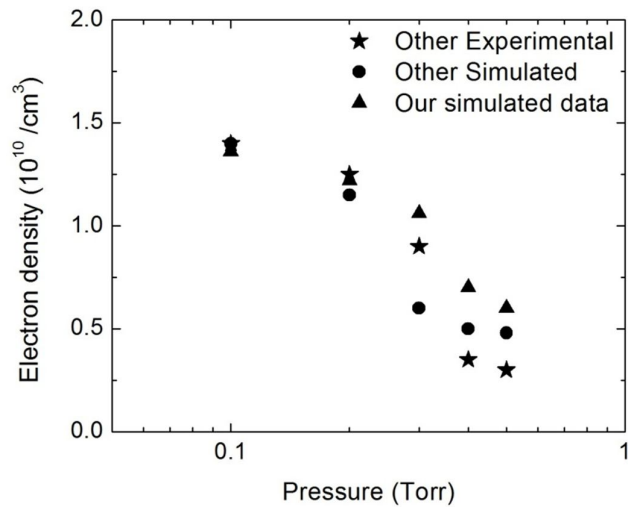


Fig. 4.4 Electron densities as a function of argon gas pressure. Comparison of our simulated data with other experimental [174] and simulated [175] data

Correlation coefficient is then determined using the data from our simulations and the data from [175], which is plotted in Fig. 4.3. This correlation coefficient can give a measure of the degree of closeness of both graphs. The correlation coefficient for our simulated data and the data of [175] is found to be 0.9784. The correlation coefficient for the comparison of data of our simulations and the data from [174] and

[175], which is plotted in Fig. 4.4, is 0.9946 and 0.904 respectively. The correlation coefficient is '1' if the two datasets match completely. The obtained correlation coefficients in our data analysis are close to '1' which increases the confidence level to use these codes for further simulations.

## 4.2 Breakdown Voltages in Cylindrical Electrodes

In the second part of the benchmarking, the simulations are carried out using XPDC1 codes to calculate the breakdown voltages. The behavior of gas breakdown is examined using argon in two types of applied fields i.e. combined RF and DC field and DC-only field. The gap spacing between the cylindrical electrodes is kept constant i.e. 2.3 cm and the breakdown voltages are determined by varying the gas pressure. The method used to determine the breakdown voltages is the same as used by Marija et al. [176] and is described by Yu P. Raizer [112]. The gas breakdown is not an instantaneous phenomenon. It occurs over finite period of time and is determined by the balance between creation and removal of electrons only if the field is maintained for a sufficiently long time, adequate for producing numerous generations of electrons. The breakdown voltages as a function of gas pressure in combined RF and DC fields are shown in Fig. 4.5.

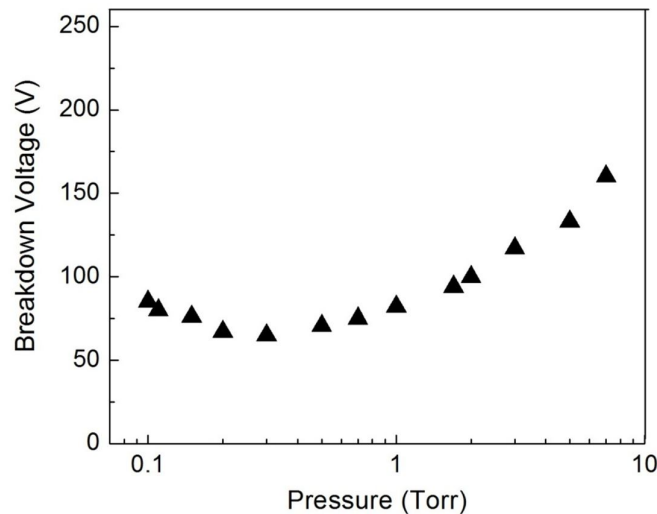


Fig. 4.5 Breakdown voltages as a function of gas pressure in combined RF and DC fields.

In this case, the gas pressure is varied from 0.1 Torr to 7.0 Torr. It is clearly shown in the graph that the U-shaped Paschen's curve is obtained. The details of Paschen's Law are described in chapter 2. By decreasing the gas pressure from 7.0 Torr the breakdown voltages are decreasing and below 0.3 Torr of gas pressure the breakdown voltages are again increasing, making a U-shaped Paschen's curve. It is observed from the graphs that the minimum breakdown voltage is obtained at gas pressure of around 0.3 Torr.

The breakdown voltages as a function of gas pressure in the case of DC-only field are shown in Fig. 4.6.

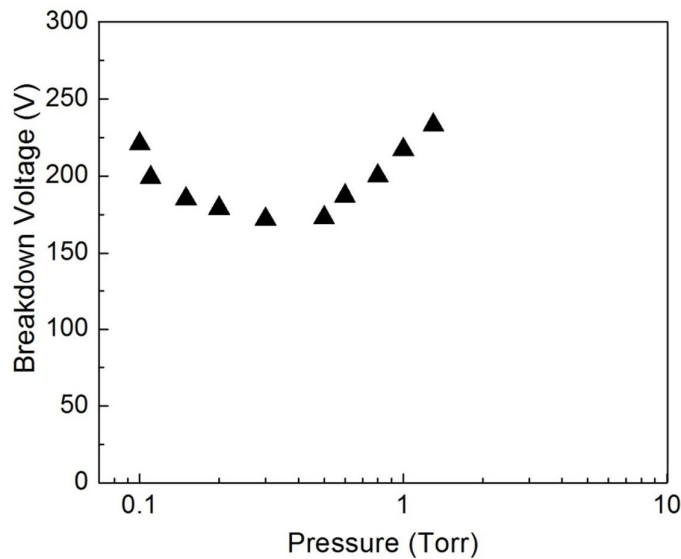


Fig. 4.6 Breakdown voltages as a function of gas pressure in DC-only field

In this graph of Fig. 4.6, the same U-shaped Paschen's curve is obtained. The gas pressure is varied from 0.1 Torr to 1.3 Torr and the gap spacing is constant i.e. 2.3 cm. A prominent decrease in the breakdown voltages is observed while decreasing the gas pressure from 1.3 Torr to 0.3 Torr. In this case also, the minimum breakdown voltage observed from the graph is at gas pressure of 0.3 Torr.

In Fig. 4.5, the breakdown voltages are in the range of 70 V to 160 V. However, in the case of DC-only discharges in Fig. 4.6, the breakdown voltages are in the range

of 170 V to 230 V. In a low gas pressure range of 0.2 Torr to 0.5 Torr, the breakdown voltages are low by around 100 V in the case of combined RF and DC fields. This voltage difference increases to around 150 V at a gas pressure of 1 Torr. Overall, it is observed that the lower breakdown voltages can be obtained by applying the combined RF and DC fields. The reason is the oscillatory energy gained by the electrons with the help of RF field along with large number of ionizations due to the DC field.

The gas pressure, at which the lowest breakdown voltage is observed, can be verified by using the minimum breakdown condition for Paschen's Law given by Eq. (2.13). The gap spacing  $d$  is 2.3 cm,  $e$  is 2.72,  $A$  is constant which is 12 for argon, taken from [112], and  $\gamma$  is 0.08 for argon, taken from [177]. Using these values in Eq. (2.13), the value of gas pressure for which the breakdown voltage is minimum is found to be 0.26 Torr. This theoretically calculated value of gas pressure is very close to the value observed from the graph of the simulation results. The slight difference in these values, i.e. 0.04 Torr, is acceptable which can be due to the slight variation in some of the simulation parameters. After investigating the cause of this difference it was found that the data on  $\gamma$  are incomplete and contradictory [112]. The uncertainty usually occurs in the values of  $\gamma$  because of the fact that  $\gamma$  is normally found in the formulas only within the logarithm. As a rule, one assumes that value of  $\gamma$  can be from 0.1 to 0.01 [112].

In order to further verify the results, the graphs of Fig. 4.5 and Fig. 4.6 are compared with the published experimental and simulated data. The comparison is shown in Fig. 4.7 and Fig. 4.8.

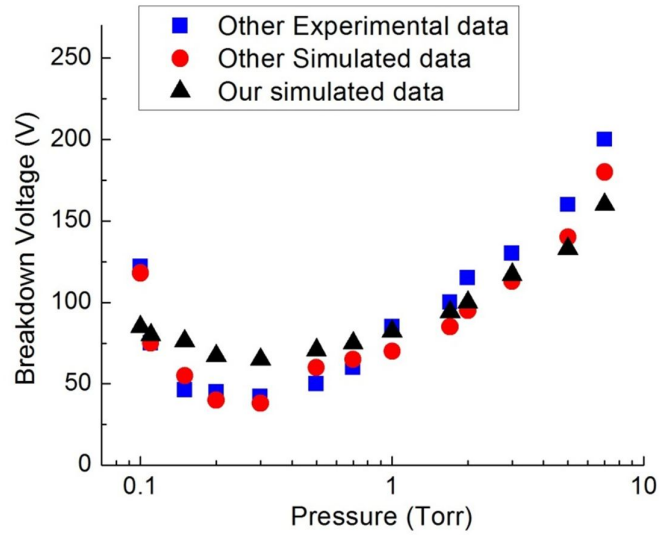


Fig. 4.7 Comparison of breakdown voltages with published experimental [178] and simulated [177] data in combined RF and DC fields

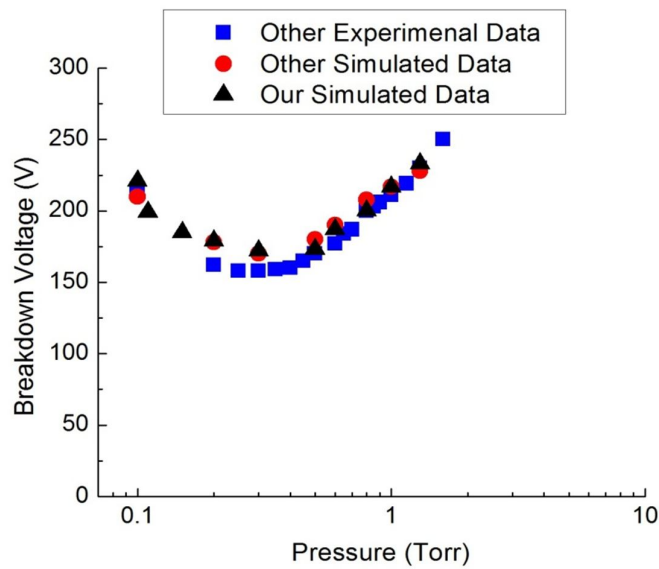


Fig. 4.8 Comparison of breakdown voltages with published experimental [178] and simulated [177] data in DC-only field

All the parameters which are available in the published work are kept same in the simulations. The other parameters which are not mentioned in the published papers are assigned appropriate values. From the graphs of Fig. 4.7 and Fig. 4.8, it can be observed that the same trend is followed in our simulation results and in the results of other published works.

To further enhance the confidence level the data analysis was performed and the correlation coefficients were calculated. The correlation coefficients for experimental and other simulated results in Fig. 4.7 are calculated to be 0.957 and 0.9447 respectively. Similarly, the correlation coefficients of our data and the experimental and other simulated data plotted in Fig. 4.8 are 0.9827 and 0.9677 respectively. All of these values are close to '1' which shows the good matching of our data with the other experimental and simulated results.

In benchmarking, the results are compared with the published data and also validated with the theoretical calculations. Our simulated results show good agreement with the calculated and published results. This proves that enough understanding of the simulator, which is based on standard PIC-MCC codes, has been achieved. Moreover, it provides a detailed understanding about the electron densities and determination of gas breakdown voltages.

### **4.3 Effect of Device Structure on Gas Breakdown Behavior**

After gaining adequate understanding of the standard PIC-MCC codes, the simulations are carried out to investigate the effect of device structure on the gas breakdown behavior. These simulations are run by using the packages XPDP1 and XPDC1, which represent two types of devices, i.e. planar and cylindrical respectively. As already described in section 3.3, all the parameters are kept same in both the cases. The breakdown voltages are determined by varying the argon gas pressure from 0.1 Torr to 4.5 Torr with the gap spacing of 2.3 cm. The results are shown in Fig. 4.9.

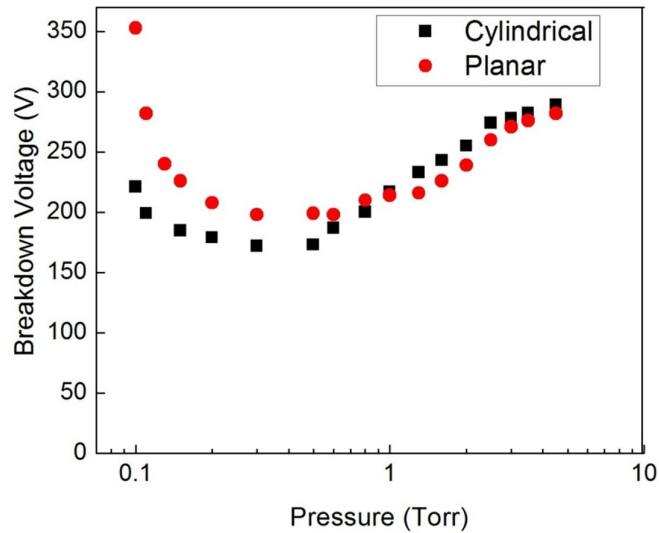


Fig. 4.9 Breakdown voltages as a function of gas pressure in two different device structures

In this graph, the breakdown voltages are following the typical U-shaped Paschen's curves with both the planar and cylindrical electrode structures. The minimum breakdown voltage is observed at 0.3 Torr of gas pressure. The breakdown voltages are increasing on both sides, i.e. right hand side and left hand side, from this minimum breakdown point. It can be observed from the graph that both the breakdown voltage curves in a pressure range greater than 0.3 Torr are in close agreement with each other. However, the breakdown voltage curves in a pressure range less than 0.3 Torr are not matching with each other. The breakdown voltages in the case of cylindrical electrodes are lower as compared to the breakdown voltages of planar electrode. To state the reason for this behavior of the graph, we recall the description provided in section 2.1.2.2. At slightly higher gas pressures the breakdown is initiated and developed by the gas and self-sustained by the electrode. But in a low gas pressure range, the breakdown is initiated, developed and self-sustained by the electrode. In the later case, the gas pressure is low which causes the decrease in the collision probability of the gas particles and hence, reduce the role of the gas and increase the role of electrode, in the breakdown mechanism. The same situation is occurring in these simulation results. The breakdown voltages at slightly

higher gas pressures, i.e. greater than 0.3 Torr, are in close agreement with each other. That means the argon gas, which is the same in both the electrode structures, is taking part in breakdowns and electrodes are playing no prominent role in the gas breakdowns. However, in the case of very low gas pressures, i.e. less than 0.3 Torr, the gas pressure is very low and breakdowns are occurring due to the processes which are taking place due to the electrodes. The electrode structures are different in both the cases, i.e. planar and cylindrical. That is why, the breakdown voltage curves are not matching in a pressure range less than 0.3 Torr. The cylindrical electrode structure has less breakdown voltages than the planar electrode structure in a range of gas pressure less than 0.3 Torr. Hence, the device structure has prominent effects on the gas breakdown voltage, especially in the low gas pressure range.

#### 4.4 Effect of Gas Species on Breakdown Behavior

After understanding the effects of device structure on the gas breakdown, some other simulations were run to investigate the effects of different gases on the breakdown behavior in the same device structure. The planar device is used in this case along with two gases i.e. argon and helium. The breakdown voltages of the two gases are shown in Fig. 4.10.

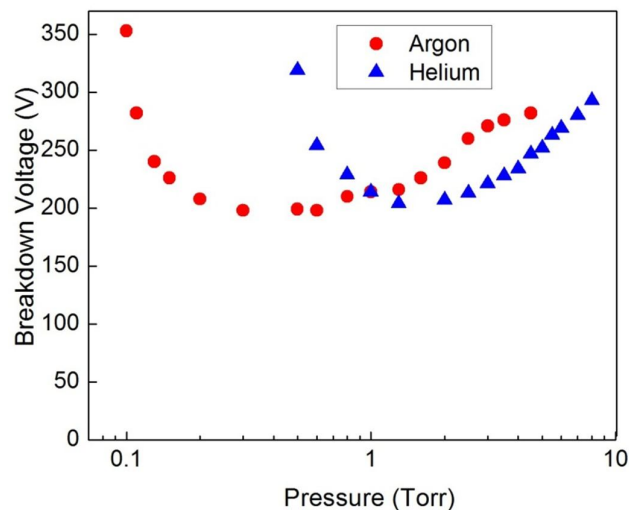


Fig. 4.10 Breakdown voltages of argon and helium in planar electrodes

It is observed from the Paschen's curves in Fig. 4.10 that the breakdown voltages of argon are in a pressure range of 0.1 Torr to 4.5 Torr. However, the breakdown voltages of helium are in a pressure range of 0.5 Torr to 8.0 Torr. In the simulations, the helium gas was not giving breakdown below 0.5 Torr of pressure. To verify this, Eq. (2.14) is used to calculate the minimum pressure limit for breakdown in helium gas. It is observed from the graph that the minimum breakdown voltage for helium is at 1.3 Torr of pressure. Putting this value of pressure and  $e = 2.72$  in Eq. (2.14), gives the minimum limit of the pressure for the gas breakdown to be 0.48 Torr. This value is in close agreement with the value observed from the simulations i.e. 0.5 Torr. Similarly, the minimum breakdown voltage for argon is at pressure of 0.3 Torr. Putting this value in Eq. (2.14) gives the minimum limit of pressure for the argon gas breakdown to be 0.11 Torr. This calculated value of minimum pressure limit for breakdown in argon is also in close agreement with the value observed from the simulations i.e. 0.1 Torr.

The reason for helium gas not giving breakdown below 0.5 Torr of pressure is its light weight. Helium is one order of magnitude lighter than the argon. Due to this reason the collision energy becomes low and the ionization rate decreases. At very low pressures, even non-local effects are not sufficient enough to initiate breakdown in the gas due to very light weight of the helium atom and less pressure. Hence, it was found that the minimum limit for the breakdown is different for two different gases and does not depend on the structure of the device.

#### **4.5 Breakdown Voltages in Micrometer Gaps**

So far, the simulations were carried out in the centimeter range of gap spacing. Those simulations were run to understand the functionality of the standard codes and to investigate the impact of different parameters on gas breakdown. In real gas sensor, the gap spacing is usually in micrometer range. The reduction of gap spacing from centimeter range to micrometer range affects the breakdown mechanism. Many input parameters need adjustment accordingly, as already described in chapter 3. Before testing the new model, a platform is required to compare the improved results of new model with standard model results. To achieve this goal, this simulation setup was

prepared using XPDP1 package without carbon nanotube field emission effects to determine the breakdown voltages in micrometer gap spacing.

In this setup, the planar electrode device of XPDP1 package was scaled down in the micrometer range. Argon gas was used with a pressure range from 300 Torr to 3800 Torr and gap spacing of 10  $\mu\text{m}$  in all the simulations. The details of the simulation parameters are provided in chapter 4. The results of the simulation setup in a wide range of gas pressure are provided in Fig. 4.11.

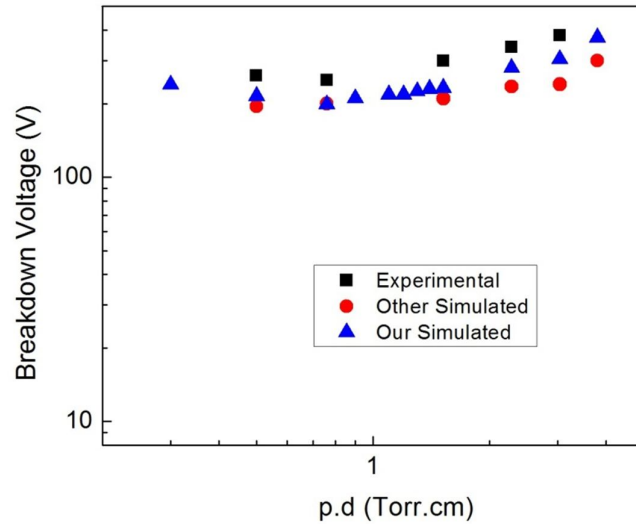


Fig. 4.11 Breakdown voltages in 10  $\mu\text{m}$  gap without carbon nanotube field emission model. The results are compared with published experimental [179] and simulated [177] data

In the graphs of Fig. 4.11, the breakdown voltages are plotted as a function of the product of gas pressure (Torr) and gap spacing (cm). The gap spacing of 10  $\mu\text{m}$ , which is equal to 0.001 cm, is kept constant in all the cases. However, the gas pressure was varied from 300 Torr to 3800 Torr. The breakdown voltages are decreasing with the decrease in the gas pressure. As the gas pressure is very high, the full U-shaped Paschen's curve is not apparent in the graph. The data points show the right hand side branch of the Paschen's curve from the minimum breakdown point. The breakdown voltages are compared with the published experimental [179] and

simulated [177] data. The high gas pressure range is selected according to the published data, so that the results can be easily comparable. The comparatively low gas pressure range in few hundred of Torr is selected to compare the results with the enhanced model results later. Our results show the same trend as observed in the published results. The correlation coefficients were calculated which are 0.9894 and 0.9708 for the comparison of our data with experimental and other simulated data respectively.

Once the results without carbon nanotube field emission effects are validated in micrometer gap spacing, this provides a platform to compare these results with enhanced model results in which the carbon nanotube field emission effects are included.

#### **4.6 Effect of CNT Field Emission on Gas Breakdown Behavior**

Now, moving towards the very interesting part of this thesis, i.e. results from the enhanced model. The results discussed in this section are taken from the simulations using Module 1 (CNT field emission module) along with Module 3 (position and velocity assignment module). The results from the Module 2 along with Module 3 will be discussed in section 4.7. The simulations are run in micrometer gap spacing and most of the parameters are selected according to the behaviour of real ionization gas sensor as described in chapter 3. The simulations of the breakdown behaviour including the carbon nanotube field emission effects in ionization gas sensor become possible for the first time with the help of this enhanced model.

To investigate the effects of carbon nanotube field emission on the gas breakdown, the breakdown phenomenon is studied in detail. As already described in chapter 2, the gas breakdown is initiated by a number of processes related to the movement of electrons and ions. The details of these processes are very difficult to examine in the experiments due to equipment limitation. With the help of our model, we have the opportunity to capture the number of electrons and ions along with their increasing and decreasing nature between the electrodes in short time intervals. As most of the simulations were run for 0.05 ps, this small time step was helpful to study

the details of the breakdown processes. The number of electrons and ions with respect to time without-CNT and with-CNT field emission effects is shown in Fig. 4.12 and Fig. 4.13.

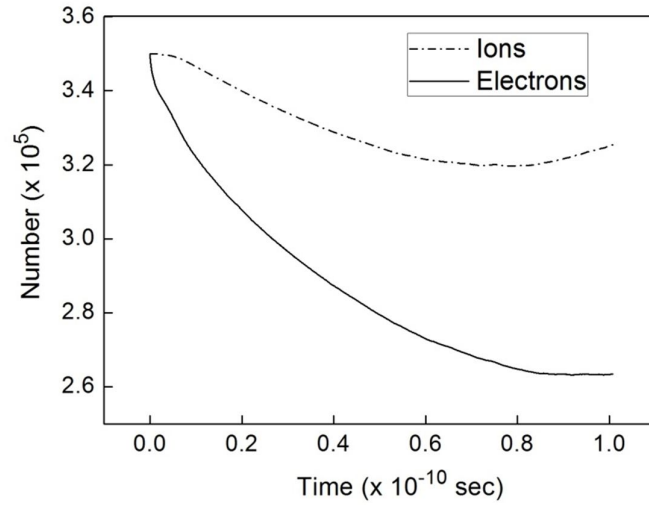


Fig. 4.12 Number of charged particles during simulation as a function of time in device without-CNT

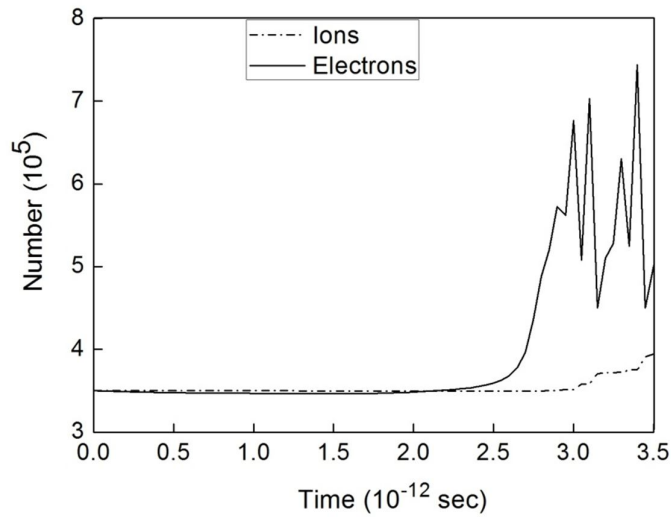


Fig. 4.13 Number of charged particles during simulation as a function of time in device with-CNT

These graphs of Fig. 4.12 and Fig. 4.13 are plotted with the data extracted from the simulation tool during the simulations. It is mentioned in chapter 3 that the initial number of computer particles in these simulations is  $3.5 \times 10^5$ . These number of computer particles can be seen in the graphs at time  $t = 0$ . When the simulation started, a different phenomenon is observed in both cases. In the case of device without-CNT (Fig. 4.12), the number of electrons and ions start decreasing. The number is determined by the creation of charged particles via ionization and their losses via collisional processes and diffusion to the walls. The decreasing nature of the graphs shows that the rate of creation of charged particles is less than the rate of loss of these particles. It means, initially most of the particles are lost. Even if the applied potential is continuously increasing, the rate of ionization is not enough to compensate the lost particles. Another observation is that the decreasing rate of the graphs of electrons and ions is different. The rate of loss of electrons is high as compared to the rate of loss of ions. This is due to the light weight of electrons which is few orders of magnitude less as compared to the ions. Electrons are more mobile than ions which increase their collision probability and also the diffusion rate.

As already mentioned the breakdown is determined by the balance between creation of charged particles and their loss until the field is uniform and supplied for a long period of time which is enough to create several generations of electrons. Hence, no breakdown is initiated until the rate of the creation of charged particles is less than the rate of loss. When the sufficient number of electrons is created and the rate of creation and loss of charged particles is balanced, that point is the threshold of the breakdown. Once the breakdown is initiated and the potential is still increasing, it helps the breakdown to fully develop and then to sustain itself. But the development of the breakdown and its self-sustaining nature does not depend only on the applied potential. There are number of factors involved e.g. gas pressure, electrode spacing, type and structure of the electrode etc.

The ionization collisions between the electrodes in without-CNT device are shown in Fig. 4.14.

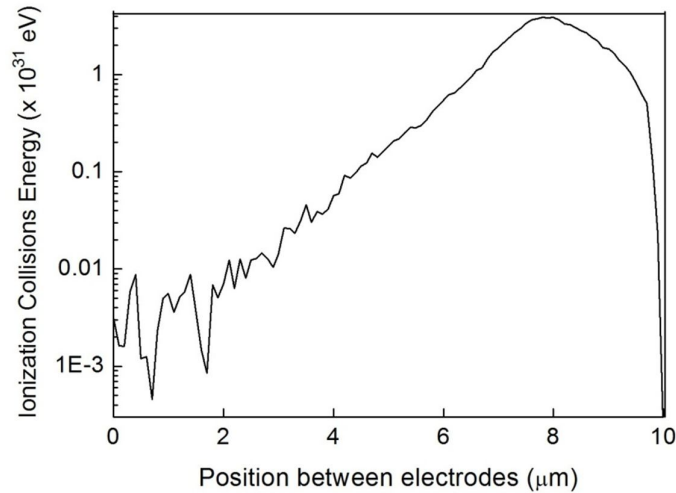


Fig. 4.14 Ionization collisions between the electrodes in without-CNT device

In Fig. 4.14, the y-axis shows the ionization collision energy and x-axis shows the gap spacing between the electrodes, which is 10 μm. The left hand side electrode at the gap spacing 0 is anode. However, the right hand side electrode where the gap spacing is 10 μm is the cathode. The maximum ionization collision energy in this case is  $3.9 \times 10^{31}$  eV. The argon gas which is non-attaching in nature results in positive ionization. Therefore, most of the ions are attracted towards the cathode and large number of ionization collisions is observed near the cathode.

The density of the charged particles between the electrodes in without-CNT device is shown in Fig. 4.15. In these graphs, the electron density is low compared to the ion density near the electrodes. However, it is almost the same near the center of the simulation space. The less electron density near the electrodes shows lack of secondary electrons, which are suppose to be emitted from the electrodes. But, near the center of the simulation space, more ionization collisions are taking place due to which an ion-electron pair is created. That is why, the electron and ion density is almost the same near the center of the electrodes. This statement can also be supported with the help of Fig. 4.18 in which ionization collisions are shown between the electrodes. These ionization collisions are very high near the center and low near the electrodes, keeping the electron density low near the electrodes. Also, the electron

density near the cathode ( $X=10\mu\text{m}$ ) is much lower than the electron density near the anode ( $X=0$ ). There are two reasons: (i) lack of secondary electron emission from the cathode (ii) the primary electrons created near the center of the space as a result of ionization are attracted towards the anode. Therefore, the electron density is high near the anode as compared to the cathode.

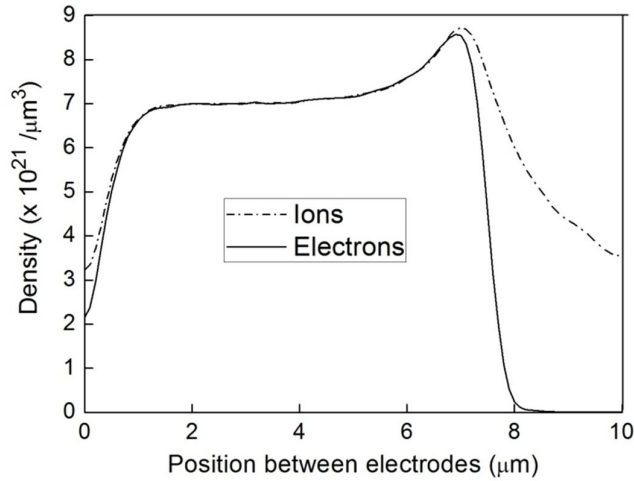


Fig. 4.15 Density of charged particles between the electrodes in without-CNT device

The graphs of Fig. 4.13 are plotted with the data taken from the simulations of the enhanced model in which the carbon nanotube field emission effects are present. In these graphs, the increasing and decreasing nature of the charged particles is quite different from the graphs of Fig. 4.12. The simulation started with the same number of initial computer particles, i.e.  $3.5 \times 10^5$  at  $t = 0$ . Initially, the number of charged particles decreases because large number of particles is lost in the boundaries. Secondly, the rate of carbon nanotube field emission is low because the applied potential is less than the turn-on field. Once the potential is increased and field becomes non-uniform near the tips of the carbon nanotubes, the rate of electron field emission increases. It is clear from the graphs of Fig. 4.13 that at some particular time the electron population increases vigorously. This is the time when the potential becomes greater than the turn-on field and the electron emission rate is increased. In the graph, the number of electrons greater than the number of ions shows the emission of electrons from the cathode due to carbon nanotubes. This large number of electrons

is contributing to increase the ionization rate and the creation of electron avalanche. This electron avalanche is created at a very low potential (around one order of magnitude low) as compared to the case of without carbon nanotube field emission. Once the breakdown is initiated, it is very easy to develop a breakdown and self-sustain it with the help of these emitted electrons.

The ionization collisions between the electrodes in with-CNT device are shown in Fig. 4.16. In this case, the ionization collisions are very intense due to the large number of secondary electron emission. As, the secondary electrons were emitted from the cathode due to carbon nanotubes, the large number of ionization collisions are shifted towards the cathode. The rate of ionization increases throughout the gap spacing from 0 to 10  $\mu\text{m}$  but at the cathode, the number of ionizations is maximum. The formation of the graph is also changed compared to the without-CNT case. In without-CNT case, the maximum ionization collisions are near the cathode but in with-CNT case the high intensity ionizations are occurring at the cathode showing the vigorous electron emission. The ionization energy reaches up to  $3.81 \times 10^{34}$  eV which is three orders of magnitude greater than the ionization energy of without-CNT device.

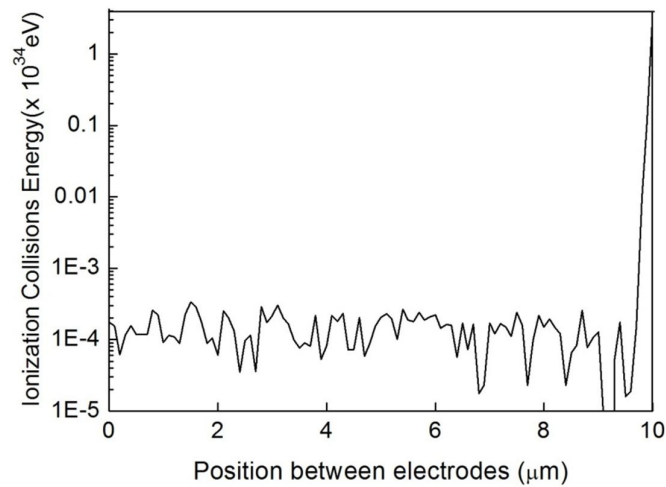


Fig. 4.16 Ionization collisions between the electrodes in with-CNT device

The density of the charged particles from the simulations with carbon nanotube field emission model is shown in Fig. 4.17. It is clear from the graph that the electron density near the cathode is much greater than ion density due to the secondary electron emission from the cathode. Due to this secondary electron emission the ionization collisions are also increased at the cathode as already shown in Fig. 4.16. The electron and ion density at the anode is around two orders of magnitude lower because the secondary electrons are emitting from cathode and more ionization is also taking place at the cathode. However, electrons created or emitted at the cathode are attracted towards the anode. This is the reason that electron density near the anode is still of the order of  $10^{21}$ .

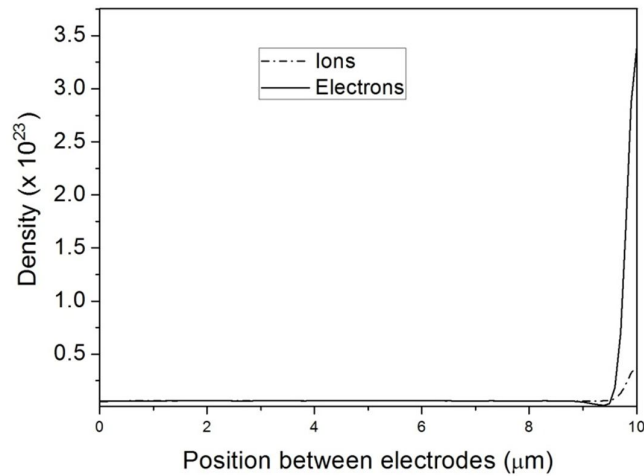


Fig. 4.17 Density of charged particles between the electrodes in with-CNT device

The plotted graphs of Fig. 4.12 to Fig. 4.17 from the simulations show that the breakdown phenomenon with and without carbon nanotube field emission is changed. In the case of without field emission effects, the breakdown was determined by the balance between the creation and loss of charged particles. However, in the case of carbon nanotube field emission, the breakdown is determined by the completion of the creation of electron avalanche. Hence, the gas breakdown phenomenon and the determination criteria in both the cases are different.

#### 4.6.1 Improvement in Breakdown Voltages due to CNTs

In this simulation setup, the argon gas is used between the electrodes. The breakdown voltages are determined by varying the gas pressure from 300 Torr to 1400 Torr and initially, keeping the gap spacing constant at 10  $\mu\text{m}$ . The results of these simulations are shown in Fig. 4.18.

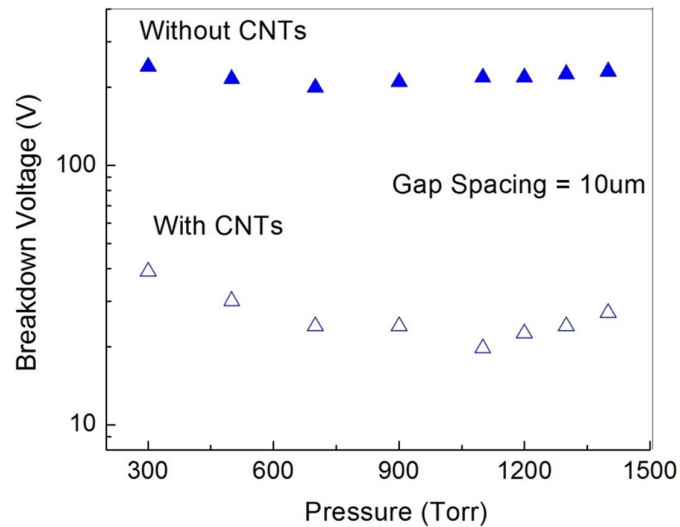


Fig. 4.18 Comparison of breakdown voltages determined from simulations of standard and enhanced model in 10  $\mu\text{m}$  gap spacing

To examine the effects of the carbon nanotube field emission on the breakdown voltages, the enhanced model results are compared with the standard model results which were shown in Fig. 4.11. In the results of standard model the breakdown voltages were in the range of 200 V to 240 V in the gas pressure range of 300 Torr to 1400 Torr. However, the results of the enhanced model in the same gas pressure range show the breakdown voltages in the range of 20 V to 30 V. Hence, a remarkable decrease by around one order of magnitude in the breakdown voltages is observed when enhanced model is used in the simulations. This decrease in the breakdown voltages is due to the effects of carbon nanotube field emission which are incorporated in the enhanced model. The local and non-local effects, both are contributing to achieve the gas breakdown at a lower voltage. The secondary electron

emission from the cathode due to carbon nanotubes is playing a major role to speed up the ionization process. The electric field becomes non-uniform and a high electric field region is created near the cathode. The particles in this high electric field region gain large energy which increases the collision probability. The increase in collision probability increases the creation of ion-electron pairs which are accelerated by the high electric field and produce more secondary electrons. Hence, these processes create a positive feedback, which leads to the gas breakdown at a lower voltage.

In experiments the researcher cannot enjoy the full freedom of playing with various parameters simultaneously. To take a good advantage of the simulation setup, we have also changed the gap spacing between the electrodes along with the gas pressure. For different gap spacing from 2 $\mu\text{m}$  to 12 $\mu\text{m}$ , the breakdown voltages were determined by changing the gas pressure in a range of 300 Torr to 1400 Torr. The simulation results of with-CNT and without-CNT field emission effects in a gap spacing of 12  $\mu\text{m}$  are shown in Fig. 4.19.

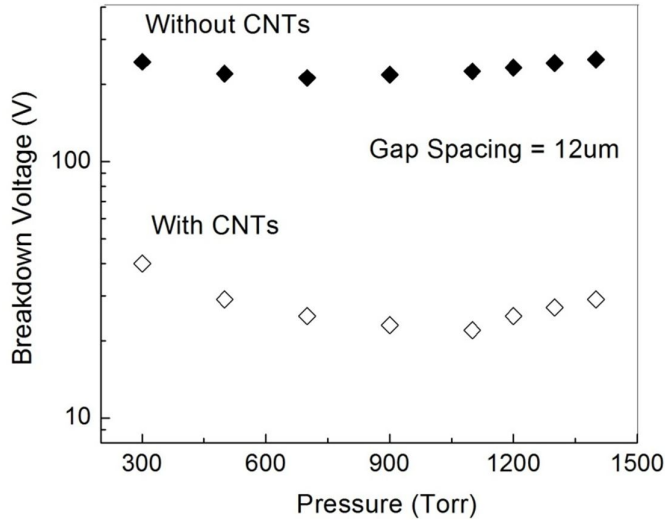


Fig. 4.19 Comparison of breakdown voltages determined from simulations of standard and enhanced model in 12  $\mu\text{m}$  gap spacing

In the graph of Fig. 4.19, the overall breakdown voltages are slightly shifted upwards along y-axis. The breakdown voltages without carbon nanotube field emission effects

are in the range of 212V to 250 V. In the case of 10  $\mu\text{m}$  gap spacing, the lowest breakdown voltage observed was 199 V at a pressure of 700 Torr. However, in the case of 12  $\mu\text{m}$  gap spacing the lowest breakdown voltage point has been shifted to 212 V at the same gas pressure. Hence, an increase in the breakdown voltage by 13 V is observed by increasing the gap spacing by 2  $\mu\text{m}$ . The breakdown voltages with carbon nanotube field emission effects are also shown in Fig. 4.19. Most of the breakdown voltages are in the range of 22 V to 30 V. The lowest breakdown voltage is increased by around 2 V as compared to the similar graph of Fig. 4.18. The highest breakdown point observed in the graph is 40 V at 300 Torr of gas pressure. This data point is almost at the same position in both the 10  $\mu\text{m}$  and 12  $\mu\text{m}$  cases. The reason is the low gas pressure along with the very less gap spacing. At this low pressure, the secondary electrons are needed to develop a breakdown in a gas. The carbon nanotube field emission is playing a major role in providing these secondary electrons which develops and sustains a breakdown in a low pressure gas. Overall view of the Fig. 4.19 shows the same one order of magnitude decrease in the breakdown voltages in the case of carbon nanotube field emission model.

After observing the effects of carbon nanotube field emission on the breakdown voltages at 10  $\mu\text{m}$  and 12  $\mu\text{m}$  gap spacing, the simulations are run by reducing the gap spacing to 8  $\mu\text{m}$ . The graph is shown in Fig. 4.20.

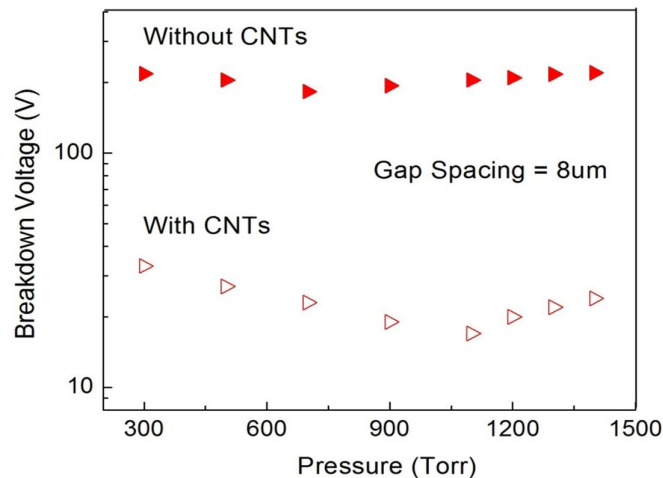


Fig. 4.20 Comparison of breakdown voltages determined from simulations of standard and enhanced model in 8  $\mu\text{m}$  gap spacing

As the gap spacing is reduced to 8  $\mu\text{m}$ , the breakdown voltages are shifted downwards. This is a typical trend which was expected, based on the theoretical knowledge, by reducing the gap spacing between the electrodes. The breakdown voltages are in the range of 183 V to 220 V in the without-CNT device and 19 V to 33 V in the with-CNT device. These breakdown voltages are lower than the breakdown voltages observed in the previous two cases i.e. 10  $\mu\text{m}$  and 12  $\mu\text{m}$ . The lowest breakdown voltages in without-CNT device in the previous cases were 199 V and 212 V respectively. However, in this case it is reduced to 183 V. Hence, a reduction of 16 V is observed from the lowest breakdown voltage of the 10  $\mu\text{m}$  case. The breakdown voltages in the with-CNT device are also reduced in 8  $\mu\text{m}$  case. The highest data point which is at 300 Torr of gas pressure is reduced to 33 V as compared to the 40 V in previous two cases. Except this data point, all other breakdown voltages are below 27 V in the graph of Fig. 4.20. The lowest breakdown occurs at 17 V, which is 3 V and 5 V lower than the lowest breakdown points of 10  $\mu\text{m}$  and 12  $\mu\text{m}$  cases respectively. The comparison of graphs of without carbon nanotube field emission model and with carbon nanotube field emission model shows the same trend in lowering down the breakdown voltages by around one order of magnitude.

To further check the repeatability of the enhanced model results, the gap spacing was reduced to 6  $\mu\text{m}$ , 4  $\mu\text{m}$  and 2  $\mu\text{m}$  with the same simulation setup. The graphs are shown in Fig. 4.21, Fig. 4.22 and Fig. 4.23 respectively.

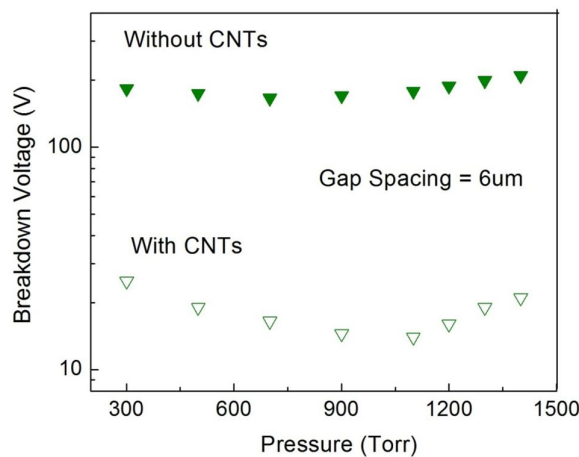


Fig. 4.21 Comparison of breakdown voltages determined from simulations of standard and enhanced model in 6  $\mu\text{m}$  gap spacing

In the gap spacing of 6  $\mu\text{m}$ , the breakdown voltage range without carbon nanotube field emission effects was reduced to 166 V – 210 V. Most of the breakdown voltages were below 200 V. The lowest breakdown voltage, i.e. 166 V, is 17 V lower than that at the equivalent point in 8  $\mu\text{m}$  case. However, in the case of simulations using carbon nanotube field emission model, the breakdown range is from 14 V to 25 V. The lowest breakdown point, i.e. 14 V, is 3 V lower than the equivalent point in 8  $\mu\text{m}$  gap spacing.

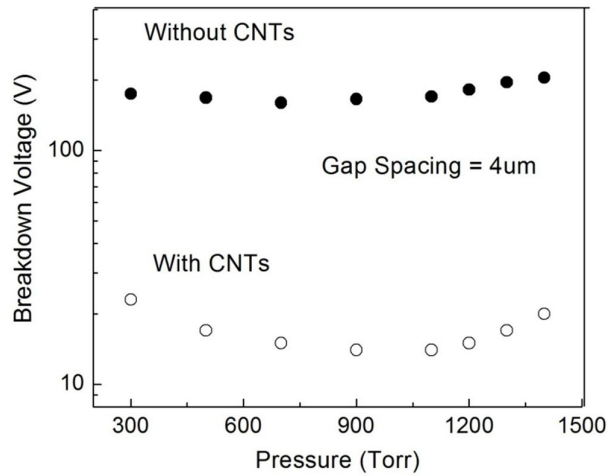


Fig. 4.22 Comparison of breakdown voltages determined from simulations of standard and enhanced model in 4  $\mu\text{m}$  gap spacing

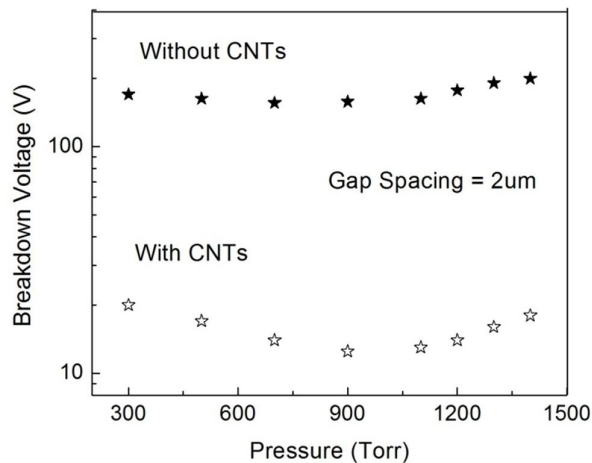


Fig. 4.23 Comparison of breakdown voltages determined from simulations of standard and enhanced model in 2  $\mu\text{m}$  gap spacing

The same trend is observed in the cases of Fig. 4.22 and Fig. 4.23. This trend shows almost the same decreasing factor in the breakdown voltages as was observed in the previous cases when the gap spacing was reduced from 12  $\mu\text{m}$  to 6  $\mu\text{m}$ . The comparison of breakdown voltages of with and without carbon nanotube field emission model also gives the same decreasing factor by around one order of magnitude.

We conclude this discussion by two important points: (i) the repeatability of the results, i.e. around one order of magnitude decrease in the breakdown voltages with carbon nanotube field emission effects in all gap spacing is observed and (ii) the same decreasing factor in the breakdown voltages is achieved by changing various gap spacing accordingly. This shows that the enhanced model which incorporates the effects of carbon nanotube field emission is working consistently with the standard model.

To check the reliability of the results taken from the simulations of the enhanced model, the available published data is considered. In this published work, Z. Hou et al. [90] developed the carbon nanotube based ionization gas sensor. They have performed experiments to record the breakdown voltages using air as a medium between the two electrodes in with-CNT and without-CNT devices. Their data is available for the breakdown voltages in air and we have tested our model using argon gas. We can understand this is not a one to one comparison. We are not comparing the breakdown voltages of air with argon gas. The only thing we want to take from the data of Z. Hou et al. [90] is the decreasing factor in the breakdown voltages of the with-CNT and without-CNT devices. The breakdown voltages in air at various gap spacing in with-CNT and without-CNT devices taken from [90] are shown in Table 4.1.

Table 4.1 Breakdown voltages in air at various gap spacing  
in with-CNT and without-CNT devices [90]

Gap Spacing ( $\mu\text{m}$ )	Breakdown Voltage (V)	
	Without-CNT	With-CNT
6	$359 \pm 20$	$14 \pm 0.3$
8	$392 \pm 20$	$20 \pm 0.3$
10	$413 \pm 20$	$25 \pm 0.3$
12	$427 \pm 20$	$37 \pm 0.3$

From Table 4.1, it is seen that the breakdown voltages in without-CNT device are in the range of 359 V to 427 V. However, the breakdown voltages in with-CNT device are in the range of 14 V to 37 V. This shows the breakdown voltages are lowered by around one order of magnitude in the case of with-CNT device. The same trend is observed in our model results. Hence, the comparison of the decreasing factor of breakdown voltages in with-CNT device, taken from the experimental published data, shows the same trend as observed in the results of our carbon nanotube field emission model.

#### 4.6.2 Improvement in Response Time due to CNTs

In general, the time taken by the gas breakdown without carbon nanotube field emission is usually in the range of  $10^{-6}$  to  $10^{-10}$  seconds depending on the nature of the breakdown. As, this time is very short so it is very difficult to capture it during experiments. But, using simulator, the breakdown time is captured easily. We have determined the breakdown time, by running simulations with and without carbon nanotube field emission model. As the ionization gas sensor detects the gas by the breakdown mechanism, this breakdown time is also called response time of the device.

To have a look at the response time of the without-CNT device, Fig. 4.12 is referred again. In Fig. 4.12 the time recorded is  $1.0075 \times 10^{-10}$  sec. which is the time at which the breakdown has initiated. The time after the breakdown occurred is again recorded and is shown in Fig. 4.24. In Fig. 4.24, the time recorded is  $1.063 \times 10^{-10}$  which is the time just after the breakdown has occurred. Hence, the response time of the without-CNT device is in the range of  $1 \times 10^{-10}$  seconds.

The number of charged particles as a function of time in with-CNT device is shown in Fig. 4.25. The simulations are run to record a breakdown time using carbon nanotube field emission model. In this case the response time is recorded just after the breakdown has occurred. At this stage the highly intense ionizations with great energy are taking place at the cathode, shown in Fig. 4.16. This increased ionizations and the secondary electron emission from the cathode creates avalanche and the number of electrons becomes greater than the number of ions. The recorded time just after the breakdown is  $3.3 \times 10^{-12}$  seconds. This shows that the breakdown occurred in the time range of around  $3 \times 10^{-12}$  seconds. This response time is two orders of magnitude faster than the response time of the device without carbon nanotube field emission.

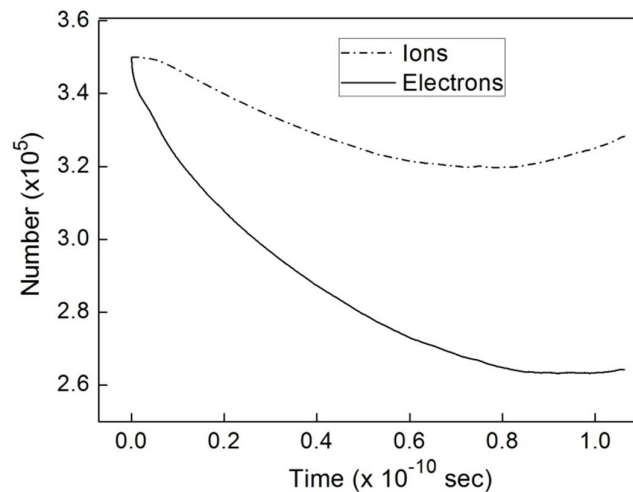


Fig. 4.24 Number of charged particles as a function of time in without-CNT device.

The time recorded just after the breakdown occurred

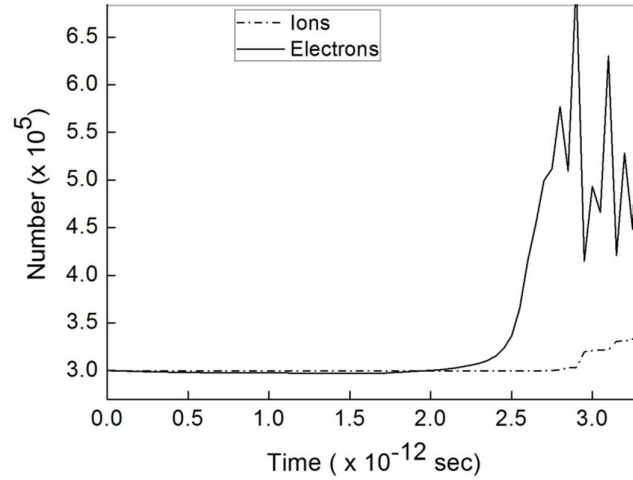


Fig. 4.25 Number of charged particles as a function of time in with-CNT device. The time recorded just after the breakdown occurred

The carbon nanotube field emissions change the breakdown phenomenon in the device. This change is due to the emission of large number of electrons from the cathode which create electron avalanche at much lower voltages. The large number of electrons emitted at much lower voltages reduces the time taken by the breakdown to occur.

#### 4.7 Effect of CNT Density and Aspect Ratio on Gas Breakdown Behavior

After discussing the effects of carbon nanotube field emission on the gas breakdown behavior, now the effects of carbon nanotube density and aspect ratio on the breakdown behavior is studied. The field emission behaviour of carbon nanotubes is affected by the density of the tubes, so the aspect ratio and density variation module is also included to make a new model more close to the reality. These effects are incorporated in the Module 2, which is already described in chapter 3.

This simulation setup is run to test the functionality of Module 2 along with Module 3. Most of the parameters are kept same as in the previous case but few new parameters are added and assigned proper values, as already mentioned in chapter 3.

According to these parameter values the density is calculated and the field emission is provided by the carbon nanotubes. As, the carbon nanotube density plays an important role in their field emission behavior, the calculation of carbon nanotube density in the model is very important. To validate the density calculation criteria described in the model, densities are calculated several times and compared with the published experimental data.

#### 4.7.1 Validation of CNT Density Calculation

Before discussing the simulation results, the CNT density calculation procedure applied in our new model is validated by the experimental published results. The density calculation criterion is given in section 3.5.2.2.1 and is not repeated here. Results of calculated density from our model and the experimental data of Teo et al. [137] are provided in Table 4.2 and Table 4.3.

Table 4.2 Comparison of CNT density of our model with experimental data. The intertube spacing to tube height ratio is zero

<b>Density variation parameters</b>	<b>Published Data [137]</b>	<b>Our Data</b>
CNT Diameter	50-100nm	100nm
CNT Height	5 $\mu$ m	5 $\mu$ m
Intertube spacing to height ratio	0	0
Density	10 <sup>9</sup> / cm <sup>2</sup>	10 <sup>10</sup> / cm <sup>2</sup>

In Table 4.2, the density of the carbon nanotubes is given with intertube spacing equal to zero. That means the nanotubes are very close to each other and the density of the nanotubes is very high. The height of the carbon nanotubes is 5  $\mu$ m which is

same as in the published data. The diameter of the carbon nanotubes is mentioned 50 nm – 100 nm in the published data, which is considered as 100 nm in this case. The density calculated by our model with these parameters is  $10^{10} / \text{cm}^2$ . The published data shows density of the carbon nanotubes around  $10^9 / \text{cm}^2$ . The one order of magnitude difference at such a large scale can be negligible without affecting the efficiency of the nanotubes. It is mentioned in many published papers that all the fabricated nanotubes do not work efficiently. Some nanotubes may damage during the fabrication or some work partially. So this difference in the nanotube density is considered very small which do not affect the functionality of the carbon nanotube array.

Table 4.3 Comparison of CNT density of our model with experimental data. The intertube spacing is two times the tube height

<b>Density variation parameters</b>	<b>Published Data [137]</b>	<b>Our Data</b>
CNT Diameter	55nm	55nm
CNT Height	5 $\mu$ m	5 $\mu$ m
Intertube spacing to height ratio	2	2
Density	$1 \times 10^6 / \text{cm}^2$	$0.99 \times 10^6 / \text{cm}^2$

In Table 4.3, the calculated value from our model and the experimental published value of the density of carbon nanotubes are given with an intertube spacing equal to two times the height of the nanotube. The carbon nanotubes with this intertube spacing are far apart from each other and are considered in the moderate density range. The diameter and height of the carbon nanotubes are 55 nm and 5  $\mu$ m respectively, and are same in both the cases. The density of the carbon nanotubes with these mentioned parameters is calculated to be  $0.99 \times 10^6 / \text{cm}^2$ . This calculated value

from our model is quite close to the experimentally examined value of the published data, which is  $1 \times 10^6 / \text{cm}^2$ .

With this comparison of calculated density with the published data, it is found that the density values are very close to each other. Hence, the assumptions which are considered in our model are acceptable, and the method which is applied in our model to calculate the density of carbon nanotubes is close to reality.

#### **4.7.2 Effect of CNT Density Variation on Breakdown Voltages**

Once, the density calculation criteria is validated, the simulation setup is prepared to test the functionality of Module 2 along with Module 3. The simulations were run to study the effects of carbon nanotube density and aspect ratio on the field emission behavior, which affects the gas breakdown behavior. All the simulations were run with a constant gap spacing of  $10 \mu\text{m}$  and varying the gas pressure. The density of the nanotubes is changed by changing the intertube spacing. The details of the parameter values are provided in chapter 3.

The graph of Fig. 4.26 shows the breakdown voltages as a function of gas pressure. The carbon nanotubes are highly dense with an intertube spacing equal to zero. In the case of high density, all the nanotubes are not contributing to the field emission due to electrostatic screening effects (already described in chapter 2). The actual emitting sites become low and the field emission is decreased. Still, in the case of high density, the breakdown voltages are lowered and are in the range of 13 V to 18 V.

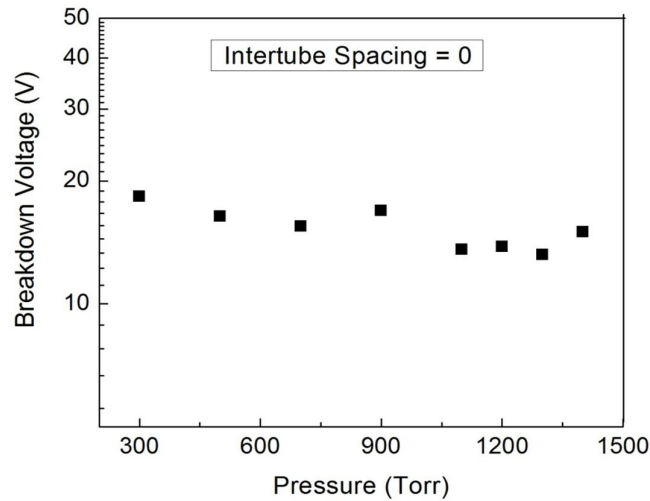


Fig. 4.26 Breakdown voltages as a function of gas pressure with zero intertube spacing

The electrostatic screening effects can be reduced if the nanotube density is lowered. The graph of Fig. 4.27 shows the breakdown voltages with intertube spacing equal to the height of the nanotube. In this case, the nanotubes are far apart from each other and the moderate density is observed as compared to the previous case. The much lowered breakdown voltages are observed which shows the sufficient number of nanotubes on the electrode and all the nanotubes are contributing to the field emission. The breakdown voltages are in the range of 8.5 V to 11 V which is very low as compared to the high density nanotubes. However, the same trend in the breakdown curves is observed in both the cases.

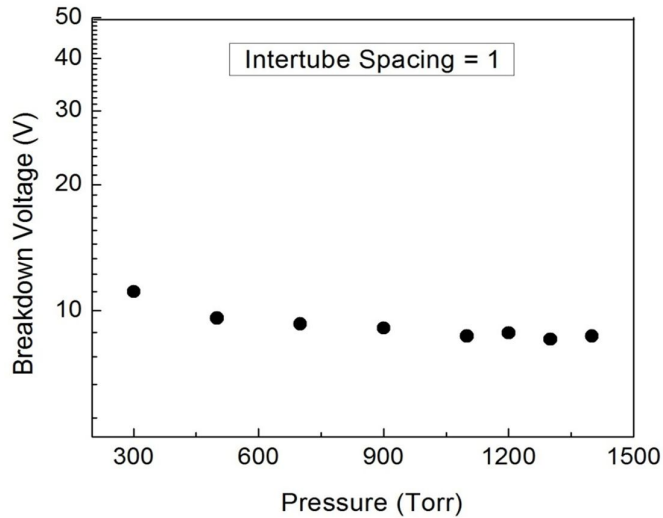


Fig. 4.27 Breakdown voltages as a function of gas pressure with intertube spacing equal to height of the nanotube

The graph of Fig. 4.28 shows the breakdown voltages with more sparse nanotubes in which the intertube spacing is increased to two times the height of the nanotube. The nanotube density is further lowered but still in the range of moderate density. The breakdown voltages are determined in the range of 10.5 V to 14 V. These breakdown voltages are low than the highly dense nanotubes where intertube spacing was zero, but high than the breakdown voltages when intertube spacing was equal to height of the nanotubes. The density of the nanotubes is still in the moderate density range but the number of nanotubes becomes low due to the high intertube spacing. In this case, the electrostatic screening effects are reduced to minimum and all the nanotubes are contributing to the field emission but breakdown voltages are increased due to low number of nanotubes.

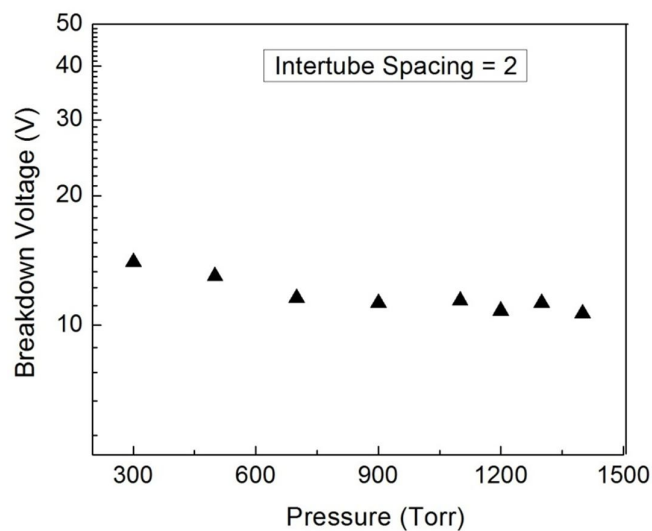


Fig. 4.28 Breakdown voltages as a function of gas pressure with intertube spacing equal to two times height of the nanotubes

The breakdown voltages with intertube spacing equal to three times the height of the nanotubes is shown in Fig. 4.29. It is clear from the graph that the breakdown voltages are further increased as compared to the case in which the intertube spacing is equal to two times the nanotube height. The breakdown voltages are in the range of 12 V to 17 V. But on the other hand, they are still low than the breakdown voltages in the case of highly dense nanotubes where the intertube spacing was zero. That means density of nanotubes is still considered in the moderate density range but it is on the lower side of this range.

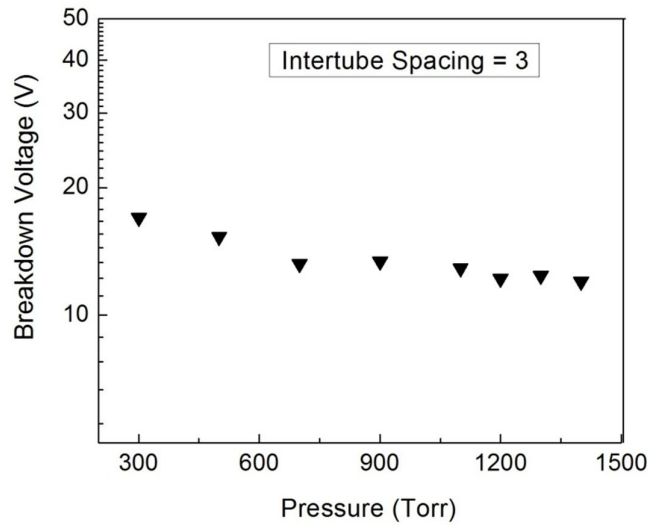


Fig. 4.29 Breakdown voltages as a function of gas pressure with intertube spacing equal to three times height of the nanotubes

To check the reliability of our model with further low densities, simulations were run with intertube spacing equal to four and five times the height of the nanotubes. The graph of breakdown voltages by keeping intertube spacing equal to four is shown in Fig. 4.30. In this case, the number of nanotubes is further decreased and the density becomes lower. The breakdown voltages are in the range of 15 V to 20 V which is high from the previous case and also from highly dense case. This shows that the density of the nanotubes is in the low density range when the intertube spacing is equal to four times height of the nanotubes. In low density range the field emission becomes very low due to very less number of nanotubes on the electrode.

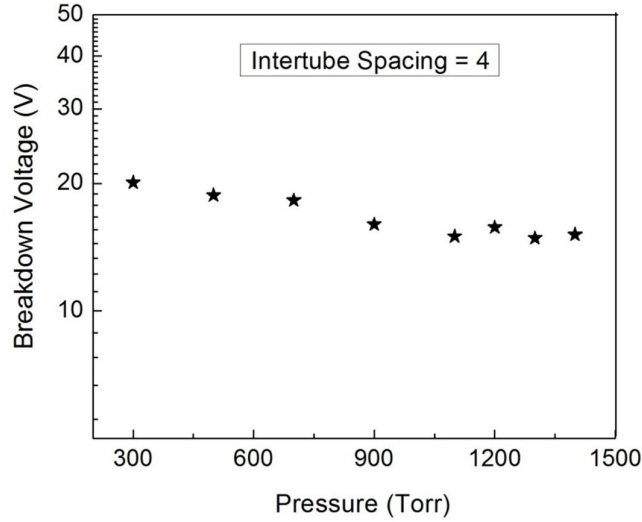


Fig. 4.30 Breakdown voltages as a function of gas pressure with intertube spacing equal to four times height of the nanotubes

The Fig. 4.31 shows the breakdown voltages with intertube spacing equal to five times height of the nanotubes. The range of the breakdown voltages is from 17 V to 22 V. These breakdown voltages are higher than all the density variation cases which are discussed so far. In this case, the number of nanotubes is further decreased, the field emission is reduced, and the breakdown voltages are further increased by around 10%.

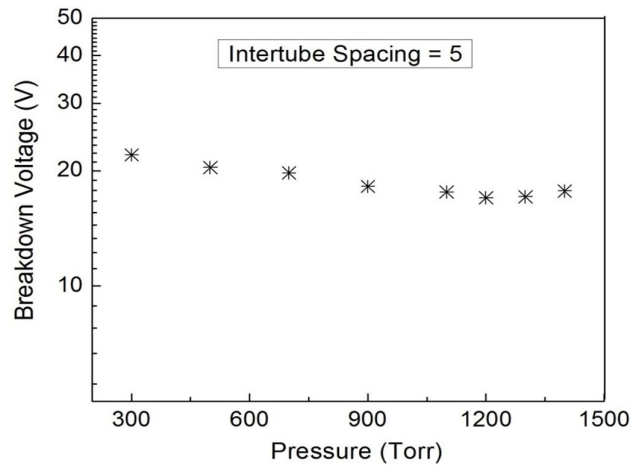


Fig. 4.31 Breakdown voltages as a function of gas pressure with intertube spacing equal to five times height of the nanotubes

To conclude this discussion, we can have a look at couple of more graphs in which the whole scenario is summarized. The graphs of Fig. 4.32 show the breakdown voltage curves at different intertube spacing along with the breakdown voltages of without-CNT device. From these graphs it can be concluded that the excellent field emission is observed from carbon nanotubes in all the density ranges. The great decrease of breakdown voltages which is observed in the comparison of with-CNT and without-CNT device is still there. Optimization of carbon nanotube density ranges to reduce electrostatic screening effects is just like the fine tuning of breakdown voltages to reduce further. But overall, the same trend is observed in all the cases. The ionization collisions, and number and the density of charged particles are almost the same in all these density ranges and similar to the cases discussed in the section 4.6.

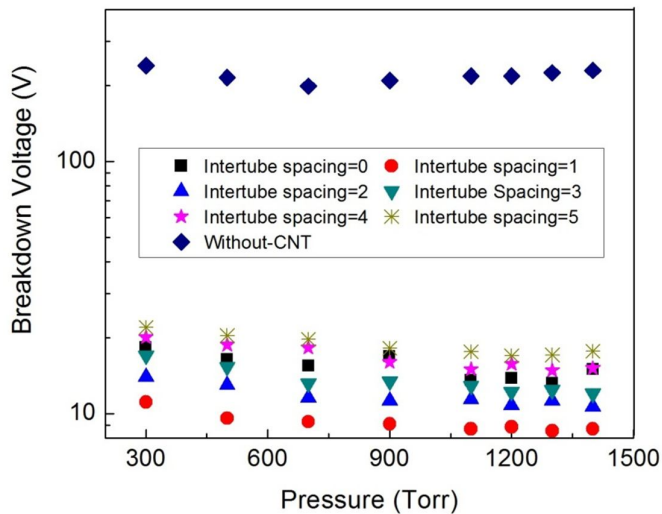


Fig. 4.32 Comparison of breakdown voltages with-CNT in different density range and without-CNT device

In Fig. 4.33, the breakdown voltages are shown as a function of intertube spacing to tube height ratio with a constant gas pressure of 1400 Torr and gap spacing of 10  $\mu\text{m}$ .

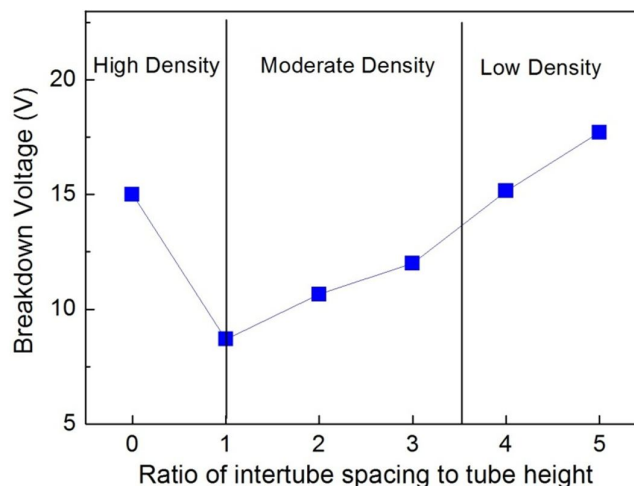


Fig. 4.33 Breakdown Voltages as a function of intertube spacing to tube height ratio at constant gas pressure of 1400 Torr

In this graph, the carbon nanotube density ranges are defined according to the trend observed in the breakdown voltages. The breakdown voltages are decreasing with decreasing the intertube spacing. The transition from low density range to high density range takes place when the intertube spacing to tube height ratio is equal to 3.5. The lowest breakdown voltage is observed when the intertube spacing is equal to the height of the nanotube. At this point, sufficient number of nanotubes is present on the electrode to produce large field emission and the space between the nanotubes is enough to reduce the electrostatic screening effects to minimum. Below this point, the transition from moderate density range to high density range takes place. The number of nanotubes becomes large but space between them is very small and electrostatic screening effects are produced. In this case, all the nanotubes are not contributing to the field emission hence, reducing the field emission and increasing the breakdown voltage.

#### 4.8 Results Validation with Field Enhancement Factor ( $\beta$ )

To further check the integrity of our codes and to validate the results provided by the simulations using our enhanced model, the field enhancement factor  $\beta$  is calculated and verified. The field enhancement factor is very important parameter to examine the field emission property of the nanomaterials. The detail overview of  $\beta$  is provided in chapter 2 and is not repeated here. The graph of electric field between the electrodes from the simulations of our enhanced model is shown in Fig. 4.34.

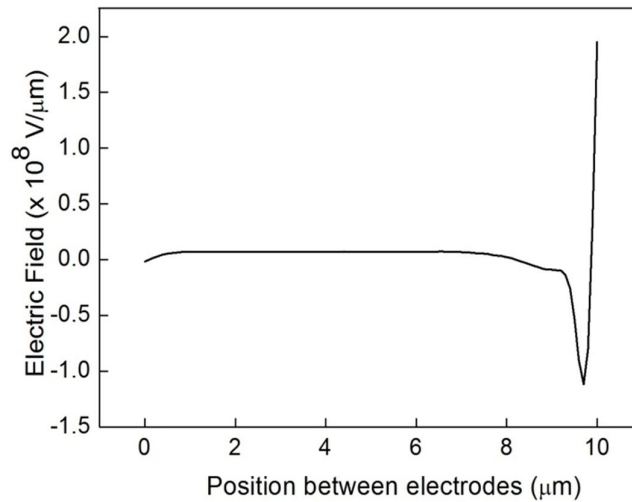


Fig. 4.34 Electric field between the electrodes in with-CNT device. The non-uniform enhanced electric field is observed near the cathode

In Fig. 4.34, the electric field is captured near the occurrence of breakdown in the device. The electric field is very high near the cathode due to the presence of the field emission effects. Due to this high electric field, ionization collisions near the cathode also increases as already shown in Fig. 4.16. This very high electric field is observed at the applied potential of 14.7 V as shown in Fig. 4.35.

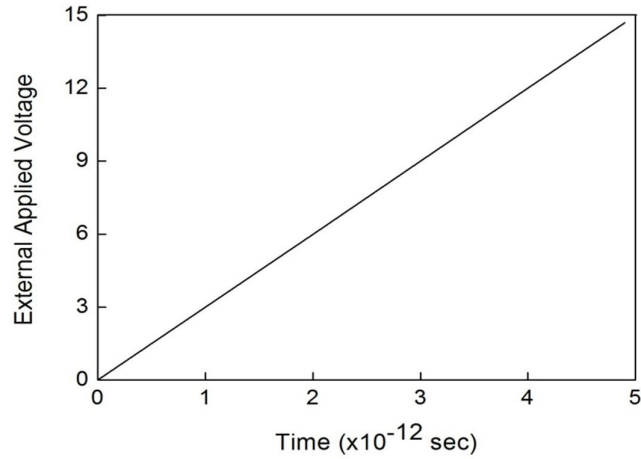


Fig. 4.35 The potential applied to the with-CNT device at which the high electric field of Fig. 4.34 is observed

By extracting data from the graphs and using Eq. (2.15), we can calculate the field enhancement factor  $\beta$ , provided by our enhanced model. The applied field  $E_{app}$  can be calculated using Eq. (2.3), putting  $V = 14.7$  and  $d = 10\mu m$ . Using these values, the applied field is calculated to be  $1.47 \times 10^6$  V/ $\mu m$ . The effective field  $E_{eff}$  which is enhanced by the field emission effects of carbon nanotubes observed near the cathode in Fig. 4.34 is  $2 \times 10^8$  V/ $\mu m$ . Using these values of  $E_{app}$  and  $E_{eff}$  in Eq. (2.15) to get the  $\beta$  of our enhanced model, which is calculated to be 136.

To verify  $\beta$  from our enhanced model, Eq. (2.16) is used. As already described in chapter 2, this equation is based on the well established *hemisphere on post* model [146]. Using values of height of nanotube as  $h = 5\mu m$  and radius of the nanotube as  $r = 27.5 nm$  in Eq. (2.16), gives the value of  $\beta$  equal to 131. The close agreement with less than 5% error between  $\beta$  calculated from a well established model and  $\beta$  calculated from our model validates our field emission model of carbon nanotubes.

Furthermore, the value of  $\beta$  of our model is compared with the  $\beta$  values of other published works. Sadegian et al. [93], based on their work published in 2007, calculated  $\beta$  of gold nanowire based ionization gas sensor to be 37.9. They have claimed that their value of  $\beta$  is better by almost eight times than the  $\beta$  of carbon

nanotube based ionization gas sensor. This carbon nanotube based ionization gas sensor was reported by Zhang et al. [180] in their work published in 2006. The values of  $\beta$  in their carbon nanotube based ionization gas sensor vary between 3 ~ 5.

From the value of  $\beta$  of our enhanced model, we can state that using carbon nanotubes in ionization gas sensor a better field enhancement can be achieved. Our value of  $\beta$  is almost 3.6 times and 28 times better than the  $\beta$  values of gold nanowire based ionization gas sensor and other carbon nanotube based ionization gas sensor, respectively. The reason for this better field enhancement factor is the optimization of various parameters which is achieved with the help of our model. Among these, the most important parameters are density and aspect ratio of the carbon nanotubes, and gap spacing between the electrodes. In addition, the accuracy of the field emission provided by our enhanced model according to the selected value of density and aspect ratio also plays important role in defining the value of  $\beta$ .

#### **4.9 Improvement in Performance of Ionization Gas Sensor**

After discussing and validating the results obtained from the simulations using enhanced PIC-MCC model, the main findings from the results are extracted and listed below.

- Breakdown voltages are dependent on the applied field; lowered by 2 to 3 times if the combined RF and DC field is applied
- Breakdown voltages are dependent on the device structure; lowered by few volts if the cylindrical electrodes are used instead of planar electrodes
- Breakdown voltages are dependent on the carbon nanotubes; lowered by one order of magnitude if the carbon nanotubes are embedded in the device on the cathode
- Response time is improved by two orders of magnitude if carbon nanotubes are embedded in the device on the cathode
- Breakdown voltages are dependent on the density and aspect ratio of the carbon nanotubes; lowered by few volts if the intertube spacing is equal to height of the nanotubes

- The field enhancement factor  $\beta$  is improved by 3.6 times compared to gold nanowire based ionization gas sensor, and 28 times compared to the other carbon nanotube based ionization gas sensor.

Based on these findings, the improvement factors of some parameters of ionization gas sensor are calculated. These improvement factors are based on the simulation results of our enhanced PIC-MCC model and are mentioned in Table 4.4 to Table 4.6.

Table 4.4 Improvement factors of breakdown voltages

Parameters		Lowest Breakdown Voltage (V)	Improvement Factor
Fields	DC	170	58.82 %
	DC+RF	70	
Shape of electrodes	Planar	198	13.13 %
	Cylindrical	172	
Embedded CNTs	No	199	90.1 %
	Yes	19.7	
Gap Spacing with CNTs	10 $\mu$ m	19.7	28.93 %
	6 $\mu$ m	14	
Density variation effects	No	19.7	56.6 %
	Yes	8.55	

Table 4.5 Improvement factor of response time using enhanced model

Response time (without-CNT)	Response Time (with-CNT)	Improvement Factor
1.063 x 10 <sup>-10</sup> sec	3.3 x 10 <sup>-12</sup> sec	96.9%

Table 4.6 Improvement in field enhancement factor  $\beta$  using enhanced model

$\beta$ from AuNW based ionization gas sensor [93]	$\beta$ from other CNT based ionization gas sensor [180]	$\beta$ from our enhanced model	Improvement Factor (from AuNW)
37.9	3 ~ 5	136	72.1%

These improvement factors show that if the optimized data suggested with the help of our model is used, the performance of ionization gas sensor can be improved several times.

The percentage error in the improvement factors of our model was also calculated with the help of correlation coefficients calculated in the benchmarking phase. The lowest correlation coefficient calculated in comparison of our data with the experimental data is 0.957. That means, in the worst case our benchmarking results are 95.7 % matching with the experimental data and the mismatch is equal to 4.3 %. If the baseline simulations have maximum of 4.3 % mismatch with the experiments then, we can say that the improvement factors calculated for the enhanced model are true up to 95.7 % with a chance of error of 4.3 % from the calculated value.

In the end, it is also important to mention that these improvement factors are calculated according to the specific values of the parameters which we have provided at the input of our model. If it is desired to optimize the ionization gas sensor according to some particular application requirements, the input parameters can be assigned values accordingly to test the ionization gas sensor for that particular application.

#### 4.10 Summary

The chapter has started with the discussion and validation of the results of benchmarking. The breakdown voltage which is the key parameter to detect gas in ionization gas sensor is determined. The parameters which affect the breakdown

voltage of the gas are highlighted and their influence on the gas breakdown is studied. The detail discussion on the change in breakdown behavior with and without the carbon nanotube field emission model is provided along with the charged particles behavior between the electrodes. The breakdown voltages with new field emission model of carbon nanotubes are calculated by varying the gas pressure and gap spacing between the electrodes. The carbon nanotube aspect ratio and density which plays important role in the gas breakdown are also discussed. The lowest breakdown voltages are determined by reducing the electrostatic screening effects to minimum and fine tuning the density of the carbon nanotubes. The results are further validated by calculating the field enhancement factor  $\beta$ . The optimized data which is suggested with the help of our enhanced model is provided. Based on the suggested data, the improvement factors to improve the performance of ionization gas sensor are calculated.



## CHAPTER 5

### CONCLUSION

#### **5.1 Conclusion**

In this thesis, the field emission model of carbon nanotube based ionization gas sensor was successfully developed. Based on the working mechanism, the model was divided into three modules. These modules are (i) CNT field emission module (ii) CNT density and aspect ratio variation module and (iii) position and velocity assignment module. The modules are combined together and embedded in the standard PIC-MCC codes to make the enhanced version of PIC-MCC. The enhanced PIC-MCC codes were successfully used to study the gas detection mechanism in carbon nanotube based ionization gas sensor.

To test the functionality of the new model and comparison with the standard codes, the simulations were started by doing the benchmarking of the standard PIC-MCC codes. The benchmarking phase provided the basic understanding of various important parameters and laid the foundation to develop and test the new model. The results of the benchmarking were validated with the published data and the correlation coefficient was calculated to examine the closeness factor. Most of the correlation coefficients were in the range of 0.9, which shows the better agreement between our results and the published data. After completing the benchmarking phase, the new model was developed and tested. The gas detection mechanism of carbon nanotube based ionization gas sensor was simulated for the first time with the help of enhanced PIC-MCC model. Several simulation setups were prepared to test the complete functionality of each module. These various simulation setups helped to highlight different aspects in the working mechanism of the ionization gas sensor.

The results of the enhanced PIC-MCC model lead to some important findings which are useful to improve the performance of the ionization gas sensor. The breakdown voltages are dependent on various parameters e.g. nature of applied field, structure of the device, gap spacing, aspect ratio and density of the carbon nanotubes etc. The remarkable decrease in the breakdown voltage can be achieved if these parameters are controlled efficiently. The one order of magnitude decrease in the breakdown voltages is observed with the help of enhanced PIC-MCC model. The improvement factors in the breakdown voltages of around 29% and 56% can be achieved with the proper adjustment of the device gap spacing and the CNT density respectively. It was found that presence of carbon nanotubes in the ionization gas sensor changes the breakdown behavior which in turn affects the breakdown determination criteria. The two orders magnitude faster response time was also observed in the comparison of with-CNT and without-CNT device.

To further validate the results and to check the authenticity of our codes, the field enhancement factor  $\beta$  was calculated. The value of  $\beta$  of our enhanced model was verified by comparing with the  $\beta$  obtained from the well established and widely used model *hemisphere on post*. The closeness among the two values of  $\beta$  validates the performance and the results of our enhanced model. Furthermore, the  $\beta$  of our enhanced model was compared with the  $\beta$  of the existing ionization gas sensors. It was found that the  $\beta$  of our sensor is 3.6 times better than the  $\beta$  of the gold nanowire based ionization gas sensor and 28 times better than the  $\beta$  of the other CNT based ionization gas sensor. The reason for this increase in the value of  $\beta$  is the fine tuning of the aspect ratio and density parameters of the carbon nanotubes to enhance the field emission property.

Hence, our enhanced PIC-MCC codes paved the way for the optimization of carbon nanotube based ionization gas sensor.

## **5.2 Recommendations**

Based on this thesis, the following potential research projects are recommended.

- The optimized carbon nanotube based ionization gas sensor can be fabricated based on the useful data provided by our model. The efficiency of that ionization gas sensor will be improved several folds as suggested in the findings of this project.
- The field emission model of carbon nanotubes developed in this research can be modified for different nanomaterial structures such as gold nanowires and ZnO nanowires.



## REFERENCES

- [1] Pipeline Accident Report, "Natural Gas Pipeline Rupture and Fire Near Carlsberg, New Mexico, August 19, 2000," Washington D.C 2003.
- [2] P. H. Dai and B. M. Ling, "Study of a new gas sensor based on electrical conductance of gases in a high electric field," *China Instrum. Control Soc.*, vol. 19, pp. 239-244, 1998.
- [3] B. Ghodsian, *et al.*, "Gas detector with low-cost micromachined field ionization tips," *IEEE Electron Device Letters*, vol. 19, pp. 241-243, 1998.
- [4] Y. Zhang, *et al.*, "Study of gas sensor with carbon nanotube film on the substrate of porous silicon," presented at the IEEE 14th Intl. Vacuum Microelectronics Conf. Proc. , Boston, USA, 2001.
- [5] A. Modi, *et al.*, "Miniaturized gas ionization sensors using carbon nanotubes," *Nature*, vol. 424, pp. 171-174, 2001.
- [6] E. Comini, *et al.*, *Solid State Gas Sensing*. New York: Springer, 2009.
- [7] A. Mandelis and C. Christofides, *Physics, Chemistry and Technology of Solid State Gas Sensor Devices*: Wiley, 1993.
- [8] I. Lundstrom, *Sensors and Actuators B*, vol. 11, pp. 35-36, 1996.
- [9] M. J. Madou and S. R. Morrison., *Chemical Sensing with Solid State Devices*. New York: Academic Press, 1989.
- [10] P. T. Moseley, *Meas. Sci. Technology*, vol. 8, p. 223, 1997.
- [11] P. T. Moseley and B. C. Tofield, *Solid State Gas Sensors*: Adam Hilger, Bristol and Philadelphia, 1987.
- [12] S. Capone, *et al.*, "Solid State Gas Sensors: State of the Art and Future Activities," *Journal of Optoelectronics and Advanced Materials*, vol. 5, pp. 1335-1348, 2003.
- [13] Available: <http://www.figarosensor.com>
- [14] Available: <http://www.umweltsensortechnik.de>

- [15] G. Eranna, *et al.*, "Oxide Materials for Development of Integrated Gas Sensors - A Comprehensive Review," *Crit. Rev. Solid State Mater Sci.*, vol. 29, pp. 111-188, 2004.
- [16] J. W. Gardner and J. Yinon, *Electronic noses and sensors for the detection of explosives* vol. 159: Kluwer, 2004.
- [17] P. T. Moseley, *et al.*, *Techniques and mechanisms in gas sensing*. Bristol: Adam Hilger, 1991.
- [18] I. Lundstrom, *et al.*, "A hydrogen-sensitive MOS field-effect transistor," *Appl. Phys. Lett.*, vol. 26, pp. 55-57, 1975.
- [19] I. Lundstrom, *et al.*, "A hydrogen sensitive Pd-gate MOS transistor," *Jour. of Appl. Phys*, vol. 46, pp. 3876-3881, 1975.
- [20] I. Lundstrom, *et al.*, "Catalytic metals and field-effect devices - a useful combination," *Sensors and Actuators B1*, pp. 15-20, 1990.
- [21] S. Nakagomi and L. S. A., "Gas sensor device based on catalytic metal-Metal oxide -SiC structure," *Encyclopedia of sensors. Stevenson Ranch Ca. USA: American Scientific Publishers*, vol. 4, pp. 155-170, 2006.
- [22] A. Arbab, *et al.*, "Chemical sensors for high temperatures based on silicon carbide " *Sens. Mater*, vol. 4, pp. 173-185, 1993.
- [23] A. L. Spetz, *et al.*, "High temperature sensors based on metal-insulator-silicon carbide devices," *Phys Stat Sol (a)*, vol. 162, pp. 493-511, 1997.
- [24] A. L. Spetz, *et al.*, "SiC based field effect gas sensors for industrial applications," *Phys Stat Sol (a)*, vol. 185, pp. 15-25, 2001.
- [25] N. Miura, *et al.*, *Solid State Ionics*, vol. 86-88, p. 1069, 1996.
- [26] P. Elumalai, *et al.*, *J Electrochemical Soc.*, vol. 152, p. H95, 2005.
- [27] N. Miura, *et al.*, *Electrochem Solid-State Lett.*, vol. 9, p. H9, 2005.
- [28] N. Miura, *et al.*, *Sens Actuators B*, vol. 114, p. 903, 2006.
- [29] V. V. Plashnitsa, *et al.*, "Zirconia-based planar NO<sub>2</sub> sensor using ultrathin NiO or laminated NiO-Au sensing electrode," *Springer, Ionics*, vol. 14, pp. 15-25, 2008.
- [30] N. Miura, *et al.*, *Electrochem Commun.*, vol. 4, p. 284, 2002.
- [31] N. Miura, *et al.*, *Sens Actuators B*, vol. 93, p. 221, 2003.
- [32] M. Nakatou and N. Miura, *Electrochem Commun.*, vol. 6, p. 995, 2004.
- [33] M. Nakatou and N. Miura, *Solid State Ionics*, vol. 176, p. 2511, 2005.

- [34] R. Wama, *et al.*, *Electrochem Commun.*, vol. 9, p. 2774, 2007.
- [35] W. Demtroder, *Laser Spectroscopy, Basic Concepts and Instrumentation*. Berlin: Springer-Verlag, 1996.
- [36] R. Menzel, *Photonics Linear and NonLinear Interactions of Laser Light and Matter*. Berlin: Springer-Verlag, 2001.
- [37] S. Mukamel, *Principles of Nonlinear Optical Spectroscopy* New York: Oxford University Press, 1999.
- [38] N. Tkachenko, *Optical spectroscopy: methods and instrumentations*. Amsterdam: Elsevier, 2006.
- [39] H. Abramczyk, *Introduction to laser spectroscopy*. Amsterdam: Elsevier, 2005.
- [40] M. Sigrist, *Air Monitoring by Spectroscopic Techniques*. Somerset N.J: John Willey & Sons, 1994.
- [41] R. Azzam and N. Bashara, *Ellipsometry and Polarized Light*. Amsterdam, 1977.
- [42] S. Zangoie, *et al.*, "Vapour sensitivity of thin porous silicon layers," *Sens Actuators B Chem*, vol. 43, pp. 168-174, 1997.
- [43] G. Wang and H. Arwin, "Modification of vapour sensitivity in ellipsometric gas sensing by copper deposition in porous silicon," *Sens Actuator B Chem*, vol. 85, pp. 95-103, 2002.
- [44] S. Zangoie, *et al.*, "Water interaction with thermally oxidized porous layers," *J Electrochemical Soc.*, vol. 144, pp. 4027-4035, 1997.
- [45] J. Homola, *et al.*, "Surface plasmon resonance sensors: review," *Sens Actuator B Chem*, vol. 54, pp. 3-15, 1999.
- [46] S. Conoci, *et al.*, "Optical recognition of organic vapours through ultrathin calix[4]pyrrole films," *Colloid Surface Physicochem Eng Aspect*, vol. 198-200, pp. 869-873, 2002.
- [47] K. Kato, *et al.*, "Surface plasmon resonance properties and gas response in porphyrin Langmuir-Blodgett films," *Colloid Surface Physicochem Eng Aspect*, vol. 198-200, pp. 811-816, 2002.
- [48] M. G. Manera, *et al.*, "Investigation on alcohol vapours/TiO<sub>2</sub> nanocrystal thin films interaction by SPR technique for sensing application," *Sens Actuator B Chem*, vol. 100, pp. 75-80, 2004.

- [49] M. G. Manera, *et al.*, "TiO<sub>2</sub> nanocrystal films for sensing applications based on surface plasmon resonance," *Synthetic Met.*, vol. 148, pp. 25-29, 2005.
- [50] W. P. Hu, *et al.*, "A novel ultrahigh resolution surface plasmon resonance biosensor with an Au nanocluster-embedded dielectric film," *Biosens. and Bioelectron.*, vol. 19, pp. 1465-1471, 2004.
- [51] R. M. White and F. W. Voltmer, "Direct piezoelectric coupling to surface elastic waves," *Appl. Phys. Lett.*, vol. 12, p. 314, 1965.
- [52] C. K. Campbell, *Surface Acoustic Wave Devices for Mobile and Wireless Communications*. San Diego: Academic Press, 1998.
- [53] A. Rugemer, *et al.*, "Surface acoustic wave NO<sub>2</sub> sensing using attenuation as the measured quantity," *Sens Actuator B* vol. 56, pp. 45-49, 1999.
- [54] H. Becker, *et al.*, "A new sensor principle based on the reflection of surface acoustic waves," *Sens Actuator A*, vol. 54, pp. 618-621, 1996.
- [55] S. J. Martin and A. J. Ricco, "Effective utilization of acoustic wave sensor responses: Simultaneous measurement of velocity and attenuation," in *Proc. of the IEEE Ultrasonics Symposium*, 1989, pp. 621-625.
- [56] W. P. Jakubik, *et al.*, "Investigations on the resistance of the metal-free phthalocyanine and palladium bilayer sensor structure influenced by hydrogen" *Sens Actuator B*, vol. 105, pp. 340-345, 2005.
- [57] W. P. Jakubik, *et al.*, "Palladium and phthalocyanine bilayer films for hydrogen detection in a surface acoustic waves sensor system," *Sens Actuator B*, vol. 96, pp. 321-328, 2003.
- [58] W. P. Jakubik, *et al.*, "Bilayer structure for hydrogen detection in a surface acoustic wave sensor system," *Sens Actuator B*, vol. 82, pp. 265-271, 2002.
- [59] S. J. Ippolito, *et al.*, "Layered SAW hydrogen sensor with modified tungsten trioxide selective layer," *Sens Actuator B*, vol. 108, pp. 553-557, 2005.
- [60] S. J. Ippolito, *et al.*, "A layered surface acoustic waves ZnO/LiTaO<sub>3</sub> structure with a WO<sub>3</sub> selective layer for hydrogen sensing," *Sens. Lett.*, vol. 1, pp. 33-36, 2003.
- [61] S. J. Ippolito, *et al.*, "Highly sensitive layered ZnO/LiNbO<sub>3</sub> SAW device with InOx selective layer for NO<sub>2</sub> and H<sub>2</sub> gas sensing," *Sens Actuator B*, vol. 111, pp. 207-212, 2005.

- [62] S. J. Ippolito, *et al.*, "Layered SAW nitrogen dioxide sensor based on a ZnO/36°YX LiTaO<sub>3</sub> structure with WO<sub>3</sub> selective layer," in *Proc. of the 2003 IEEE Intl. Freq. Cont. Symp.*, 2003, pp. 931-934.
- [63] S. J. Ippolito, *et al.*, "A layered SAW based NO<sub>2</sub> sensor with a copper phthalocyanine selective layer," presented at the Proc. of the Conf. on Optoelectronic and microelectronic materials and devices, 2002.
- [64] S. J. Ippolito, *et al.*, "Ethanol sensor based on layered WO<sub>3</sub>/ZnO/36° YX LiTaO<sub>3</sub> SAW devices," presented at the Proc. of TRANSDUCERS '05, 2005.
- [65] D. A. Powell, *et al.*, "Layered surface acoustic waves chemical and bio-sensors " *Encyclopedia of sensors. Stevenson Ranch Ca. USA: American Scientific Publishers*, 2006.
- [66] H. Wohltjen, *et al.*, "Surface acoustic-wave probe for chemical-analysis .1. Introduction and Instrument Description," *Anal. Chem.*, vol. 51, pp. 1458-1464, 1979.
- [67] M. Thompson and D. C. Stone, *Surface-launched acoustic wave sensors. chemical sensing and thin-film characterization* New York: John Wiley & Sons, 1997.
- [68] E. L. Adler, "SAW and pseudo-SAW properties using matrix-methods," *IEEE Trans. Ultrason Ferr.*, vol. 41, pp. 876-882, 1994.
- [69] D. A. Powell, *et al.*, "Numerical calculation of SAW sensitivity: Application to ZnO /LiTaO<sub>3</sub> Transducers," *Sens Actuator A*, vol. 115, p. 456, 2004.
- [70] S. J. Ippolito, *et al.*, "A 3-dimensional finite element approach for simulating acoustic wave propagation in layered SAW devices " presented at the Proc. on IEEE Symp. on Ultrasonics 2003.
- [71] R. J. Wilfinger, *et al.*, "Resonistor - a frequency selective device utilizing mechanical resonance of a silicon substrate," *IBM J Res. Develop*, vol. 12, pp. 113-118, 1968.
- [72] T. M. S. Heng, "Trimming of microstrip circuits utilizing microcantilever air gaps," *IEEE Trans. Microw. Theor. Techn.*, vol. 19, pp. 652-654, 1971.
- [73] K. E. Petersen, "Micromechanical membrane switches on silicon " *IBM J Res. Develop*, vol. 23, pp. 376-385, 1979.
- [74] E. S. Kolesar, United States Patent 4549427, 1983.
- [75] G. Binnig, *et al.*, *Phys. Rev. Lett.*, vol. 56, pp. 930-933, 1986.

- [76] Z. Hu, *et al.*, "Investigation of adsorption and adsorption-induced stresses using microcantilever sensors," *J. Appl. Phys.*, vol. 90, pp. 427-431, 2001.
- [77] D. R. Balselt, *et al.*, "Design and performance of microcantilever-based hydrogen sensor " *sens Actuator B*, vol. 88, pp. 120-131, 2003.
- [78] A. Fabre, *et al.*, "Monitoring the chemical changes in Pd induced by hydrogen adsorption using microcantilevers," *Ultramicroscopy*, vol. 97, p. 425, 2002.
- [79] T. Ono, *et al.*, "Mass sensing of adsorbed molecules in sub-picogram sample with ultrathin silicon resonator," *Rev Sci. Instrum*, vol. 74, pp. 1240-1243, 2003.
- [80] J. Zhou, *et al.*, "Self excited piezoelectric microcantilever for gas detection," *Microelectr Eng.*, vol. 69, pp. 37-46, 2003.
- [81] J. D. Adams, *et al.*, "Piezoelectric self-sensing of adsorption-induced microcantilever bending," *Sens Actuator A*, vol. 121, pp. 457-461, 2005.
- [82] T. L. Porter, *et al.*, "A solid state sensor platform for the detection of hydrogen cyanide gas," *sens Actuator B*, vol. 123, pp. 313-317, 2007.
- [83] H. Jensenius, *et al.*, "A microcantilever based alcohol vapour sensor-application and response model " *Appl. Phys. Lett.*, vol. 76, pp. 2815-2817, 2000.
- [84] K. B. Brown, *et al.*, "Micro structural pressure sensor based on an enhanced resonant mode hysteresis effect " *J Vac Sci Technol B*, vol. 19, pp. 1628-1632, 2001.
- [85] K. B. Brown, *et al.*, "Simple resonating microstructure for gas pressure measurement," *J Micromech Microeng*, vol. 12, pp. 204-210, 2002.
- [86] Y. Su, *et al.*, "Characterization of a highly sensitive ultrathin piezo-resistive silicon cantilever probe and its application in gas flow velocity sensing," *J Micromech Microeng*, vol. 12, pp. 780-785, 2002.
- [87] J. Mertens, *et al.*, "Effects of temperature and pressure on microcantilever resonance response " *Ultramicroscopy*, vol. 97, pp. 119-126, 2003.
- [88] V. Mortet, *et al.*, "Wide range pressure sensor based on a piezoelectric bimorph microcantilever," *Appl. Phys. Lett.*, vol. 88, p. 133511, 2006.
- [89] Z. Hou, *et al.*, "A MEMS-based ionization gas sensor using carbon nanotubes," *IEEE Electron Device Letters*, vol. 54, pp. 1545-1548, 2007.

- [90] Z. Hou, *et al.*, "MEMS-based microelectrode system incorporating carbon nanotubes for ionization gas sensing," *Sens Actuator B*, vol. 127, pp. 637-648, 2007.
- [91] J. Wu, *et al.*, "A MEMS-based ionization gas sensor using carbon nanotubes and dielectric barrier," in *IEEE Proc. 3rd Intl. Conf. Nano/Micro Engineered and Molecular Systems*, Sanya, China, 2008, pp. 824-827.
- [92] X. Chen, *et al.*, "Ionization Sensors Using Well-aligned MWCNT Arrays Grown in Porous AAO Template," in *IEEE Proc. Intl. Conf. on Information Acquisition*, Hong Kong and Macau, China, 2005, pp. 290-293.
- [93] R. B. Sadeghian and M. Kahrizi, "A novel miniature gas ionization sensor based on freestanding gold nanowires," *Sens Actuator A*, vol. 137, pp. 248-255, 2007.
- [94] R. B. Sadeghian and M. Kahrizi, "A low voltage gas ionization sensor based on sparse gold nanorods," presented at the IEEE Sensors Conf., 2007.
- [95] R. B. Sadeghian and M. Kahrizi, "A novel gas sensor based on tunneling-field-ionization on whisker-covered gold nanowires," *IEEE Sensors Journal*, vol. 8, pp. 161-169, 2008.
- [96] K. Zhao, *et al.*, "Field Ionization from ZnO Nanorod Arrays for Detecting Formic Acid in Air," presented at the IEEE Proc. Intl. Conf. on Information Acquisition, Jeju City, Korea, 2007.
- [97] N. Azmoodeh, *et al.*, "A Silver Nanowire Based Gas Ionization Sensor," in *IEEE EUROCON 2009*, pp. 1231-1235.
- [98] F. Paschen, *Ann. Phys.*, vol. 273, p. 69, 1889.
- [99] J. S. Townsend, "The Theory of Ionization of Gases by Collision," *Constable & Company Ltd. London*, 1910.
- [100] A. D. MacDonald and S. C. Brown, "High-Frequency Gas-Discharge Breakdown in Helium," Research Laboratory of Electronics, MIT Technical Report No. 86, 1948.
- [101] M. A. Herlin and S. C. Brown, "Electrical Breakdown of a Gas between Coaxial Cylinders at Microwave Frequencies," Research Laboratory of Electronics, MIT Technical Report No. 72, 1948.

- [102] S. C. Brown and J. J. McCarthy, "A Microwave Gas Discharge Counter for the Detection of Ionizing Radiation," Research Laboratory of Electronics, MIT Technical Report No. 75, 1948.
- [103] M. A. Herlin and S. C. Brown, "Microwave Breakdown of a Gas in a Cylindrical Cavity of Arbitrary Length," Research Laboratory of Electronics, MIT Technical Report No. 77, 1948.
- [104] B. Lax, *et al.*, "The Effect of Magnetic Field on the Breakdown of Gases at Microwave Frequencies," Research Laboratory of Electronics, MIT Technical Report No. 165, 1950.
- [105] X. Xu, *et al.*, "Prediction of Breakdown in SF<sub>6</sub> Under Impulse Conditions," *IEEE Trans. on Dielectrics and Electrical Insulation*, vol. 3, pp. 836-842, 1996.
- [106] P. Osmokrovic and G. Djogo, "Applicability of Simple Expressions for Electrical Breakdown Probability in Vacuum," *IEEE Trans. on Electrical Insulation*, vol. 24, pp. 943-947, 1989.
- [107] P. Osmokrovic and N. Kartalovic, "Applicability of Simple Expressions for Electrical Breakdown Probability Increase in Vacuum and Gas," *IEEE Trans. on Power Systems*, vol. 12, pp. 1455-1460, 1997.
- [108] P. Osmokrovic, *et al.*, "Mechanism of Electrical Breakdown Left of Paschen Minimum," *IEEE Trans. on Dielectrics and Electrical Insulation*, vol. 1, pp. 77-81, 1994.
- [109] P. Osmokrovic, "Mechanism of Electrical Breakdown of Gases at Very Low Gas Pressure and Interelectrode Gap Values," *IEEE Trans. on Plasma Science*, vol. 21, pp. 645-653, 1993.
- [110] G. Djogo and P. Osmokrovic, "Statistical Properties of Electrical Breakdown in Gases," *IEEE Trans. on Electrical Insulation*, vol. 24, pp. 949-953, 1989.
- [111] J. M. Meek and J. D. Craggs., *Electric Breakdown of Gases: The Clarendon Press, Oxford*, 1953.
- [112] Y. P. Raizer, *Gas Discharge Physics: Springer-Verlag*, 1991.
- [113] R. H. Good and E. W. Muller, "Field Emission," *Handbuch der physik*, vol. 21, p. 176, 1956.
- [114] W. P. Dyke and W. W. Dolan, *Adv Electron Electron Phys*, vol. 8, p. 89, 1956.
- [115] J. W. Gadzuk and E. W. Plummer, *Rev Mod Phys*, vol. 45, p. 487, 1973.

- [116] R. Gomer, "Field emission, field ionization, and field desorption," *Surf Sci.*, vol. 299/300, pp. 129-152, 1994.
- [117] S. Iijima, "Helical Microtubules of Graphitic Carbon," *Nature*, vol. 354, pp. 56-58, 1991.
- [118] L. A. Chernozatonskii, *et al.*, *Chem Phys Lett.*, vol. 233, p. 63, 1995.
- [119] A. G. Rinzler, *et al.*, *Science*, vol. 269, p. 1550, 1995.
- [120] W. A. D. Heer, *et al.*, *Science*, vol. 270, p. 1179, 1995.
- [121] Q. H. Wang, *et al.*, "A nanotube-based field-emission flat pannel display," *Appl. Phys. Lett.*, vol. 72, pp. 2912-2913, 1998.
- [122] Y. Saito, *et al.*, "Field emission from multi-walled carbon nanotubes and its application to electron tubes," *Appl. Phys. A*, vol. 67, pp. 95-100, 1998.
- [123] J. M. Bonard, *et al.*, "Carbon nanotube films as electron field emitters," *Carbon*, vol. 40, pp. 1715-1728, 2002.
- [124] J. M. Bonard, *et al.*, "Field emission from single-wall carbon nanotube films," *Appl. Phys. Lett.*, vol. 73, p. 918, 1998.
- [125] A. M. Rao, *et al.*, *appl. Phys. Lett.*, vol. 76, p. 3813, 2000.
- [126] H. Manohara, *et al.*, "Field emission testing of carbon nanotubes for THz frequency vacuum microtube sources," *SPIE Proceedings*, vol. 5343, p. 227, 2003.
- [127] T. W. Ebbesen and P. M. Ajayan, "Large scale synthesis of carbon nanotubes," *Nature*, vol. 358, pp. 220-222, 1992.
- [128] S. Iijima and T. Ichihashi, "Single-shell carbon nanotubes of 1-nm diameter," *Nature*, vol. 363, pp. 603-615, 1993.
- [129] D. S. Bethune, *et al.*, "Cobalt-catalysed growth of carbon nanotubes with single-atomic-layer walls," *Nature*, vol. 363, pp. 605-607, 1993.
- [130] J. M. Bonard, *et al.*, "Field emission properties of mltiwalled carbon nanotubes," *Ultramicroscopy*, vol. 73, p. 7, 1998.
- [131] P. J. d. Pablo, *et al.*, *Appl. Phys. Lett.*, vol. 75, p. 3941, 1999.
- [132] X. Xu and G. R. Brandes, *Appl. Phys. Lett.*, vol. 74, p. 2549, 1999.
- [133] S. K. Srivastava, *et al.*, "Excellent Field Emission Properties of Short Conical Carbon Nanotubes Prepared by Microwave Enhanced CVD Process," *Nnaoscale Res. Lett.*, vol. 3, pp. 25-30, 2008.

- [134] J. L. Silan, *et al.*, "Novel Geometry of Carbon Nanotube Field Emitter to Achieve High Current Densities for Terahertz Sources," in *IEEE*, 2009.
- [135] S. I. Jung, *et al.*, "Highly improved field emission properties from organic binder-free carbon nanotube emitters fabricated by filtration transfer technique," *Technical Digest of IVNC*, pp. 261-262, 2009.
- [136] J. M. Bonard, *et al.*, "Field emission from carbon nanotubes: the first five years," *Solid State Electron*, vol. 45, p. 893, 2001.
- [137] K. B. K. Teo, *et al.*, "Field emission from dense, sparse, and patterned arrays of carbon nanofibres," *Appl. Phys. Lett.*, vol. 80, pp. 2011-2013, 2002.
- [138] W. Zhu, *et al.*, *Appl. Phys. Lett.*, vol. 75, p. 873, 1999.
- [139] O. M. Kuttel, *et al.*, *Carbon*, vol. 37, p. 745, 1999.
- [140] L. Nilsson, *et al.*, "Scanning field emission from patterned carbon nanotube films," *appl. Phys. Lett.*, vol. 76, pp. 2071-2073, 2000.
- [141] R. C. Smith, *et al.*, "Calculation of field enhancement factor and screening effects in carbon nanotube arrays," *IEEE* pp. 171-172, 2007.
- [142] R. C. Smith, *et al.*, "Maximizing the electron field emission performance of carbon nanotube arrays," *Appl. Phys. Lett.*, vol. 94, pp. 133104-6, 2009.
- [143] J. S. Suh, *et al.*, "Study of the field screening effect of highly ordered carbon nanotube arrays," *Appl. Phys. Lett.*, vol. 80, p. 2392, 2002.
- [144] S. M. Yoon, *et al.*, "Comparison of the field emissions between highly ordered carbon nanotubes with closed and open tips," *Appl. Phys. Lett.*, vol. 84, pp. 825-827, 2004.
- [145] J. Yun, *et al.*, "Field emission from a large area of vertically-aligned carbon nanofibres with nanoscale tips and controlled spatial geometry," *Carbon*, vol. 48, pp. 1362-1368, 2010.
- [146] R. G. Forbes, *et al.*, "Some comments on models for field enhancement," *Ultramicroscopy*, vol. 95, pp. 57-65, 2003.
- [147] P. K. Tein and J. Moshman, *J. Appl. Phys.*, vol. 27, p. 1067, 1956.
- [148] O. Buneman, *Phys. Rev.*, vol. 115, p. 503, 1959.
- [149] C. K. Birdsall and W. B. Bridges, *J. Appl. Phys.*, vol. 32, p. 2611, 1961.
- [150] J. M. Dawson, *Phys. Fluids*, vol. 2 p. 445, 1962.
- [151] D. B. Graves, *J. Appl. Phys.*, vol. 62, p. 88, 1987.
- [152] D. B. Graves and K. F. Jensen, *IEEE Trans. Plasma Sci.*, vol. 14, p. 92, 1986.

- [153] T. Makabe and N. Nakano, *Phys. Rev. A*, vol. 45, p. 2520, 1992.
- [154] S. K. Park and D. J. Economou, *J. Appl. Phys.*, vol. 68, p. 3904, 1990.
- [155] H. C. Kim, *et al.*, "Particle and fluid simulations of low-temperature plasma discharges: benchmarks and kinetic effects " *Jour. of Appl. Phys D: Appl. Phys.*, vol. 38, pp. R283-R301, 2005.
- [156] C. K. Birdsall, "Particle-In-Cell Charged-Particle Simulations, Plus Monte Carlo Collisions With Neutral Atoms, PIC-MCC," *IEEE Trans. on Plasma Science*, vol. 19, pp. 65-85, 1991.
- [157] C. K. Birdsall and A. B. Langdon, *Plasma Physics Via Computer Simulation*. New York: Taylor & Francis Group, LLC, 1991.
- [158] T. Tajima, *Computational Plasma Physics*. Red wood city: Addison-Wesley, 1988.
- [159] R. W. Hockney and J. W. Eastwood, *Computer Simulation Using Particles*. New York: McGraw-Hill, 1981.
- [160] J. P. Verboncoeur, *et al.*, "Simultaneous Potential and Circuit Solution for 1D Bounded Plasma Particle Simulation Codes," *Jour. of Computational Phys.*, vol. 104, p. 321, 1993.
- [161] V. Vahedi and M. Surendra, "A Monte Carlo collision model for a particle-in-cell method: applications to argon and oxygen discharges," *Computer Physics Comm.*, vol. 87, pp. 179-198, 1995.
- [162] M. Surendra and D. B. Graves, *IEEE Trans. on Plasma Science*, vol. 19, p. 144, 1991.
- [163] M. M. Turner and H. B. Hopkins, *Phys. Rev. Lett.*, vol. 69, p. 3511, 1992.
- [164] T. J. Sommerer and M. J. Kushner, *J. Appl. Phys.*, vol. 71, p. 1654, 1992.
- [165] M. J. Kushner, *J. Appl. Phys.*, vol. 95, p. 846, 2004.
- [166] J. K. Lee and C. K. Birdsall, *Phys. Fluids*, vol. 22, p. 1315, 1979.
- [167] V. Vahedi and G. Dipeso, "Simultaneous Potential and Circuit Solution for Two-Dimensional Bounded Plasma Simulation Codes," *Jour. of Computational Phys.*, vol. 131, pp. 149-163, 1997.
- [168] J. P. Verboncoeur, *et al.*, "An object-oriented electromagnetic PIC code," *Computer Physics Comm.*, vol. 87, pp. 199-211, 1995.
- [169] A. B. Langdon, *Jour. of Computational Phys.*, vol. 6, p. 247, 1970.
- [170] A. B. Langdon and C. K. Birdsall, *Phys. Fluids*, vol. 13, p. 2115, 1970.

- [171] H. Okuda, *Jour. of Computational Phys.*, vol. 10, p. 475, 1972.
- [172] L. Chen and A. B. Langdon, *Jour. of Computational Phys.*, vol. 14, p. 200, 1974.
- [173] E. Kawamura, *et al.*, *Plasma Sour. Sci. Technol.*, vol. 9, p. 413, 2000.
- [174] V. A. Godyak and R. B. Peijak, "Abnormally Low Electron Energy and Heating-Mode Transition in a Low Pressure Argon rf Discharge at 13.56 MHz" *Phys. Rev. Lett.*, vol. 65, pp. 996-999, 1990.
- [175] H. C. Kim, *et al.*, "Particle-In-Cell Monte-Carlo Simulation of Capacitive RF Discharges: Comparison with Experimental Data," *Japanese Journal of Applied Physics*, vol. 44, pp. 1957-1958, 2005.
- [176] M. R. Radjenovic and B. Radjenovic, "A Particle-In-Cell Simulation of the High-Field Effect in Devices with Micrometer Gaps," *IEEE Trans. on Plasma Science*, vol. 35, pp. 1223-1228, 2007.
- [177] M. R. Radjenovic, *et al.*, "Modelling of breakdown behavior by PIC/MCC code with improved secondary emission models," *IOP Publishing, Journal Of Physics: Conference Series*, vol. 71, pp. 1-19, 2007.
- [178] V. A. Lisovsky and V. D. Yegorenkov, "Low pressure gas breakdown in combined field," *Jour. of Appl. Phys D: Appl. Phys.*, vol. 27, pp. 2340-2348, 1994.
- [179] T. Ito, *et al.*, *Thin Solid Films*, vol. 386, pp. 300-304, 2001.
- [180] Y. Zhang, *et al.*, "The structure optimization of the carbon nanotube film cathode in the application of gas sensor," *Sens Actuator A*, vol. 128, pp. 278-289, 2006.

## PUBLICATIONS

### Conference Papers

1. S. Mahmood, Z. A. Burhanudin, and N. H. Hamid, "Effects of CNT density variation in field emission model of ionization gas sensor", accepted in IEEE-RSM 2011, Kota Kinabalu, Malaysia, Sep. 28-30, 2011.
2. S. Mahmood, Z. A. Burhanudin, and N. H. Hamid, "Field emission model of CNT based ionization gas sensor", in press, AIP conf. proc. NanoSciTech 2011, Shah Alam, Malaysia, Mar. 2-3, 2011.
3. S. Mahmood, Z. A. Burhanudin, and N. H. Hamid, "Simulation of electron densities and breakdown voltages in argon-filled cylindrical electrodes", IEEE ICEDSA, pp. 436-439, 2010.
4. S. Mahmood, Z. A. Burhanudin, and N. H. Hamid, "Electron densities in radio frequency argon discharge simulated using PIC-MCC", IEEE-RSM 2009, Kota Bahru, Malaysia, Aug. 10-12, 2009.
5. S. Mahmood, Z. A. Burhanudin, and N. H. Hamid, "Realization of ionization gas sensor design; A review", Symposium on Engineering & Technology (SET) 2008, 14-17 Dec. 2008, Labuan, Malaysia.

### Journal Paper

1. S. Mahmood, Z. A. Burhanudin, Nor Hisham Hamid, "Field emission model of carbon nanotubes to simulate gas breakdown in ionization gas sensor," to be submitted, Journal of Molecular Graphics and Modeling, Elsevier.



## APPENDIX A

### CODES

#### A.1 XPDP1 Source pdp1.h in Modified Form

```
#include <math.h>
#include <stdio.h>
//#include <unistd.h>
#include <stdlib.h>

#define EPS0      8.8542e-12          /* (F/m) */
#define NperTORR 8.3221e20
#define NSMAX     7
#define HISTMAX   32768             /* upper bound on histories */

#ifndef max
#define max(x, y)  (((x) > (y)) ? (x) : (y))
#endif

#ifndef min
#define min(x, y)  (((x) < (y)) ? (x) : (y))
#endif

#ifndef DBL_MIN
#define DBL_MIN    1E-200
#endif

#ifndef FLOAT_MIN
```

```
#define FLOAT_MIN      1e-4
#endif

#ifndef DEN_MIN
#define DEN_MIN      1
#endif

#ifndef True
#define True          1
#endif

#ifndef False
#define False         0
#endif

#ifndef M_PI
#define M_PI  3.14159265358979323846
#endif

#ifndef onesixth
#define onesixth 0.1666666667
#endif

#ifndef one24
#define one24 0.041666667
#endif

#ifndef one12
#define one12 0.0833333333
#endif

#ifndef onethird
#define onethird 0.3333333333
```

```

#endif

#ifndef twot thirds
#define twot thirds 0.666666667
#endif

#ifdef linux
#define cosd(d) (cos(M_PI*d/180))
#define sind(d) (sin(M_PI*d/180))
#endif

#define BIT_REVERSE 1
#define RANDOM 0

#define sqr(a) ((a)*(a))

/* PG, attempt to read the gas type from input deck */
#define HELIUM 1
#define ARGON 2
#define NEON 3
#define OXYGEN 4
#define MCC 5

/*****

float nc2p, length, area, nm_h, nm_d, rhoback, backj, dde, epsilon, b, psi, extr,
      extl, extc, w0, dcbias, acbias, extq, extq_1, extq_2, extq_3,
      exti, sigma, oldsigma, dx, dt, vxscale, vscale, xnc, pressure,
      gtemp, ramp, theta0, risetime, seec[NSMAX], nmeec[NSMAX], jwall[NSMAX],
      jnorm[NSMAX],
      q[NSMAX], m[NSMAX], qm[NSMAX], jj0[NSMAX][2], v0[NSMAX][2],

```

```

        vt[NSMAX][2],    vc[NSMAX][2],    v0y[NSMAX],    vty[NSMAX],
        v0z[NSMAX],    vtz[NSMAX],
tx[NSMAX],    tz[NSMAX],    sx[NSMAX],    sz[NSMAX],    emin[NSMAX],
de[NSMAX],dtheta[NSMAX],enter[NSMAX][2],emin_mid[NSMAX],
de_mid[NSMAX],xs_mid[NSMAX],xf_mid[NSMAX],a_scale[NSMAX],
sp_chi_scale[NSMAX],
    Escale[NSMAX],jdote_scale[NSMAX],j_scale[NSMAX], elect_perdt, elect_persec;

int    nsp, nc, ng, secondary, ionspecies, nm, nm_den, int_spc, ecollisional,
icollisional,
        hist_hi, thist_hi, freq_hi, interval, nsmoothing, n timestep,
        nfft, n_ave, dcramped, reflux, np[NSMAX], nbin[NSMAX],
        inject[NSMAX],    nbin_mid[NSMAX],    sp_k[NSMAX],    it[NSMAX],
maxnp[NSMAX],
        k_count[NSMAX], ndiag, gas, psource, nstrt, vel_dist_accum,
                                vxloader[NSMAX][2],
vyloader[NSMAX], vzloader[NSMAX], N_trapped[NSMAX],
                                N_untrapped[NSMAX],
E_trapped[NSMAX], E_untrapped[NSMAX], E_particles[NSMAX];

long int seed;

double t;

char src, **rate_title;

float **x, **vx, **vy, **vz, **sp_n, *rho, *e, *phi, *a, *x_grid,
        **fe, **ftheta, **e_array, **th_array, **fe_mid, **fe_mid_show,
                                **sp_fe_ave, **sp_fe_show, **sp_fe,
        **e_mid_array, *e_ave, *e_ave_show, *phi_ave, *phi_ave_show,
        **sp_n_ave, **sp_n_ave_show,
        **sp_n_0, **sp_n_k, **sp_n_mcc, *chi,

```

```

**jdote, **jdote_show, **mccrate, **rate_show, **np_trapped, **np_untrapped,
**kes_x_hist, **TE_trapped, **TE_untrapped, **TE_particle;

```

```

/* stuff for history diagnostics */

```

```

float *t_array, **np_hist, **jwall_hist, **phi_hist,
      *wall_sigma_hist, *ese_hist,
          **kes_hist, **kes_x_hist, **kes_y_hist, **kes_z_hist,
          *cur_hist,
      *com_cur_hist, *pow_hist, *com_pow_hist, **com_phi_hist, *f_array,
      *cur_fft, *phi_fft, *pow_fft, *mphi_fft, *Local_t_array;

```

```

/* stuff for velocity moments diagnostics */

```

```

float **sp_ke_x, **sp_ke_y, **sp_ke_z,
      **sp_ke_x_show, **sp_ke_y_show, **sp_ke_z_show,
          **sp_ke_x_ave, **sp_ke_y_ave, **sp_ke_z_ave,
          **sp_ke_x_ave_show, **sp_ke_y_ave_show,
**sp_ke_z_ave_show,
          **sp_ke_show, **sp_ke_ave_show,
          **sp_j_x, **sp_j_y, **sp_j_z,
          **sp_j_x_show, **sp_j_y_show, **sp_j_z_show,
          **sp_j_x_ave, **sp_j_y_ave, **sp_j_z_ave,
          **sp_j_x_ave_show, **sp_j_y_ave_show,
**sp_j_z_ave_show, **sp_u_x_show, **sp_u_y_show, **sp_u_z_show,
**sp_u_x_ave_show, **sp_u_y_ave_show, **sp_u_z_ave_show, **Tx_ave, **Ty_ave,
**Tz_ave, **Tx_ave_show, **Ty_ave_show, **Tz_ave_show, **T_ave_show;

```

```

/*stuff for velocity distribution diagnostics*/

```

```

float ***vx_dist, **vx_array, ***vy_dist, **vy_array, ***vz_dist, **vz_array;
float vxu[NSMAX], vxl[NSMAX], vyu[NSMAX], vyl[NSMAX], vzu[NSMAX],
vzl[NSMAX];
int nvxbin[NSMAX], nvybin[NSMAX], nvzbin[NSMAX];

```

```

/*stuff for the volume source */
float endpts[2], vol_source, ionization_energy;

/*stuff for injection*/
float eold[2], W[NSMAX], sin4W[NSMAX], sin22W[NSMAX], cos22W[NSMAX],
cos_psi, sin_psi;

float frand(void), tstrt;
//float bit_rever_maxwellian(void), maxwellian(void), maxwellian_flux(void);
float maxwellian(int);
// maxwellian_flux(int);
float distribution(int,int,int), distribution_flux(int,int,int);
void maxwellv(float *, float *, float *, float);
double revers_base(int,int), base2(void), revers(unsigned int);
void history(void), gather(int), adjust(int);
int start(void);
void fields(void), setrho(void);
void imp_move(int isp, const int EnergyFlag), exp_move(int isp, const int
EnergyFlag), (*moveptr)(int isp, const int EnergyFlag);
void (*mccptr)(int isp);
void mccddiag_init(void);
void heliummcc(int isp), argonmcc(int isp), neonmcc(int isp), oxygenmcc(int isp),
mcc(int isp);

```

## A.2 XPDP1 Source start.c in Modified Form

```

#include "pdp1.h"
#include "xgrafx.h"

/*****
/* Routine to adjust (initialize, re-pack and inject) particles */
/* to the desired boundary conditions */

```

```

void injection_push(int species, int particle, float part_time);
void injection_push_oldpdp(int species, int particle, float part_time);
void injection_push_FTSBP(int species, int particle, float part_time);
void injection_push_MBP(int species, int particle, float part_time);
void injection_push_FG(int species, int particle, float part_time);

```

```

void sterm(int number);
void ionization(int number);

```

```

void adjust(int isp)
{
    static int ionsp, npold;
    static int secsp, nmsp, nm_densp, init_flag=1;
    static float extra[NSMAX][2];
    static float this_time;

    register int i, ii, j, k, q;
    int nnp, secountl=0, secountr=0;
    // float secountl=0, secountr=0;
    int nreflux[NSMAX], s;
    float dum, del_t=0;

    /* INITIALIZE array for computing positions of injected particles */
    if (init_flag) {

        ionsp = ionspecies-1;
        secsp = secondary -1;
        nmsp = nm -1;
        nm_densp = nm_den -1;

        /* "enter" is now the no. of particles injected each "dt" */
        for (i=0; i<nsp; i++) {

```

```

    if (fabs(enter[i][0]) > 0.) extra[i][0] = 0.5123123;
    else extra[i][0] = 0.;
    if (fabs(enter[i][1]) > 0.) extra[i][1] = 0.5123123;
    else extra[i][1] = 0.;
}
init_flag = 0;
}

if (psource && (isp == ionsp))
    npold = np[ionsp]; /* Save the number of ions before adjust */

if (isp==0) // secondaries add to jwall[secsp] not jwall[isp]
    for (i=0; i<nsp; i++)
        jwall[i]=0;

if(secondary) secountr = secountr = 0;
nreflux[isp]= 0; /* nreflux[isp] equals zero */

if (np[isp] > 0) {
    nnp = np[isp] -1;
    i = 0;

    /* eliminate "outsiders", allow for secondary electron emission, */
    /* and if it left thru LH plate, ADD charge there to sigma */
    /* (plate surface density). */

    /* note: the system starts at 0 (includes 0) and end before xnc */
    /****** DOES NOT INCLUDE xnc *****/

do {
    if (x[isp][i] >= xnc) {
        x[isp][i] = x[isp][nnp];

```

```

vx[isp][i] = vx[isp][nnp];
vy[isp][i] = vy[isp][nnp];
vz[isp][i] = vz[isp][nnp];
nnp--;
if(reflux) nreflux[isp]++;
else if(secondary) {
    if (frand() < seec[isp]){
        secountr++;
    }
}
if (nm) {
    if (phi[0] <= 7.5){
        if (frand() < nmeec[isp]) {
            secountr=secountr+1;
        }
    }

    /* if (e[nc] > 7.5e5) { */
    else
        if (frand() < nmeec[isp]){
            secountr=secountr+2;
        }

}

if (nm_den) {
    if (int_spc < 1) {
        if (phi[0] <= 8.5){
            if(frand() < nmeec[isp]){
                secountr = secountr+1;
            }
        }
    }
}

```

```

else
    if (frand() < nmeec[isp]){
        secountr = secountr+2;
    }
}
else

if (int_spc==1) {
    if (phi[0] <=5.0){
        if (frand() < nmeec[isp]) {
            secountr =secountr+1;
        }
    }
}
else
    if (frand() < nmeec[isp]) {
        secountr=secountr+2;

    }
}
else
if (int_spc==2){
    if (phi[0] <= 6.5){
        if (frand() < nmeec[isp]){
            secountr = secountr+1;
        }
    }
}
else
    if (frand() <nmeec[isp]){
        secountr = secountr+2;
    }
}
else
    if (int_spc==3){

```

```

        if(phi[0] <= 7.5){
            if (frand() < nmeec[isp]){
                secountr = secountr+1;
            }
        }
        else
            if (frand() < nmeec[isp]){
                secountr = secountr+2;
            }
        }
    }
}
else if (x[isp][i] < 0) {
    /***** LHS wall diagnostics *****/
    if(theRunWithXFlag) {
        dum = (vx[isp][i]*vx[isp][i] + vy[isp][i]*vy[isp][i]
            +vz[isp][i]*vz[isp][i] - emin[isp])/de[isp];
        s = dum;
        if (s<nbin[isp]-1 && dum>=0) {
            dum -= s;
            fe[isp][s] += (!s) ? 2*(1-dum) : 1-dum;
            fe[isp][s+1] += (s==nbin[isp]-2) ? 2*dum : dum;
        }

        dum = -atan(sqrt(vy[isp][i]*vy[isp][i]+vz[isp][i]*vz[isp][i])
            /vx[isp][i])/dtheta[isp];
        s = dum;
        dum -= s;
        ftheta[isp][s] += (!s) ? 2*(1-dum) : 1-dum;
        ftheta[isp][s+1] += (s==nbin[isp]-2) ? 2*dum : dum;
    }
    x[isp][i] = x[isp][nnp];
    vx[isp][i] = vx[isp][nnp];

```

```

vy[isp][i] = vy[isp][nnp];
vz[isp][i] = vz[isp][nnp];
nnp--;
jwall[isp] += jnorm[isp];
if (secondary) {
  if (frand() < seec[isp]) {
    secountl++;
    jwall[seesp] -= jnorm[seesp];
  }
}
}
else {
  /***** MID system diagnostics *****/
  if(theRunWithXFlag) {
    if (xs_mid[isp] <= x[isp][i] && x[isp][i] <= xf_mid[isp]) {
      s = (vx[isp][i]*vx[isp][i] + vy[isp][i]*vy[isp][i]
          +vz[isp][i]*vz[isp][i] - emin_mid[isp])/de_mid[isp];

      if (0 <= s && s< nbin_mid[isp]) {
        fe_mid[isp][s] += 1;
        sp_fe[isp][s] += 1;
      }
    }
  }
  i++;
}
} while (i <= nnp);
np[isp] = nnp + 1;
}

/*****
/* INJECT new particles at walls, one species at a time */

```

```

if (inject[isp] || nreflux[isp]) {
  for(k=0; k<2; k++) {
    extra[isp][k] += enter[isp][k];
    if (enter[isp][k])
      del_t = 1/enter[isp][k];
    if (reflux && k == 1) {
      extra[isp][k] += nreflux[isp];
      if ((enter[isp][k]+nreflux[isp])!=0.0)
        del_t = 1/(enter[isp][k] + nreflux[isp]);
    }
    while (extra[isp][k] >= 1.0) {
      extra[isp][k] -= 1.0;
      ii = np[isp];
      np[isp]++;

      if (ii >= maxnp[isp]) { /* Move array boundaries here */
        printf("ADJUST: too many particles, species %d",isp);
        exit(1);
      }

      /* Choose V's */
      vx[isp][ii] = distribution_flux(k,isp,vxloader[isp][k]);
      vy[isp][ii] = v0y[isp]+vty[isp]*maxwellian(vyloader[isp]);
      vz[isp][ii] = v0z[isp]+vtz[isp]*maxwellian(vzloader[isp]);
      if (k)
        x[isp][ii] = xnc-FLOAT_MIN;
      else
        x[isp][ii] = 0;
      /* Adjust Vx,x for effect of E and B field
      for a partial timestep push*/
      injection_push(isp,ii,extra[isp][k]*del_t);

```

```

/*      injection_push_oldpdp(isp,ii,extra[isp][k]*del_t); */
      if ((x[isp][ii]>=xnc)||(x[isp][ii]<0)){
          np[isp]--;
      }

      if (!k) jwall[isp] -= jnorm[isp];
  }
}
}

if(secondary) {
  i = np[secsp];
  //  np[secsp] += secountl +secountr;

  //  if(np[secsp] >= maxnp[isp])
  //    printf("ADJUST(Secondaries): too many particles. MUST EXIT!");

  for(j=i; j< i+secountl; j++) {
    x[secsp][j]= 0;
    vx[secsp][j]= distribution_flux(0,secsp,vxloader[secsp][0]);
    vy[secsp][j] = v0y[secsp]+vty[isp]*maxwellian(vyloader[secsp]);
    vz[secsp][j] = v0z[secsp]+vtz[isp]*maxwellian(vzloader[secsp]);
    injection_push(secsp,j,frand());
    if (x[secsp][j]<0){
      j--;
      secountl--;
    }
  }
  i += secountl;
  for(j=i; j< i+secountr; j++) {
    x[secsp][j]= xnc-FLOAT_MIN;
    vx[secsp][j]= distribution_flux(1,secsp,vxloader[secsp][1]);
    vy[secsp][j] = v0y[secsp]+vty[isp]*maxwellian(vyloader[secsp]);

```

```

vz[secsp][j] = v0z[secsp]+vtz[isp]*maxwellian(vzloader[secsp]);
injection_push(secsp,j,frand());
if (x[secsp][j]>=xnc){
    j--;
    secountr--;
}
}

np[secsp] += secountr +secountr;

if(np[secsp] >= maxnp[secsp])
    printf("ADJUST(Secondaries): too many particles. MUST EXIT!");
}

if (nm) {
i = np[nmsp];
// if (e[nc] <= 7.5e5) {electron increase is in do-loop, not here.
for (q=i; q< i+secountr; q++) {
    x[nmsp][q] = xnc - FLOAT_MIN;
vx[nmsp][q] = distribution_flux(1,nmsp,vxloader[nmsp][1]);
vy[nmsp][q] = v0y[nmsp]+vty[isp]*maxwellian(vyloader[nmsp]);
    vz[nmsp][q] = v0z[nmsp]+vtz[isp]*maxwellian(vzloader[nmsp]);
injection_push(nmsp,q,frand());
if (x[nmsp][q]>=xnc){
    q--;
    secountr--;
}
}

np[nmsp] += secountr;

if (np[nmsp] >= maxnp[nmsp])
    printf("ADJUST(Secondaries): too many particles. MUST EXIT!");
}

```

```

}

if (nm_den) {
i = np[nm_densp];
//secountr = elect_perdt;
for (q=i; q< i+secountr; q++) {
x[nm_densp][q] = xnc - FLOAT_MIN;
vx[nm_densp][q] = distribution_flux(1,nm_densp,vxloader[nm_densp][1]);
vy[nm_densp][q] = v0y[nm_densp]+vty[isp]*maxwellian(vyloader[nm_densp]);
vz[nm_densp][q] = v0z[nm_densp]+vtz[isp]*maxwellian(vzloader[nm_densp]);
injection_push(nm_densp,q,frand());
if (x[nm_densp][q]>=xnc){
    q--;
    secountr--;
}
}

np[nm_densp] += secountr;

if (np[nm_densp] >= maxnp[nm_densp])
    printf("ADJUST(Secondaries): too many particles. MUST EXIT!");

}

// jwall[isp] /= sp_k[isp]*dt;

/* volume source of ionization */
if (isp==ionsp){
if (psource){
if (t>tstrt)
    ionization(npold-np[ionsp]); /* Create ion/elec pair for each ion lost */
}
if ((vol_source > 0)){

```

```

    this_time += vol_source;
    ionization((int)this_time);
    this_time -= (int)this_time;
}
}

} /* end ADJUST */

/*****/

void sterm(int count)
{
    static float ionization_vel[NSMAX], vgth;
    static int init_flag=1,ionsp;
    int i, ix, j, isp;
    float r;

/*****/

    if (init_flag){
        vgth= sqrt(gtemp/Escale[ionsp]);
        ionsp= ionspecies-1;    /* Fixing the indices into the array of species */
        for (isp=0; isp<nsp; isp++)
            ionization_vel[isp] = sqrt(2*gtemp/Escale[ionsp]);
        init_flag = 0;
    }

    for (isp=0; isp<nsp; isp++)
        if ((np[isp] - count) >= maxnp[isp])
            {
                printf("np[isp] maxnp[isp] %d %d \n ", np[isp], maxnp[isp]);
                puts("source term: too many particles, species ");
                putchar(isp+49);
            }
}

```

```

        exit(1);
    }

if (count < 0) /* add only when there is a loss */
for (j=0; j<abs(count); j++)
{
    r=frand();
    /* Loading the ions (ionsp) randomly in the plasma */
    ix = np[ionsp];
    x[ionsp][ix]= (endpts[1]-endpts[0])*r+endpts[0];

    maxwellv(&vx[ionsp][ix], &vy[ionsp][ix], &vz[ionsp][ix], vgth);

    if(dde)
        for(i=0; i<1; i++)
            x[ionsp][ix] += dde*sin((2*M_PI*x[ionsp][ix]/xnc));

    np[ionsp]++;

    /* Loading the electron (isp=0) at the same position as the ion */
    isp=0;
    ix = np[isp];
    x[isp][ix]= x[ionsp][np[ionsp]-1];
    /* single energy ionization */

    maxwellv(&vx[ionsp][ix], &vy[ionsp][ix], &vz[ionsp][ix], vgth);

    np[isp]++;
}
} /* end STERM */

void ionization(int count)
{

```

```

static float ionization_vel[NSMAX], vgth;
static int init_flag=1,ionsp;
int i, ix, j, isp;
float theta, phi, r;
float sintheta, cosphi, costheta, sinphi;

/*****

if (init_flag){
    ionsp = ionspecies-1; /* Fixing the indices into the array of species */
    if (ionsp<0){
        puts("photo ionization: must have ion species");
        exit(1);
    }
    vgth= sqrt(gtemp/Escale[ionsp]);
    for (isp=0; isp<nsp; isp++)
        ionization_vel[isp] = m[0]*sqrt(ionization_energy/Escale[isp])/m[isp];
    init_flag = 0;
}

for (isp=0; isp<nsp; isp++)
    if ((np[isp] + count) >= maxnp[isp])
        {
            printf("np[isp] maxnp[isp] %d %d \n ", np[isp], maxnp[isp]);
            puts("photo ionization: too many particles, species ");
            putchar(isp+49);
            exit(1);
        }

if (count > 0)
    for (j=0; j<count; j++)
        {

```

```

r=frand();
/* Loading the ions (ionsp=ionspecies-1) randomly in the plasma */
ix = np[ionsp];
x[ionsp][ix]= (endpts[1]-endpts[0])*r+endpts[0];

/* single energy ionization with a background gas temperature*/

maxwellv(&vx[ionsp][ix], &vy[ionsp][ix], &vz[ionsp][ix], vgth);
phi =2*M_PI*frand();
cosphi = cos(phi);
sinphi = sin(phi);
costheta = 1-2*frand();
sintheta = sqrt(1-costheta*costheta);
vx[ionsp][ix] += ionization_vel[ionsp]*sintheta*cosphi;
vy[ionsp][ix] += ionization_vel[ionsp]*sintheta*sinphi;
vz[ionsp][ix] += ionization_vel[ionsp]*costheta;

if(dde)
  for(i=0; i<1; i++)
    x[ionsp][ix] += dde*sin((2*M_PI*x[ionsp][ix]/xnc));

np[ionsp]++;

/* Loading the electrons (isp=0) randomly in the plasma */
isp=0;
ix = np[isp];
x[isp][ix]= x[ionsp][np[ionsp]-1];
/* single energy ionization */

//                                theta += M_PI; //con mom
//                                costheta *=-1;

sintheta *=-1;
vx[isp][ix] = ionization_vel[isp]*sintheta*cosphi;

```

```

        vy[isp][ix] = ionization_vel[isp]*sintheta*sinphi;
        vz[isp][ix] = ionization_vel[isp]*costheta;

        np[isp]++;
    }

} /* end ionization */

/*****

void injection_push(int isp, int i, float del_t)
{
    int j;
    float vxinit, vyinit, vzinit, xinit, vxtemp, vytemp, vztemp, xtemp;
    float vxhalf, vyhalf, vzhalf;
    float k, a0;
    float sin2fW;

    float s;

    float deltaA, ep, f, fW, A1, A2, A3, A4;

    k = sp_k[isp];
    vxtemp = vxinit = vxhalf = vx[isp][i];
    vytemp = vyinit = vyhalf = vy[isp][i];
    vztemp = vzinit = vzhalf = vz[isp][i];
    xtemp = xinit = x[isp][i];

    j = xinit;
    s = xinit - j;

    /* a is for normalized for half a time step */
    /*

```

```

if (s){
a0 =a[j] + s*(a[j+1] - a[j]);
deltaA = aold[j] + s*(aold[j+1] - aold[j])- a[j] + s*(a[j+1] - a[j]);
ep= rho[j]+s*(rho[j+1] - rho[j]);
}
else {
a0 = a[j];
*/

/*Assume that the particle is injected from the
right or left side of the simulation */

a0=a[j];
if (j<1){
deltaA = a_scale[isp]*eold[0]-a0;
ep = a_scale[isp]*rho[0]*dx/epsilon;
}
else{
deltaA = a_scale[isp]*eold[1]-a0;
ep = a_scale[isp]*rho[nc]*dx/epsilon;
}

if (b>0){
/*position push*/
a0*=2;
ep*=2;
deltaA*=2;
f = del_t;
fW=f*W[isp];
A1=f*(3*a0+deltaA*(2*f-3)+ep*vxinit*f)*onesixth;
A2=3*sin(fW)+fW*cos(fW);
A3=3*cos(fW)-fW*sin(fW);

```

```

x[isp][i] +=f*(vxinit+A1+twothirds*sin(fW)*sin_psi*(A2*(vzinit*cos_psi-
(vxinit+0.5*A1)*sin_psi)+A3*vyinit));

```

```

/*velocity push*/

```

```

f = del_t-.5;

```

```

fW=f*W[isp];

```

```

A1=(W[isp]*sin4W[isp]+12*sqr(sin(2*fW)))*one12;

```

```

A2=(W[isp]*sin22W[isp]-3*sin(4*fW))*onethird;

```

```

A3=0.25*(4+ep*sqr(f));

```

```

A4=0.25*f*(2*a0+deltaA*(f-1));

```

```

sin2fW=sin(2*fW);

```

```

vx[isp][i] += a0*f+one24*(deltaA*(12*f*(f-1)-1)-

```

```

2*sqr(sin_psi)*(a0*W[isp]*sin4W[isp]+24*A4*sqr(sin2fW))+

```

```

vxinit*(ep*(1+12*sqr(f))-

```

```

4*sqr(sin_psi)*(12*A1+3*ep*sqr(f*sin2fW)))+

```

```

sin_psi*(-vyinit*A2+

```

```

vzinit*2.0*cos_psi*A2);

```

```

vy[isp][i] += sin_psi*(-onesixth*W[isp]*a0*cos22W[isp]-A4*sin(4*fW)+

```

```

vxinit*(onethird*W[isp]*sin22W[isp]-A3*sin(4*fW)))

```

```

-2.0*vyinit*A1-vzinit*A2*cos_psi;

```

```

vz[isp][i]

```

```

+=

```

```

one12*cos_psi*(sin_psi*(a0*W[isp]*sin4W[isp]+24*sqr(sin2fW)*A4+

```

```

2*vxinit*(W[isp]*sin4W[isp]+12*sqr(sin2fW)*A3))+

```

```

12*vyinit*A2-24*vzinit*cos_psi*A1);

```

```

}

```

```

else{

```

```

/*position push*/

```

```

f = del_t;

```

```

A1=f*(3*a0+deltaA*(2*f-3)+ep*vxinit*f)*onesixth;

```

```

x[isp][i] +=f*(vxinit+A1);

```

```

/*velocity push*/
f = del_t-.5;
vx[isp][i] += a0*f+one24*(deltaA*(12*f*(f-1)-1)+
                vxinit*ep*(1+12*sqr(f)));
}
}

void injection_push_oldpdp(int isp, int i, float del_t)
{
int j;
float temp_t;
float vxinit, vyinit, vzinit, xinit, vxtemp, vytemp, vztemp, xtemp;
float vxhalf, vyhalf, vzhalf;
float k, s, a0;
float ax;

k = sp_k[isp];
vxtemp = vxinit = vxhalf = vx[isp][i];
vytemp = vyinit = vyhalf = vy[isp][i];
vztemp = vzinit = vzhalf = vz[isp][i];
xtemp = xinit = x[isp][i];

j = xinit;
s = xinit - j;

if (s)
    a0 = a[j] + s*(a[j+1] - a[j]);
else a0 = a[j];
if (b>0){
temp_t = del_t-.5; /* half step already normalized in a array, tz, and tx.*/
/****** mag acc *****/

ax = 2*a0;

```

```

vx[isp][i] += temp_t*ax;

/***** Update Position *****/

x[isp][i] += del_t*k*vxinit;
}
}

void injection_push_FTSP(int isp, int i, float del_t)
{
int j;
float temp_t;
float vxinit, vyinit, vzinit, xinit, vxtemp, vytemp, vztemp, xtemp;
float vxhalf, vyhalf, vzhalf;
float k, s, atemp=0, a0;

float tx,tz,sx,sz;
float t;

k = sp_k[isp];
vxtemp = vxinit = vxhalf = vx[isp][i];
vytemp = vyinit = vyhalf = vy[isp][i];
vztemp = vzinit = vzhalf = vz[isp][i];
xtemp = xinit = x[isp][i];

j = xinit;
s = xinit - j;

if (s)
a0 = a[j] + s*(a[j+1] - a[j]);
else a0 = a[j];

```

```

if (b>0){
  temp_t = del_t-.5;
  atemp = a[j] + s*(a[j+1] - a[j]);

  vx[isp][i] += temp_t*a0;

  t= tan(.5*b*qm[isp]*dt*temp_t*sp_k[isp]);
  s= 2*t/(1+t*t);

  tx= t*cosd(psi);
  tz= t*sind(psi);
  sx= s*cosd(psi);
  sz= s*sind(psi);

  /***** Advance velocity *****/
  /***** Boris rotation *****/
  vxhalf= vx[isp][i] +tz*vyinit;
  vyhalf= vyinit -tz*vx[isp][i] +tx*vzinit;
  vzhalf= vzinit -tx*vyinit;

  vx[isp][i] += sz*vyhalf;
  vy[isp][i] += -sz*vxhalf +sx*vzhalf;
  vz[isp][i] += -sx*vyhalf;

  vx[isp][i] += temp_t*a0;

  /***** Advance position *****/

  temp_t = del_t/2;
  atemp = a[j] + s*(a[j+1] - a[j]);

  vxtemp = vxinit;
  vxtemp += temp_t*a0;

```

```

t= tan(.5*b*qm[isp]*dt*temp_t*sp_k[isp]);
s= 2*t/(1+t*t);

tx= t*cosd(psi);
tz= t*sind(psi);
sx= s*cosd(psi);
sz= s*sind(psi);

/***** Boris rotation *****/
vyhalf= vyinit -tz*vxtmp +tx*vzinit;
vxtmp += sz*vyhalf;

vxtmp += temp_t*a0;

x[isp][i] += vxtmp*del_t;

}
}

void injection_push_MBP(int isp, int i, float del_t)
{
int j;
float vxinit, vyinit, vzinit, xinit, vxtmp, vytemp, vztemp, xtemp;
float vxhalf, vyhalf, vzhalf;
float k, a0;
float sin2fW;

float s;

float dx;

float f, fW, A1, A2, A3, A4;

```

```

k = sp_k[isp];
vxtemp = vxinit = vxhalf = vx[isp][i];
vytemp = vyinit = vyhalf = vy[isp][i];
vztemp = vzinit = vzhalf = vz[isp][i];
xtemp = xinit = x[isp][i];

j = xinit;
s = xinit - j;

/*Assume that the particle is injected from
the right or left side of the simulation */

a0=a[j];

if (b>0){
/*position push*/
a0*=2;
f = del_t;
fW= f*W[isp];
A1=f*3*a0*onesixth;
A2=3*sin(fW)+fW*cos(fW);
A3=3*cos(fW)-fW*sin(fW);
dx      =      f*(vxinit+A1+twothirds*sin(fW)*sin_psi*(A2*(vzinit*cos_psi-
(vxinit+0.5*A1)*sin_psi)+A3*vyinit));
x[isp][i]      +=f*(vxinit+A1+twothirds*sin(fW)*sin_psi*(A2*(vzinit*cos_psi-
(vxinit+0.5*A1)*sin_psi)+A3*vyinit));

/*velocity push*/
f = del_t*.5;
fW=f*W[isp];
A1=(W[isp]*sin4W[isp]+12*sqr(sin(2*fW)))*one12;
A2=(W[isp]*sin22W[isp]-3*sin(4*fW))*onethird;

```

```

A3=0.25*4;
A4=0.25*f*(2*a0);
sin2fW=sin(2*fW);
vx[isp][i] += a0*f+one24*(-
2*sqr(sin_psi)*(a0*W[isp]*sin4W[isp]+24*A4*sqr(sin2fW))+
vxinit*(-4*sqr(sin_psi)*12*A1))+
sin_psi*(-vyinit*A2+
vzinit*2.0*cos_psi*A2);
vy[isp][i] += sin_psi*(-onesixth*W[isp]*a0*cos22W[isp]-A4*sin(4*fW)+
vxinit*(onethird*W[isp]*sin22W[isp]-A3*sin(4*fW)))
-2.0*vyinit*A1-vzinit*A2*cos_psi;
vz[isp][i] +=
one12*cos_psi*(sin_psi*(a0*W[isp]*sin4W[isp]+24*sqr(sin2fW)*A4+
2*vxinit*(W[isp]*sin4W[isp]+12*sqr(sin2fW)*A3))+
12*vyinit*A2-24*vzinit*cos_psi*A1);
}
}

```

```

void injection_push_FG(int isp, int i, float del_t)
{
int j;
float vxinit, vyinit, vzinit, xinit, vxtemp, vytemp, vztemp, xtemp;
float vxhalf, vyhalf, vzhalf;
float k, a0;
float sin2fW;

float s;

float ep, f, fW, A1, A2, A3, A4;

```

```

k = sp_k[isp];
vxtemp = vxinit = vxhalf = vx[isp][i];
vytemp = vyinit = vyhalf = vy[isp][i];
vztemp = vzinit = vzhalf = vz[isp][i];
xtemp = xinit = x[isp][i];

j = xinit;
s = xinit - j;

/* Assume that the particle is injected from
the right or left side of the simulation */

a0=a[j];
if (j<1){
    ep = a_scale[isp]*rho[0]/epsilon*dx;
}
else{
    ep = a_scale[isp]*rho[nc]/epsilon;
}

if (b>0){
    /*position push*/
    /* a is for normalized for half a time step  a0*=2; */

    ep*=2;
    f = del_t;
    fW= f*W[isp];
    A1=f*(3*a0+ep*vxinit*f)*onesixth;
    A2=3*sin(fW)+fW*cos(fW);
    A3=3*cos(fW)-fW*sin(fW);
    x[isp][i] +=f*(vxinit+A1+twothirds*sin(fW)*sin_psi*(A2*(vzinit*cos_psi-
(vxinit+0.5*A1)*sin_psi)+A3*vyinit));

```

```

/*velocity push*/
f = del_t-.5;
fW=f*W[isp];
A1=(W[isp]*sin4W[isp]+12*sqr(sin(2*fW)))*one12;
A2=(W[isp]*sin22W[isp]-3*sin(4*fW))*onethird;
A3=0.25*(4+ep*sqr(f));
A4=0.5*f*a0;
sin2fW=sin(2*fW);
vx[isp][i] += a0*f+one24*(-
2*sqr(sin_psi)*(a0*W[isp]*sin4W[isp]+24*A4*sqr(sin2fW))+
vxinit*(ep*(1+12*sqr(f))-
4*sqr(sin_psi)*(12*A1+3*ep*sqr(f*sin2fW))))+
sin_psi*(-vyinit*A2+
vzinit*2.0*cos_psi*A2);
vy[isp][i] += sin_psi*(-onesixth*W[isp]*a0*cos22W[isp]-A4*sin(4*fW)+
vxinit*(onethird*W[isp]*sin22W[isp]-A3*sin(4*fW)))
-2.0*vyinit*A1-vzinit*A2*cos_psi;
vz[isp][i] +=
one12*cos_psi*(sin_psi*(a0*W[isp]*sin4W[isp]+24*sqr(sin2fW)*A4+
2*vxinit*(W[isp]*sin4W[isp]+12*sqr(sin2fW)*A3))+
12*vyinit*A2-24*vzinit*cos_psi*A1);
}
}

```

### A.3 XPDP1 Source padjus.c in Modified Form

```
#include "pdp1.h"
```

```
#include "xgrafx.h"
```

```
/******
```

```

/* Routine to adjust (initialize, re-pack and inject) particles */
/* to the desired boundary conditions */

void injection_push(int species, int particle, float part_time);
void injection_push_oldpdp(int species, int particle, float part_time);
void injection_push_FTSBP(int species, int particle, float part_time);
void injection_push_MBP(int species, int particle, float part_time);
void injection_push_FG(int species, int particle, float part_time);

void sterm(int number);
void ionization(int number);

void adjust(int isp)
{
    static int ionsp, npold;
    static int secsp, nmosp, nm_densp, init_flag=1;
    static float extra[NSMAX][2];
    static float this_time;

    register int i, ii, j, k, q;
    int nnp, secountl=0, secountr=0;
    // float secountl=0, secountr=0;
    int nreflux[NSMAX], s;
    float dum, del_t=0;

    /* INITIALIZE array for computing positions of injected particles */
    if (init_flag) {

        ionsp = ionspecies-1;
        secsp = secondary -1;
        nmosp = nm -1;
        nm_densp = nm_den -1;

```

```

/* "enter" is now the no. of particles injected each "dt" */
for (i=0; i<nsp; i++) {
  if (fabs(enter[i][0]) > 0.) extra[i][0] = 0.5123123;
  else extra[i][0] = 0.;
  if (fabs(enter[i][1]) > 0.) extra[i][1] = 0.5123123;
  else extra[i][1] = 0.;
}
init_flag = 0;
}

if (psource && (isp == ionsp))
  npold = np[ionsp]; /* Save the number of ions before adjust */

if (isp==0) // secondaries add to jwall[secsp] not jwall[isp]
  for (i=0; i<nsp; i++)
    jwall[i]=0;

if(secondary) secountr = secountr = 0;
nreflux[isp]= 0; /* nreflux[isp] equals zero */

if (np[isp] > 0) {
  nnp = np[isp] -1;
  i = 0;

  /* eliminate "outsiders", allow for secondary electron emission, */
  /* and if it left thru LH plate, ADD charge there to sigma */
  /* (plate surface density). */

  /* note: the system starts at 0 (includes 0) and end before xnc */
  /******* DOES NOT INCLUDE xnc *****/
  /***/

```

```

do {
  if (x[isp][i] >= xnc) {
    x[isp][i] = x[isp][nnp];
    vx[isp][i] = vx[isp][nnp];
    vy[isp][i] = vy[isp][nnp];
    vz[isp][i] = vz[isp][nnp];
    nnp--;
    if(reflux) nreflux[isp]++;
    else if(secondary) {
      if (frand() < seec[isp]){
        secountr++;
      }
    }
    if (nm) {
      if (phi[0] <= 7.5){
        if (frand() < nmeec[isp]) {
          secountr=secountr+1;
        }
      }

      /* if (e[nc] > 7.5e5) { */
      else
        if (frand() < nmeec[isp]){
          secountr=secountr+2;
        }
    }

    if (nm_den) {
      if (int_spc < 1) {
        if (phi[0] <= 8.5){
          if(frand() < nmeec[isp]){

```

```

        secountr = secountr+1;
    }
}
else
    if (frand() < nmeec[isp]){
        secountr = secountr+2;
    }
}
else

if (int_spc==1) {
    if (phi[0] <=5.0){
        if (frand() < nmeec[isp]) {
            secountr =secountr+1;
        }
    }
}
else
    if (frand() < nmeec[isp]) {
        secountr=secountr+2;

    }
}
else
if (int_spc==2){
    if (phi[0] <= 6.5){
        if (frand() < nmeec[isp]){
            secountr = secountr+1;
        }
    }
}
else
    if (frand() <nmeec[isp]){
        secountr = secountr+2;
    }
}

```

```

    }
else
    if (int_spc==3){
        if(phi[0] <= 7.5){
            if (frand() < nmeec[isp]){
                secountr = secountr+1;
            }
        }
        else
            if (frand() < nmeec[isp]){
                secountr = secountr+2;
            }
    }
}

else if (x[isp][i] < 0) {
    /******* LHS wall diagnostics *****/
    if(theRunWithXFlag) {
        dum = (vx[isp][i]*vx[isp][i] + vy[isp][i]*vy[isp][i]
            +vz[isp][i]*vz[isp][i] - emin[isp])/de[isp];
        s = dum;
        if (s<nbin[isp]-1 && dum>=0) {
            dum -= s;
            fe[isp][s] += (!s) ? 2*(1-dum) : 1-dum;
            fe[isp][s+1] += (s==nbin[isp]-2) ? 2*dum : dum;
        }

        dum = -atan(sqrt(vy[isp][i]*vy[isp][i]+vz[isp][i]*vz[isp][i])
            /vx[isp][i])/dtheta[isp];
        s = dum;
        dum -= s;
        ftheta[isp][s] += (!s) ? 2*(1-dum) : 1-dum;
        ftheta[isp][s+1] += (s==nbin[isp]-2) ? 2*dum : dum;
    }
}

```

```

    }
    x[isp][i] = x[isp][nnp];
    vx[isp][i] = vx[isp][nnp];
    vy[isp][i] = vy[isp][nnp];
    vz[isp][i] = vz[isp][nnp];
    nnp--;
    jwall[isp] += jnorm[isp];
    if (secondary) {
        if (frand() < seec[isp]) {
            secountl++;
            jwall[secsp] -= jnorm[secsp];
        }
    }
}

else {
    /***** MID system diagnostics *****/
    if(theRunWithXFlag) {
        if (xs_mid[isp] <= x[isp][i] && x[isp][i] <= xf_mid[isp]) {
            s = (vx[isp][i]*vx[isp][i] + vy[isp][i]*vy[isp][i]
                +vz[isp][i]*vz[isp][i] - emin_mid[isp])/de_mid[isp];

            if (0 <= s && s < nbin_mid[isp]) {
                fe_mid[isp][s] += 1;
                sp_fe[isp][s] += 1;
            }
        }
    }
    i++;
}
} while (i <= nnp);
np[isp] = nnp + 1;
}

```

```

/*****
/* INJECT new particles at walls, one species at a time */

if (inject[isp] || nreflux[isp]) {
  for(k=0; k<2; k++) {
    extra[isp][k] += enter[isp][k];
    if (enter[isp][k])
      del_t = 1/enter[isp][k];
    if (reflux && k == 1) {
      extra[isp][k] += nreflux[isp];
      if ((enter[isp][k]+nreflux[isp])!=0.0)
        del_t = 1/(enter[isp][k] + nreflux[isp]);
    }
    while (extra[isp][k] >= 1.0) {
      extra[isp][k] -= 1.0;
      ii = np[isp];
      np[isp]++;

      if (ii >= maxnp[isp]) { /* Move array boundaries here */
        printf("ADJUST: too many particles, species %d",isp);
        exit(1);
      }

      /* Choose V's */
      vx[isp][ii] = distribution_flux(k,isp,vxloader[isp][k]);
      vy[isp][ii] = v0y[isp]+vty[isp]*maxwellian(vyloader[isp]);
      vz[isp][ii] = v0z[isp]+vtz[isp]*maxwellian(vzloader[isp]);
      if (k)
        x[isp][ii] = xnc-FLOAT_MIN;
      else
        x[isp][ii] = 0;
    }
  }
}

```

```

/* Adjust Vx,x for effect of E and B field
   for a partial timestep push*/
      injection_push(isp,ii,extra[isp][k]*del_t);
/* injection_push_oldpdp(isp,ii,extra[isp][k]*del_t); */
if ((x[isp][ii]>=xnc)||(x[isp][ii]<0)){
    np[isp]--;
}

if (!k) jwall[isp] -= jnorm[isp];
}
}
}

if(secondary) {
    i = np[secsp];
    // np[secsp] += secountl +secountr;

    // if(np[secsp] >= maxnp[isp])
    // printf("ADJUST(Secondaries): too many particles. MUST EXIT!");

for(j=i; j< i+secountl; j++) {
    x[secsp][j]= 0;
    vx[secsp][j]= distribution_flux(0,secsp,vxloader[secsp][0]);
    vy[secsp][j] = v0y[secsp]+vty[isp]*maxwellian(vyloader[secsp]);
    vz[secsp][j] = v0z[secsp]+vtz[isp]*maxwellian(vzloader[secsp]);
    injection_push(secsp,j,frand());
    if (x[secsp][j]<0){
        j--;
        secountl--;
    }
}
}

i += secountl;
for(j=i; j< i+secountr; j++) {

```

```

x[secsp][j]= xnc-FLOAT_MIN;
vx[secsp][j]= distribution_flux(1,secsp,vxloader[secsp][1]);
vy[secsp][j] = v0y[secsp]+vty[isp]*maxwellian(vyloader[secsp]);
vz[secsp][j] = v0z[secsp]+vtz[isp]*maxwellian(vzloader[secsp]);
injection_push(secsp,j,frand());
if (x[secsp][j]>=xnc){
    j--;
    secountr--;
}
}

np[secsp] += secountr;

if(np[secsp] >= maxnp[secsp])
    printf("ADJUST(Secondaries): too many particles. MUST EXIT!");
}

if (nm) {
i = np[nmsp];
// if (e[nc] <= 7.5e5) {electron increase is in do-loop, not here.
for (q=i; q< i+secountr; q++) {
    x[nmsp][q] = xnc - FLOAT_MIN;
vx[nmsp][q] = distribution_flux(1,nmsp,vxloader[nmsp][1]);
vy[nmsp][q] = v0y[nmsp]+vty[isp]*maxwellian(vyloader[nmsp]);
vz[nmsp][q] = v0z[nmsp]+vtz[isp]*maxwellian(vzloader[nmsp]);
injection_push(nmsp,q,frand());
if (x[nmsp][q]>=xnc){
    q--;
    secountr--;
}
}

np[nmsp] += secountr;

```

```

        if (np[nmsp] >= maxnp[nmsp])
            printf("ADJUST(Secondaries): too many particles. MUST EXIT!");
    }

    if (nm_den) {
        i = np[nm_densp];
        //secountr = elect_perdt;
        for (q=i; q< i+secountr; q++) {
            x[nm_densp][q] = xnc - FLOAT_MIN;
            vx[nm_densp][q] = distribution_flux(1,nm_densp,vxloader[nm_densp][1]);
            vy[nm_densp][q] = v0y[nm_densp]+vty[isp]*maxwellian(vyloader[nm_densp]);
            vz[nm_densp][q] = v0z[nm_densp]+vtz[isp]*maxwellian(vzloader[nm_densp]);
            injection_push(nm_densp,q,frand());
            if (x[nm_densp][q]>=xnc){
                q--;
                secountr--;
            }
        }

        np[nm_densp] += secountr;

        if (np[nm_densp] >= maxnp[nm_densp])
            printf("ADJUST(Secondaries): too many particles. MUST EXIT!");

    }

// jwall[isp] /= sp_k[isp]*dt;

/* volume source of ionization */
if (isp==ionsp){
    if (psource){
        if (t>tstrt)

```

```

        ionization(npold-np[ionsp]); /* Create ion/elec pair for each ion lost ?*/
    }
    if ((vol_source > 0)){
        this_time += vol_source;
        ionization((int)this_time);
        this_time -= (int)this_time;
    }
}

} /* end ADJUST */

/*****

void sterm(int count)
{
    static float ionization_vel[NSMAX], vgth;
    static int init_flag=1,ionsp;
    int i, ix, j, isp;
    float r;

    /*****

    if (init_flag){
        vgth= sqrt(gtemp/Escale[ionsp]);
        ionsp= ionspecies-1;      /* Fixing the indices into the array of species */
        for (isp=0; isp<nsp; isp++)
            ionization_vel[isp] = sqrt(2*gtemp/Escale[ionsp]);
        init_flag = 0;
    }

    for (isp=0; isp<nsp; isp++)
        if ((np[isp] - count) >= maxnp[isp])
            {

```

```

printf("np[isp] maxnp[isp] %d %d \n ", np[isp], maxnp[isp]);
puts("source term: too many particles, species ");
putchar(isp+49);
exit(1);
}

if (count < 0) /* add only when there is a loss */
for (j=0; j<abs(count); j++)
{
r=frand();
/* Loading the ions (ionsp) randomly in the plasma */
ix = np[ionsp];
x[ionsp][ix]= (endpts[1]-endpts[0])*r+endpts[0];

maxwellv(&vx[ionsp][ix], &vy[ionsp][ix], &vz[ionsp][ix], vgth);

if(dde)
for(i=0; i<1; i++)
x[ionsp][ix] += dde*sin((2*M_PI*x[ionsp][ix]/xnc));

np[ionsp]++;

/* Loading the electron (isp=0) at the same position as the ion */
isp=0;
ix = np[isp];
x[isp][ix]= x[ionsp][np[ionsp]-1];
/* single energy ionization */

maxwellv(&vx[ionsp][ix], &vy[ionsp][ix], &vz[ionsp][ix], vgth);

np[isp]++;
}
} /* end STERM */

```

```

void ionization(int count)
{
    static float ionization_vel[NMAX], vgth;
    static int init_flag=1,ionsp;
    int i, ix, j, isp;
    float theta, phi, r;
    float sintheta, cosphi, costheta, sinphi;

    /*****

if (init_flag){
    ionsp = ionspecies-1; /* Fixing the indices into the array of species */
    if (ionsp<0){
        puts("photo ionization: must have ion species");
        exit(1);
    }
    vgth= sqrt(gtemp/Escale[ionsp]);
    for (isp=0; isp<nsp; isp++)
        ionization_vel[isp] = m[0]*sqrt(ionization_energy/Escale[isp])/m[isp];
    init_flag = 0;
}

for (isp=0; isp<nsp; isp++)
    if ((np[isp] + count) >= maxnp[isp])
        {
            printf("np[isp] maxnp[isp] %d %d \n ", np[isp], maxnp[isp]);
            puts("photo ionization: too many particles, species ");
            putchar(isp+49);
            exit(1);
        }

```

```

if (count > 0)
  for (j=0; j<count; j++)
  {
    r=frand();
    /* Loading the ions (ionsp=ionspecies-1) randomly in the plasma */
    ix = np[ionsp];
    x[ionsp][ix]= (endpts[1]-endpts[0])*r+endpts[0];

    /* single energy ionization with a background gas temperature*/

    maxwellv(&vx[ionsp][ix], &vy[ionsp][ix], &vz[ionsp][ix], vgth);
    phi =2*M_PI*frand();
    cosphi = cos(phi);
    sinphi = sin(phi);
    costheta = 1-2*frand();
    sintheta = sqrt(1-costheta*costheta);
    vx[ionsp][ix] += ionization_vel[ionsp]*sintheta*cosphi;
    vy[ionsp][ix] += ionization_vel[ionsp]*sintheta*sinphi;
    vz[ionsp][ix] += ionization_vel[ionsp]*costheta;

    if(dde)
      for(i=0; i<1; i++)
        x[ionsp][ix] += dde*sin((2*M_PI*x[ionsp][ix]/xnc));

    np[ionsp]++;

    /* Loading the electrons (isp=0) randomly in the plasma */
    isp=0;
    ix = np[isp];
    x[isp][ix]= x[ionsp][np[ionsp]-1];
    /* single energy ionization */

    //
    theta += M_PI; //con mom

```

```

costheta *=-1;
  sintheta *=-1;
  vx[isp][ix] = ionization_vel[isp]*sintheta*cosphi;
  vy[isp][ix] = ionization_vel[isp]*sintheta*sinphi;
  vz[isp][ix] = ionization_vel[isp]*costheta;

  np[isp]++;
}

} /* end ionization */

/*****

void injection_push(int isp, int i, float del_t)
{
  int j;
  float vxinit, vyinit, vzinit, xinit, vxtemp, vytemp, vztemp, xtemp;
  float vxhalf, vyhalf, vzhalf;
  float k, a0;
  float sin2fW;

  float s;

  float deltaA, ep, f, fW, A1, A2, A3, A4;

  k = sp_k[isp];
  vxtemp = vxinit = vxhalf = vx[isp][i];
  vytemp = vyinit = vyhalf = vy[isp][i];
  vztemp = vzinit = vzhalf = vz[isp][i];
  xtemp = xinit = x[isp][i];

  j = xinit;
  s = xinit - j;

```

```

/* a is for normalized for half a time step */
/*
  if (s){
    a0 =a[j] + s*(a[j+1] - a[j]);
    deltaA = aold[j] + s*(aold[j+1] - aold[j]) - a[j] + s*(a[j+1] - a[j]);
    ep= rho[j]+s*(rho[j+1] - rho[j]);
  }
  else {
    a0 = a[j];
  }
*/

/*Assume that the particle is injected from the
right or left side of the simulation */

a0=a[j];
if (j<1){
  deltaA = a_scale[isp]*eold[0]-a0;
  ep = a_scale[isp]*rho[0]*dx/epsilon;
}
else{
  deltaA = a_scale[isp]*eold[1]-a0;
  ep = a_scale[isp]*rho[nc]*dx/epsilon;
}

if (b>0){
  /*position push*/
  a0*=2;
  ep*=2;
  deltaA*=2;
  f = del_t;
  fW=f*W[isp];

```

```

A1=f*(3*a0+deltaA*(2*f-3)+ep*vxinit*f)*onesixth;
A2=3*sin(fW)+fW*cos(fW);
A3=3*cos(fW)-fW*sin(fW);
x[isp][i]+=f*(vxinit+A1+twothirds*sin(fW)*sin_psi*(A2*(vzinit*cos_psi-
(vxinit+0.5*A1)*sin_psi)+A3*vyinit));

/*velocity push*/
f = del_t-.5;
fW=f*W[isp];
A1=(W[isp]*sin4W[isp]+12*sqr(sin(2*fW)))*one12;
A2=(W[isp]*sin22W[isp]-3*sin(4*fW))*onethird;
A3=0.25*(4+ep*sqr(f));
A4=0.25*f*(2*a0+deltaA*(f-1));
sin2fW=sin(2*fW);
vx[isp][i] += a0*f+one24*(deltaA*(12*f*(f-1)-1)-
2*sqr(sin_psi)*(a0*W[isp]*sin4W[isp]+24*A4*sqr(sin2fW))+
vxinit*(ep*(1+12*sqr(f))-
4*sqr(sin_psi)*(12*A1+3*ep*sqr(f*sin2fW))))+
sin_psi*(-vyinit*A2+
vzinit*2.0*cos_psi*A2);
vy[isp][i] += sin_psi*(-onesixth*W[isp]*a0*cos22W[isp]-A4*sin(4*fW)+
vxinit*(onethird*W[isp]*sin22W[isp]-A3*sin(4*fW)))
-2.0*vyinit*A1-vzinit*A2*cos_psi;
vz[isp][i]+=
one12*cos_psi*(sin_psi*(a0*W[isp]*sin4W[isp]+24*sqr(sin2fW)*A4+
2*vxinit*(W[isp]*sin4W[isp]+12*sqr(sin2fW)*A3))+
12*vyinit*A2-24*vzinit*cos_psi*A1);
}
else{
/*position push*/
f = del_t;

```

```

A1=f*(3*a0+deltaA*(2*f-3)+ep*vxinit*f)*onesixth;
x[isp][i] +=f*(vxinit+A1);

/*velocity push*/
f = del_t-.5;
vx[isp][i] += a0*f+one24*(deltaA*(12*f*(f-1)-1)+
                vxinit*ep*(1+12*sqr(f)));
}
}

void injection_push_oldpdp(int isp, int i, float del_t)
{
int j;
float temp_t;
float vxinit, vyinit, vzinit, xinit, vxtemp, vytemp, vztemp, xtemp;
float vxhalf, vyhalf, vzhalf;
float k, s, a0;
float ax;

k = sp_k[isp];
vxtemp = vxinit = vxhalf = vx[isp][i];
vytemp = vyinit = vyhalf = vy[isp][i];
vztemp = vzinit = vzhalf = vz[isp][i];
xtemp = xinit = x[isp][i];

j = xinit;
s = xinit - j;

if (s)
    a0 = a[j] + s*(a[j+1] - a[j]);
else a0 = a[j];
if (b>0){
    temp_t = del_t-.5; /* half step already normalized in a array, tz, and tx.*/

```

```

/***** mag acc *****/

ax = 2*a0;

vx[isp][i] += temp_t*ax;

/***** Update Position *****/

x[isp][i] += del_t*k*vxinit;
}
}

void injection_push_FTSPB(int isp, int i, float del_t)
{
int j;
float temp_t;
float vxinit, vyinit, vzinit, xinit, vxtemp, vytemp, vztemp, xtemp;
float vxhalf, vyhalf, vzhalf;
float k, s, atemp=0, a0;

float tx,tz,sx,sz;
float t;

k = sp_k[isp];
vxtemp = vxinit = vxhalf = vx[isp][i];
vytemp = vyinit = vyhalf = vy[isp][i];
vztemp = vzinit = vzhalf = vz[isp][i];
xtemp = xinit = x[isp][i];

j = xinit;
s = xinit - j;

if (s)

```

```

    a0 = a[j] + s*(a[j+1] - a[j]);
else a0 = a[j];

if (b>0){
    temp_t = del_t-.5;
    atemp = a[j] + s*(a[j+1] - a[j]);

    vx[isp][i] += temp_t*a0;

    t= tan(.5*b*qm[isp]*dt*temp_t*sp_k[isp]);
    s= 2*t/(1+t*t);

    tx= t*cosd(psi);
    tz= t*sind(psi);
    sx= s*cosd(psi);
    sz= s*sind(psi);

    /***** Advance velocity *****/
    /***** Boris rotation *****/
    vxhalf= vx[isp][i] +tz*vyinit;
    vyhalf= vyinit -tz*vx[isp][i] +tx*vzinit;
    vzhalf= vzinit -tx*vyinit;

    vx[isp][i] += sz*vyhalf;
    vy[isp][i] += -sz*vxhalf +sx*vzhalf;
    vz[isp][i] += -sx*vyhalf;

    vx[isp][i] += temp_t*a0;

    /***** Advance position *****/

    temp_t = del_t/2;
    atemp = a[j] + s*(a[j+1] - a[j]);

```

```

vxtemp = vxinit;
vxtemp += temp_t*a0;

t= tan(.5*b*qm[isp]*dt*temp_t*sp_k[isp]);
s= 2*t/(1+t*t);

tx= t*cosd(psi);
tz= t*sind(psi);
sx= s*cosd(psi);
sz= s*sind(psi);

/***** Boris rotation *****/
vyhalf= vyinit -tz*vxtemp +tx*vzinit;
vxtemp += sz*vyhalf;

vxtemp += temp_t*a0;

x[isp][i] += vxtemp*del_t;

}
}

void injection_push_MBP(int isp, int i, float del_t)
{
int j;
float vxinit, vyinit, vzinit, xinit, vxtemp, vytemp, vztemp, xtemp;
float vxhalf, vyhalf, vzhalf;
float k, a0;
float sin2fW;

float s;

```

```

float dx;

float f, fW, A1, A2, A3, A4;

k = sp_k[isp];
vxtemp = vxinit = vxhalf = vx[isp][i];
vytemp = vyinit = vyhalf = vy[isp][i];
vztemp = vzinit = vzhalf = vz[isp][i];
xtemp = xinit = x[isp][i];

j = xinit;
s = xinit - j;

/*Assume that the particle is injected from
the right or left side of the simulation */

a0=a[j];

if (b>0){
    /*position push*/
    a0*=2;
    f = del_t;
    fW= f*W[isp];
    A1=f*3*a0*onesixth;
    A2=3*sin(fW)+fW*cos(fW);
    A3=3*cos(fW)-fW*sin(fW);
    dx      =      f*(vxinit+A1+twothirds*sin(fW)*sin_psi*(A2*(vzinit*cos_psi-
(vxinit+0.5*A1)*sin_psi)+A3*vyinit));
    x[isp][i]      +=f*(vxinit+A1+twothirds*sin(fW)*sin_psi*(A2*(vzinit*cos_psi-
(vxinit+0.5*A1)*sin_psi)+A3*vyinit));

    /*velocity push*/
    f = del_t-.5;

```

```

fW=f*W[isp];
A1=(W[isp]*sin4W[isp]+12*sqr(sin(2*fW)))*one12;
A2=(W[isp]*sin22W[isp]-3*sin(4*fW))*onethird;
A3=0.25*4;
A4=0.25*f*(2*a0);
sin2fW=sin(2*fW);
vx[isp][i]+=a0*f+one24*(-
2*sqr(sin_psi)*(a0*W[isp]*sin4W[isp]+24*A4*sqr(sin2fW))+
vxinit*(-4*sqr(sin_psi)*12*A1))+
sin_psi*(-vyinit*A2+
vzinit*2.0*cos_psi*A2);
vy[isp][i] += sin_psi*(-onesixth*W[isp]*a0*cos22W[isp]-A4*sin(4*fW)+
vxinit*(onethird*W[isp]*sin22W[isp]-A3*sin(4*fW)))
-2.0*vyinit*A1-vzinit*A2*cos_psi;
vz[isp][i] +=
one12*cos_psi*(sin_psi*(a0*W[isp]*sin4W[isp]+24*sqr(sin2fW)*A4+
2*vxinit*(W[isp]*sin4W[isp]+12*sqr(sin2fW)*A3))+
12*vyinit*A2-24*vzinit*cos_psi*A1);
}
}

void injection_push_FG(int isp, int i, float del_t)
{
int j;
float vxinit, vyinit, vzinit, xinit, vxtemp, vytemp, vztemp, xtemp;
float vxhalf, vyhalf, vzhalf;
float k, a0;
float sin2fW;

float s;

```

```

float ep, f, fW, A1, A2, A3, A4;

k = sp_k[isp];
vxtemp = vxinit = vxhalf = vx[isp][i];
vytemp = vyinit = vyhalf = vy[isp][i];
vztemp = vzinit = vzhalf = vz[isp][i];
xtemp = xinit = x[isp][i];

j = xinit;
s = xinit - j;

/* Assume that the particle is injected from
   the right or left side of the simulation */

a0=a[j];
if (j<1){
    ep = a_scale[isp]*rho[0]/epsilon*dx;
}
else{
    ep = a_scale[isp]*rho[nc]/epsilon;
}

if (b>0){
    /*position push*/
    /* a is for normalized for half a time step  a0*=2; */

    ep*=2;
    f = del_t;
    fW= f*W[isp];
    A1=f*(3*a0+ep*vxinit*f)*onesixth;
    A2=3*sin(fW)+fW*cos(fW);

```

```

A3=3*cos(fW)-fW*sin(fW);
x[isp][i] +=f*(vxinit+A1+twothirds*sin(fW)*sin_psi*(A2*(vzinit*cos_psi-
(vxinit+0.5*A1)*sin_psi)+A3*vyinit));

/*velocity push*/
f = del_t*.5;
fW=f*W[isp];
A1=(W[isp]*sin4W[isp]+12*sqr(sin(2*fW)))*one12;
A2=(W[isp]*sin22W[isp]-3*sin(4*fW))*onethird;
A3=0.25*(4+ep*sqr(f));
A4=0.5*f*a0;
sin2fW=sin(2*fW);
vx[isp][i] += a0*f+one24*(-
2*sqr(sin_psi)*(a0*W[isp]*sin4W[isp]+24*A4*sqr(sin2fW))+
vxinit*(ep*(1+12*sqr(f))-
4*sqr(sin_psi)*(12*A1+3*ep*sqr(f*sin2fW))))+
sin_psi*(-vyinit*A2+
vzinit*2.0*cos_psi*A2);
vy[isp][i] += sin_psi*(-onesixth*W[isp]*a0*cos22W[isp]-A4*sin(4*fW)+
vxinit*(onethird*W[isp]*sin22W[isp]-A3*sin(4*fW)))
-2.0*vyinit*A1-vzinit*A2*cos_psi;
vz[isp][i]+=
one12*cos_psi*(sin_psi*(a0*W[isp]*sin4W[isp]+24*sqr(sin2fW)*A4+2*vxinit*(W[i
sp]*sin4W[isp]+12*sqr(sin2fW)*A3))+12*vyinit*A2-24*vzinit*cos_psi*A1);
}
}

```